Dynamic Myocardial Single-Pinhole SPECT Imaging

Distance-Driven Forward and Back-Projection, and KDE-Based Image Reconstruction Methods

Dynamic Myocardial SPECT Imaging Using Single-Pinhole Collimator Detectors: Distance-Driven Forward and Back-Projection, and KDE-Based Image Reconstruction Methods

By
Alvin Ihsani

A Thesis Submitted to the
School of Graduate Studies
in Fulfillment of the Requirements
for the Degree
Doctor of Philosophy

McMaster University

Doctor of Philosophy (2015) (Computational Science and Engineering)	McMaster University Hamilton, Ontario

TITLE:	Dynamic Myocardial SPECT Imaging Using Single-Pinhole Collimator Detectors: Distance-Driven Forward and Back-Projection, and KDE-Based Image Reconstruction Methods
AUTHOR:	Alvin Ihsani, M.A.Sc. (McMaster University)
SUPERVISOR:	Troy Farncombe
NUMBER OF PAGES:	xiii, 81

Abstract

SPECT (Single Photon Emission Computed Tomography) is the modality of choice for myocardial perfusion imaging due to the high sensitivity and specificity, and the lower cost of equipment and radiotracers compared to PET. Dynamic SPECT imaging provides new possibilities for myocardial perfusion imaging by encoding more information in the reconstructed images in the form of time-activity functions. The recent introduction of small solid-state SPECT cameras using multiple pinhole collimators, such as the GE Discovery NM 530c, offers the ability to obtain accurate myocardial perfusion information with markedly decreased acquisition times and offers the possibility to obtain quantitative dynamic perfusion information.

This research targets two aspects of dynamic SPECT imaging with the intent of contributing to the improvement of projection and reconstruction methods. First, we propose an adaptation of distance-driven projection to SPECT imaging systems using single-pinhole collimator detectors. The proposed distance-driven projection approach accounts for the finite size of the pinhole, the possibly coarse discretization of the detector and object spaces, and the tilt of the detector surface. We evaluate the projection method in terms of resolution and signal to noise ratio (SNR).

We also propose two maximum a posteriori (MAP) iterative image reconstruction methods employing *kernel density estimators*. The proposed reconstruction methods cluster time-activity functions (or intensity values) by their spatial proximity and similarity, each of which is determined by spatial and range *scaling parameters* respectively. The results of our experiments support our belief that the proposed reconstruction methods are especially effective when performing reconstructions from low-count measurements.

Acknowledgements

I wish to thank my supervisor Dr. Troy Farncombe for providing the guidance, the funding, and the encouragement to actively participate in the scientific community. I thank my co-supervisor Dr. Christopher Anand and the members of my supervisory committee, Dr. Michael Noseworthy and Dr. Ned Nedialkov, for their constructive criticism, insight, and support. I would also like to thank Dr. Laurent Desbat for his guidance, advice, and help with the materials related to sampling in tomography, and Dr. Rolf Clackdoyle for always finding the right alternative for every problem I face. I would like to acknowledge Dr. Simon Rit for his assistance with Open Reconstruction Toolkit (OpenRTK) package which greatly facilitated the obtainment of results for our research.

I would like thank my colleagues at McMaster, and those at TIMC-IMAG (Techniques de l'Ingénierie Médicale et de la Complexité - Informatique, Mathématiques et Applications, Grenoble) for time and again sharing their precious insight and ideas that helped me overcome obstacles along the way.

Finally, I want to thank my family, my girlfriend Yaroslava, and my friends for their unconditional support during my studies.

Table of Contents

List of Figures

Glossary

Glossary of Terms

Abbreviation	*Meaning*
AIF	Arterial Input Function
CAD	Coronary Artery Disease (aka. Ischemic Heart Disease)
EM	Expectation Maximization
FADS	Factor Analysis of Dynamic Structures
^{18}F-FDG	Fluorodeoxyglucose
KDE	Kernel Density Estimator
LOR	Line of Response
MAP	Maximum a Posteriori
MS	Mean-Shift
$^{13}NH_3$	Ammonia
OSEM	Ordered Subset Expectation Maximization
PET	Positron Emission Tomography
^{82}RbCl	Rubidium Chloride
SPECT	Single Photon Emission Computed Tomography
TAC	Time-Activity Curve
^{99m}Tc	Technetium-99m
^{201}Tl	Thallium-201

Glossary of Symbols

Symbol	*Interpretation*
$\mathbb{R}^n$	n-dimensional Euclidean space
$\mathbb{Z}^n$	n-tuples of integers
$\mathbb{Z}_+^n$	n-tuples of positive integers
$\hat{f}$	Fourier transform of a function f
$\tilde{f}$	inverse Fourier transform of a function f
$\langle \cdot, \cdot \rangle$	inner product
δ	Dirac's delta function
$\theta^\perp$	subspace or unit vector perpendicular to θ
$A^\top$	transpose of operator A
$\lvert \cdot \rvert$	Euclidean norm or absolute value depending on the context
$\mathcal{D}$	Fan-beam transform
$\mathcal{T}$	Single-Pinhole Transform
$*$	convolution operator

(Page intentionally left blank)

Chapter 1

Dynamic Cardiac SPECT Imaging Using Single-Pinhole Collimators: Challenges and Proposed Improvements

The quantification of myocardial damage due to ischemia or infarction is an active field of clinical research. The reasons for the interest in this field lie in providing better diagnoses after ischemic episodes or infarction as well as enabling preventive care by detecting ischemia and fibrosis in cardiac tissues at an early stage.

Current nuclear imaging technology employing the use of radiotracers for the quantification of myocardial damage include modalities such as PET (Positron Emission Tomography) and SPECT (Single Photon Emission Computed Tomography). Both imaging modalities are used in a clinical setting, but SPECT is currently more widely used [56, 73] due to its lower purchasing and maintenance costs.

The introduction of solid-state organ-specific SPECT imaging systems, such as the GE Discovery NM 530c [7], have enabled dynamic SPECT imaging of the heart through arrays of small pinhole collimator cameras. Such imaging systems offer some advantages in terms of imaging speed and sensitivity, however, low signal-to-noise ratio (SNR) remains a challenge due to its dependence on a combination of factors including the rapid washout of radioactive tracers, the relatively short length of acquisition per time-frame, and gated imaging.

In our research we have attempted to mitigate the aforementioned challenges by targeting two key areas of research, namely, projection operator modelling and image reconstruction. We propose

- a distance-driven forward- and back-projection method targeted for imaging systems using single pinhole collimators (Chapter 2), and
- two image reconstruction methods stemming from a maximum a posteriori formulation that try to address the challenge of reconstructing images from low counts by performing clustering during the reconstruction process (Chapter 3).

In addition to the above, research has also been conducted toward finding sampling conditions for pinhole collimator imaging systems. The aim is to build a theoretical methodology to constructing organ specific imaging systems, where the resolution required for the study (i.e. the size of the smallest structures required to appear in the reconstructed images) determines a theoretical minimum of the discretization of the detector surface, and the number of the detectors required for the study. Since this is ongoing research, we only provide the details of our findings so far in Chapter 4 and discuss future prospects.

Even though the theory and experiments presented in the following chapters are geared toward SPECT imaging using pinhole collimators, the same methods can be applied to other imaging modalities. For instance, the proposed projection method can be applied

to cone-beam CT (Computed Tomography), where the X-ray source cannot be modelled by a point. Additionally, our research on the topic of sampling using pinhole collimators is directly applicable to linear fan-beam imaging [55].

Before exploring the details of each of the aforementioned areas of research, some background on the pathophysiology of myocardial ischemia, and the basic principles of emission tomography for both PET and SPECT is provided in order to create a more complete picture of the imaging modalities and their aims. A high-level description of the methods proposed for image acquisition, projection, and reconstruction follows.

1.1 Myocardial Ischemia and Principles of SPECT and PET Imaging

Pathophysiology of Myocardial Ischemia Myocardial ischemia is marked by the mismatch between the demand and supply of oxygen to the myocytes (myocardial muscle cells) [56]. Myocardial demand is determined by both the strength of the muscular contractions and the heart rate. During physical exercise the heart rate increases, and the force of myocardium increases to raise the stroke volume of the left ventricular systolic pressure. In healthy subjects, the arterioles can dilate during exercise, which leads to increased myocardial perfusion. In subjects suffering from coronary artery disease (otherwise known as ischemic heart disease) myocardial perfusion is limited due to coronary artery stenoses that increase the resistance of the larger arteries. The heart compensates for the added resistance by dilating the arterioles at rest, however, this means that at stress (i.e. exercise) the arteriolar dilation is limited thereby creating a limited blood flow [56]. This explains why most patients exhibit stress-induced ischemia.

Extended periods of stress-induced ischemia, if left untreated, can cause myocardial infarction which results from the interruption of the blood supply to myocardial cells causing myocyte apoptosis which causes permanent damage to the heart, and exposes the subject to life-threatening arrhythmia [46].

Emission tomography imaging, such as PET and SPECT, can be used to detect anomalies in the perfusion of the heart by injecting radiotracers that bind to healthy myocardial tissues in a predictable way. The variation of said tracers from the predicted models can aid in determining the damage to the myocardial tissues.

Basic Principles of PET Imaging The goal of PET imaging is to generate images of the distribution of positron emitting radiotracers *in vivo*. PET systems rely on the detection of annihilation gamma rays emitted through the process of positron decay. The gamma rays (photons) emitted from positron annihilation have an energy of 511 keV, as dictated by the mass of the positron and the formula $E = mc^2$, and travel in nearly opposite directions. The emission of these photons creates a line of response (LOR) which is the line connecting the locations of incidence. Figure 1.1 shows a schematic cross-section and top-view of a PET detector ring, along with an LOR dictated by the photon coincidence on the detector.

A collimator is a structure that is typically added to imaging systems in emission tomography to limit the the angle of incidence of photons emitted by the radiotracer. While a collimator can be used in PET imaging, it is preferable to rely on the LOR to narrow down the possible directions from which detected photons were emitted, to increase sensitivity (i.e. counted events). When a collimator is not used, PET has typically higher sensitivity than

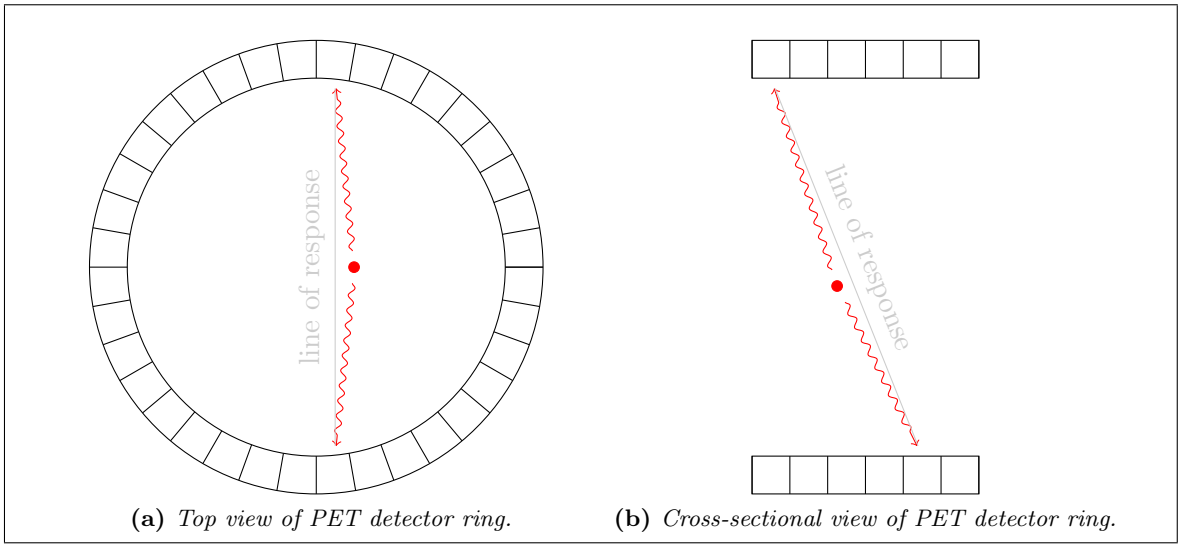

(a) *Top view of PET detector ring.* **(b)** *Cross-sectional view of PET detector ring.*

Figure 1.1: *PET detector ring in top-level and cross-sectional view. The emitted photons from the point of positron annihilation (red dot) coincide at different bins on the detector.*

SPECT. Figure 1.1b shows an example of PET detector rings that are not separated by collimator septa, and therefore oblique LORs are detected.

When a collimator is added, as is done in 2D PET imaging, septa separate the PET detector rings in such a way that LORs lie on the same ring, and therefore random events and scatter events arising from activity outside the axial field of view (FOV) are not recorded, leading to greatly decreased background counts. However, the addition of the septa also greatly reduces the sensitivity of the scanner [13].

Because in PET the subject is surrounded by a ring of detectors, all projection angles are sampled simultaneously. This means that a reconstruction can be performed from data acquired in a single time-frame, and therefore physiological processes that change tracer distribution over time can be monitored and evaluated to provide quantitative estimates of blood flow, for example.

Typical radiotracers used in myocardial perfusion imaging in PET include ^{82}RbCl, $^{13}NH_3$, and ^{18}F-FDG which is used in myocardial metabolic imaging. The half-life of PET tracers is typically shorter compared to SPECT tracers, and generally a nuclear reactor or cyclotron must be available on-site with the PET scanner to carry out an imaging study. The high costs of purchase and maintenance associated with PET imaging sometimes outweigh the benefits, and limit the availability of PET in clinical practice.

Basic Principles of SPECT Imaging The goal of SPECT imaging is to generate images of the distribution of photon-emitting radiotracers *in vivo*. Unlike PET tracers, SPECT tracers emit a single photon from radioactive decay and therefore a collimator is required to limit the directions from which photons are collected.

A multitude of collimators have been developed for SPECT imaging over the years, each with a specific purpose.

- Parallel-hole collimators aim to produce orthogonal projections of the object being

imaged.

- Fan-beam collimators were developed to produce projections which are magnified in one direction.[1]
- Single- and multi-pinhole collimators were introduced to produce projections which are magnified (or reduced) in all directions.

Figure 1.2 shows a schematic view of some of the aforementioned geometries.

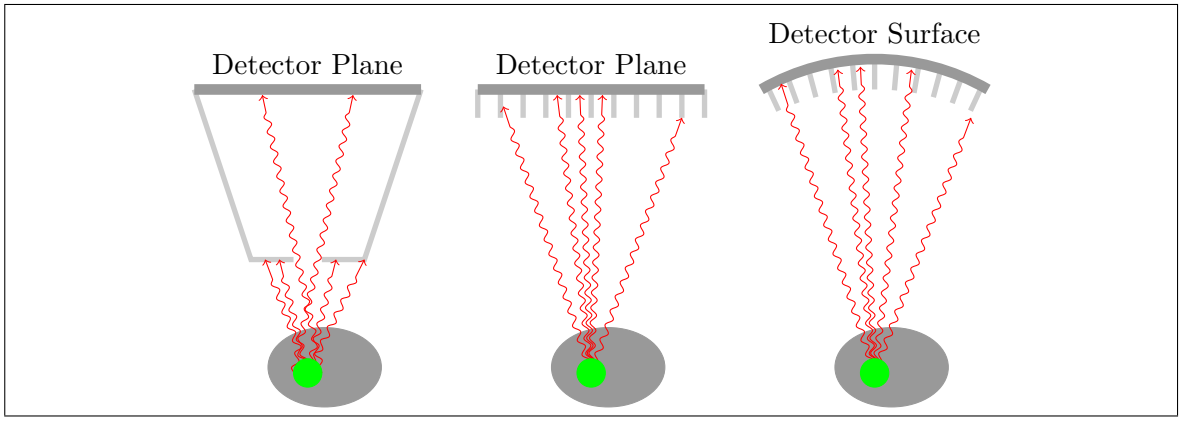

Figure 1.2: *Schematic view of typical collimators used in SPECT imaging: single-pinhole collimator (left), parallel-hole collimator (centre), fan-beam collimator (right). The provenance of measured photons (red lines) emitted from the radiotracer (green) in the subject (gray) is limited by the shape of the collimator.*

In SPECT, unlike PET, the detector head revolves around the subject, or in the case of fixed systems (where detector heads do not move) there is a limited number of heads surrounding the subject. It follows, that imaging dynamic processes in SPECT is not as straightforward as in PET since, depending on how quickly the tracer distribution changes over time, one may not have enough measurements to perform a reconstruction from a single acquisition time-frame. Typically, one must rely on kinetic models of tracer distribution (or some form of temporal modelling) to perform dynamic reconstructions in SPECT.

Currently, SPECT imaging is the modality of choice for clinicians performing cardiac studies, due to the lower cost of SPECT scanners (compared to PET), and higher availability and lower cost of production associated with the radiotracers [73]. Typical perfusion tracers used in cardiac SPECT imaging include Thallium (^{201}Tl), and Technetium-based tracers (^{99m}Tc-sestamibi, ^{99m}Tc-tetrofosmin, ^{99m}Tc-teboroxime) among others [23, 24, 31, 69, 74].

In general, PET has technical advantages over SPECT since spatial resolution is typically higher, the acquisitions are shorter, and motion artifacts present less of a problem [56]. Furthermore, PET imaging in a clinical setting is used for absolute quantification of perfusion, while SPECT imaging (even though it presents the same potential) is used to measure relative uptake [13, 56].

The main disadvantage of measuring relative tracer uptake is that one can only perform a differential diagnosis based on the comparison of healthy and unhealthy tissues.

[1] The PET detector ring is a special-case of the fan-beam collimator.

However, systemic under-perfusion (e.g. multi-vessel disease where the whole heart is under-perfused) can go undetected. In contrast, PET imaging can provide parametric images that show absolute measures of perfusion, which enables the clinician to identify systemic damage.

In our research, we pursue the improvement of SPECT imaging due to its potential to applications in preventive care, where the early detection of perfusion anomalies in the myocardium would greatly benefit patients, its cost-effectiveness in terms of purchase and maintainability, and its greater availability.

1.2 A High-level View of the Areas of Research and The Proposed Solutions

We have attempted to address three key areas in dynamic SPECT imaging employing pinhole collimators, namely, optimization of data acquisition, projection operator modelling, and design of a dynamic image reconstruction algorithm targeted for reconstructions from low-count measurements. This section provides a methodological view of each of the proposed approaches and arguments to justify the chosen course of research. It must be noted that our research in the optimization of the acquisition is still ongoing, however, we present our current findings here in order to provide a more complete picture of our goals.

Optimizing the Acquisition Protocol

The acquisition protocol must be optimized so as to obtain the desired degree of spatial resolution based on the structures of interest in the heart (i.e. thickness of the myocardial wall), while at the same time minimizing the cost of the scanning device by finding the coarsest discretization of the detector surface and the smallest number of projections or heads needed to accomplish this. The proposed methodology approaches this problem from an analytical perspective; that is, asymptotic properties of integral transforms in Fourier space are analyzed to determine an efficient sampling scheme.

In past research, we constructed a single-pinhole integral transform [40] and attempted to analyze the asymptotic properties of said transform in Fourier space [5,6,53–55]. While exact results were obtained for a curved-detector single-pinhole transform (effectively leading to a reparametrization of the standard fan-beam transform), great difficulty was encountered when analyzing the flat-detector single-pinhole transform, which is of greater interest in our application.

As an alternative, the transform of interest (flat-detector single-pinhole transform, or linear fan-beam) was approximated as a perturbation of a known transform (angular fan-beam) so that an efficient sampling scheme for the first can be determined by the latter. Two analytic approaches were employed to address the problem of efficient sampling, namely, the coarse-grid approach [22, 25] and the non-uniform sampling approach [32, 78].

The principal reason for choosing an analytic approach to finding an efficient sampling scheme is to simplify the problem of finding the optimal radius of rotation, and choosing the minimum number of detector heads along with the coarsest resolution of the detector surface. The result of our approach can then be used as a starting guess in numerical simulations that account for additional factors that are more directly related to the properties of the imaging system or study. If the same problem was approached using strictly numerical methods, we believe the complexity of the problem would quickly increase.

In the current approach, we do not address a number of problems such as truncated (or incomplete) projections and noise, however, it may be possible that this modelling effort can be transferred to later stages in the imaging chain by, for instance, letting the projection method mitigate data truncation, and letting the image reconstruction method mitigate noisy measurements by employing a denoising strategy during reconstruction.

Modelling the Projection Operator for a Single-Pinhole Imaging System

The projection operator is an integral part of the imaging chain since it determines the spatial distribution of activity across the object and detector space. We propose an extension of the distance-driven forward and back-projection method [18, 19] that is targeted to emission tomography imaging using pinhole collimators. The proposed approach accounts for the finite size of the pinhole, and samples the pinhole along its circumference resulting in a piece-wise linear approximation of the kernel function which augments object cells (i.e. voxels) projected through a point. The fraction of activity attributed to a certain detector bin is then estimated from the overlap of the detector bin and projected object cell.

We evaluate the proposed distance-driven projection method by comparing it to a ray-driven projection method. Experimental results show that the proposed method preserves the structure of reconstructed objects better in the presence of noise, albeit it is more computationally intensive than the ray-driven approach due to the large number of polygon intersection calculations.

An important physical effect in emission tomography is the spatially-dependent reduction of measured photon counts due to the radiotracer being obscured by a relatively dense material (e.g. bone, metallic implants) which "traps" emitted photons. This effect, if not accounted for, will affect the distribution of the radiotracer during image reconstruction since the algorithm may inherently assume that the lower counts in some projections are due to the distance of the radiotracer to the detector head, rather than due to an obstruction. The proposed projection operator does not account for such physical effects, however, one can include attenuation correction in the proposed projector if the attenuation map is estimated separately.

Designing an Image Reconstruction Method

To mitigate the challenge of reconstructing images in the presence of noise, we propose two maximum a posteriori iterative methods of dynamic image reconstruction, one which employs a kernel density estimator-based prior (MAPKDE) [30], and one which employs a Gaussian prior to constrain the behaviour of the time-activity functions (TAF) to "mean TAFs" that are estimated from mean-shift filtering at each iteration [15, 17].

A disadvantage of the proposed iterative schemes is that they do not explicitly deal with the interior problem, where images must be reconstructed from truncated data. However, due to the nature of the organ-specific imaging system (which is the focus of our study) it is assumed that activity coming from sources other than the organ of interest does not affect the reconstructed image. We also argue, based on existing literature (see [29, 50, 81]), that one can mitigate the artifacts introduced from truncated data by modelling the projection operator accordingly, and without changing the iterative reconstruction method itself.

1.3 Summary

This chapter has presented our motivation, and the three key areas of our research. In the following two chapters we discuss the details of the distance-driven projection approach, and the kernel density estimator based MAP image reconstruction approaches. The last chapter describes the theory related to our ongoing research in efficient sampling for the linear fan-beam transform (i.e. flat-detector single-pinhole transform).

Chapter 2

An Adaptation of the Distance Driven Projection Method for Single Pinhole Collimators in SPECT Imaging

In emission tomography, the aim is to reconstruct multi-dimensional activity images from projection measurements of an injected radioactive tracer. These projections represent detected events (i.e. detected photons) emitted from various locations within the field of view (FOV) of the scanning system. Determining the locations of the originating emission is a challenging task and different approaches are taken for different imaging modalities to "narrow down" the direction of a detected event (or photon count).

In Single Photon Emission Computed Tomography (SPECT) the possible lines of detection are limited through the use of a physical collimator. The geometry of the collimator limits the region within the FOV from where a detected photon is assumed to originate. While in clinical practice there exist many collimator geometries (i.e. parallel, fanbeam, etc), this material will focus on the single pinhole collimator geometry. We present an algebraic projector (and subsequent back-projector) which accounts for factors such as the finite size of the pinhole, possible tilting of the detector surface, and geometric sensitivity [2,41,52]. The aim is to provide an adequate algebraic approximation of the physical system (or acquisition process) to improve reconstruction accuracy.

Currently, there exist several methods for projection and back-projection that can be extended to pinhole SPECT imaging. For instance, ray-driven methods are excellent candidates to perform forward and back-projection, if one wants to include such factors as penetrative sensitivity [52]. Ray driven methods work by tracing rays through an object onto the detector surface thereby discretizing the integral line and approximating each integral line as the cumulative weighted sum of image voxels intersecting the ideal line. Several techniques have been used to weight the contribution of each voxel to the idealized integral line (see [77,79,82] and the references therein for a detailed overview). Ray-driven methods also have a transpose operator that performs the backprojection operation.

Some drawbacks of ray-driven methods include the introduction of artifacts in the form of Moiré patterns in the backprojection, and non-sequential memory access patterns, which may significantly affect performance [19]. In pinhole SPECT imaging, due to the coarse discretization of the object (i.e, 64^3-123^3 voxels) and detector space (i.e. 64^2-128^2 bins), memory may not be a limiting factor, but there are additional considerations such as the finite size of the pinhole that may present problems for ray-driven methods. One obvious approach to adapt ray-driven projection to pinhole SPECT would be to sample the pinhole at L locations which would result in performing the forward or back-projection L times (that is, from L different ideal pinholes). This problem is further complicated by the question of the pinhole surface sampling pattern to be used in order to minimize sampling artifacts.

A fundamentally different approach to ray-driven projection is *pixel-driven* projection, where intersection calculations are performed between backprojected detector pixels and object voxels in the case of backprojection, and projected object voxels and detector pixels during projection [43, 62, 82]. The drawbacks of pixel-driven projection include the introduction of high frequency artifacts, and high computational cost due to polygon intersection calculations.

A further category of projection methods are distance-driven methods introduced in [18, 19]. These methods are known for their lower arithmetic complexity, sequential memory access patterns, and the avoidance of artifacts commonly observed in ray-driven and pixel-driven projection approaches. The distance-driven projection method maps the object voxel and detector pixel onto a common plane or axis (for 3D and 2D imaging respectively) and applies a one-dimensional kernel operation to map data from one set of boundaries to the other.

In this chapter, we present a projection method which combines the distance-driven and the pixel-driven approaches. On the one hand, the similarity to the distance-driven approach comes from the fact that the weights used to determine the contribution of a detector pixel to an object cell and vice versa are determined from the overlap of these elements when projected onto a common plane. On the other hand, the similarities shared between our approach and the pixel-driven approach come from the fact that intersection calculations between projected object cells and detector pixels need to be performed in order to determine the weights for distance-driven projection. Furthermore, the regularity of the detector surface is exploited in order to reduce the number of computations.

2.1 The Proposed Distance-Driven Projection Method for Pinhole SPECT Imaging

This section provides a brief presentation of the distance-driven projection method in one, two and three dimensions, and then extends the concept to SPECT imaging using a finite-size pinhole and slanted detector surface.

2.1.1 Distance-Driven Projection

Let the source signal be defined by a set of values $f_0, f_1, \ldots, f_{N-1}$ at locations $x_0 < x_1 < \ldots < x_{N-1}$ and the destination signal $g_0, g_1, \ldots, g_{M-1}$ at locations $y_0 < y_1 < \ldots < y_{M-1}$. Re-sampling is then performed by a process known as the *kernel operation* where the destination values $\{g_j\}$ are determined by the source values $\{f_i\}$, source locations $\{x_i\}$, and destination locations $\{y_j\}$. Specifically, the destination value is calculated as

$$g_j = \sum_{i=0}^{N} \omega_{j,i} f_i \tag{2.1}$$

where $\omega_{j,i}$ is the degree of overlap between source and destination cells and is defined as

$$\begin{aligned} \omega_{j,i} &= \int_{y_j}^{y_{j+1}} \mathbf{1}_{x_i \le x < x_{i+1}} dx \\ &= |[y_j, y_{j+1}] \cap [x_i, x_{i+1}]| \end{aligned} \tag{2.2}$$

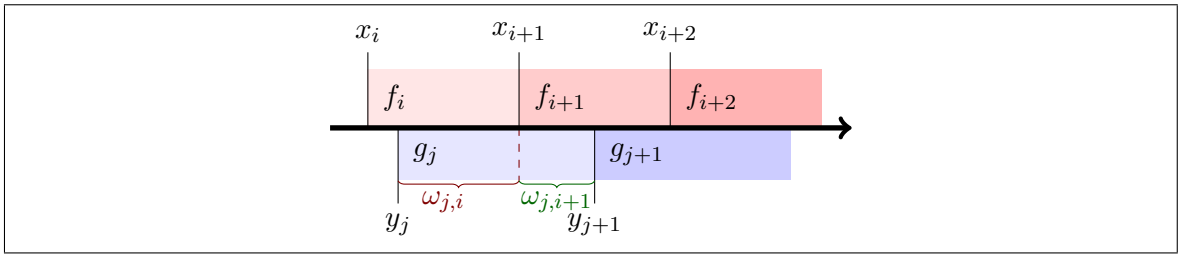

Figure 2.1: *Schematic view of the distance-driven kernel where the length of the overlap between source and destination cells is used as a weight to map the contribution of the source value to the destination value. Shown in the figure: source cells $\{f_i\}$ starting at locations $\{x_i\}$, destination cells $\{g_j\}$ at locations $\{y_j\}$ and overlaps $\omega_{j,i}$ and $\omega_{j,i+1}$ which occur between destination cell g_j and source cells f_i and f_{i+1} respectively.*

where the absolute value denotes the measure of the set, and $\mathbf{1}_{x_i \le x < x_{i+1}}$ is an indicator function for the set $[x_i, x_{i+1}]$.

For example, for the 1D source and destination cells shown in Figure 2.1, the source and destination intensities are related by

$$g_j = \omega_{j,i} f_i + \omega_{j,i+1} f_{i+1} \tag{2.3}$$

where

$$\begin{aligned} \omega_{j,i} &= |[y_j, y_{j+1}] \cap [x_i, x_{i+1}]| = x_{i+1} - y_j, \\ \omega_{j,i+1} &= |[y_j, y_{j+1}] \cap [x_{i+1}, x_{i+2}]| = y_{j+1} - x_{i+1}. \end{aligned}$$

One may choose kernel weights that are normalized by the source or destination intervals. For instance, taking the example of Figure 2.1 the weights would become

$$\omega_{j,i} = \frac{x_{i+1} - y_j}{y_{j+1} - y_j}, \quad \omega_{j,i+1} = \frac{y_{j+1} - x_{i+1}}{y_{j+1} - y_j},$$

when normalized by the destination intervals.

The aforementioned kernel operation can be extended to 2D/3D tomography by letting the detector pixels be the source cells and the object voxels be the destination cells, as is the case in backprojection. Figure 2.2 provides a schematic view of how the distance-driven approach is applied in the context of cone-beam computed tomography (CT), where the X-ray source and detector plane are typically on opposite sides of the object space (or field of view). This figure depicts the projection of a single object voxel and a corresponding incidental detector bin onto the (common) xz-plane.

Denoting the overlap of the detector pixel to the projected object voxel by ω_1 and ω_2 in the in- and out-of-plane directions respectively as shown in Figure 2.2c, and the projection of the detector pixel in these directions by λ_1 and λ_2, the contribution to the j-detector pixel from the object is then given by

$$g_j = \frac{t}{\cos\beta \cos\gamma} \sum_{i=1}^{N} \frac{\omega_{1,j,i}}{\lambda_{1,j}} \frac{\omega_{2,j,i}}{\lambda_{2,j}} f_i \tag{2.4}$$

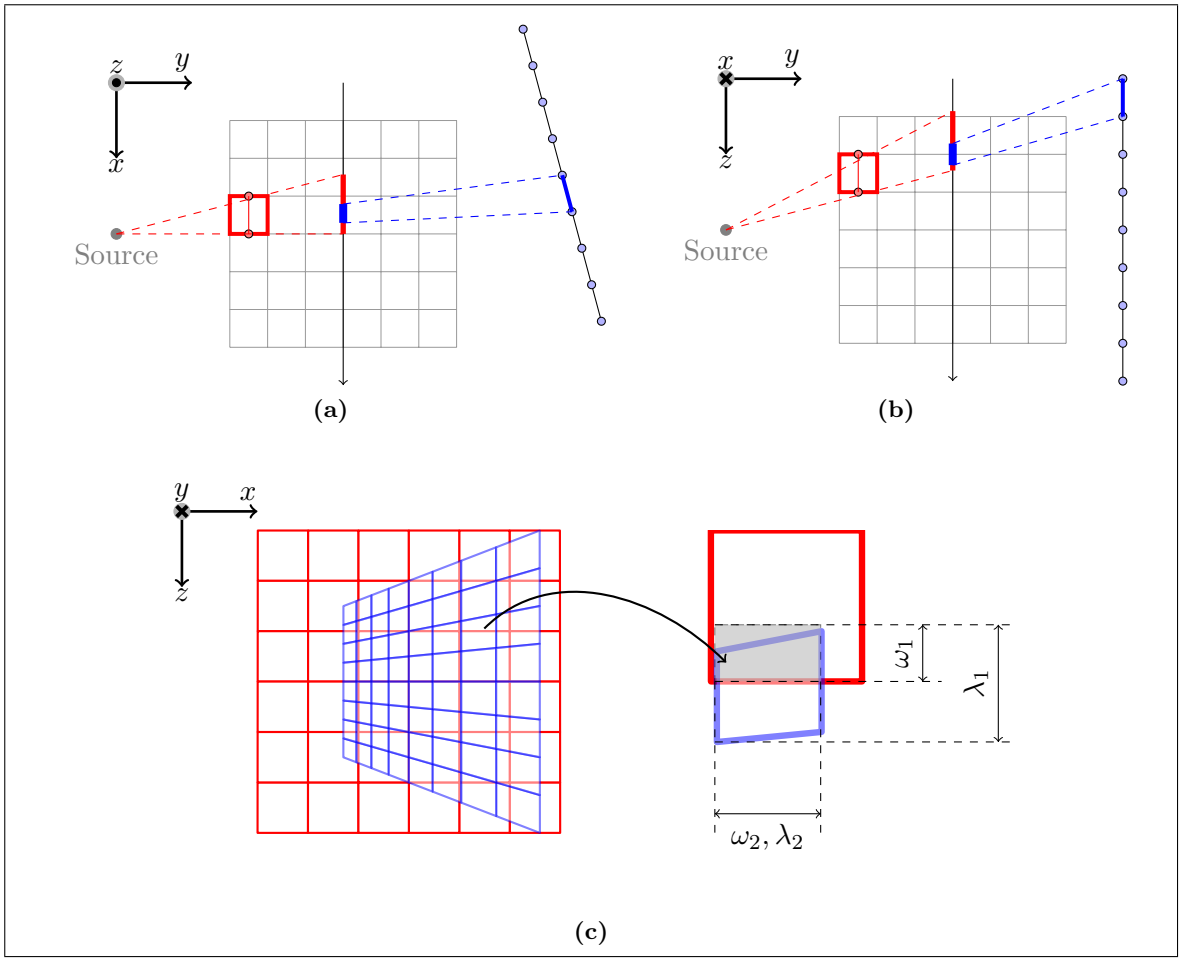

Figure 2.2: *Schematic outline of the distance-driven approach in cone-beam CT shown when looking from the positive z-axis in (a) and from the negative x-axis in (b). The object voxels (red) and detector pixels (blue) are projected along the y-axis (the main projection direction) onto the xz-plane as dictated by the source point. The dashed lines in blue and red respectively show the projection of the corners of the detector bin and mid-plane of the object voxel onto the xz-plane through the source point. Figure (c) shows projected object voxels in red along with the projected detector bins in blue onto the common xz-plane. The area of overlap of a detector pixel to an object voxel is approximated by the gray shaded area: ω_1, ω_2 correspond to the dimensions of the approximated overlap area and λ_1, λ_2 to the approximate dimensions of the projected detector pixel.*

where t is the isotropic voxel size, β and γ are the in- and out-of-plane angles with respect to the y-axis.

In the next section, a projection approach for single pinhole SPECT imaging that shares many similarities to the distance-driven projection method described above is presented. The main difference between the proposed distance-driven approach and the aforementioned is that the X-ray source (which corresponds to the pinhole in SPECT imaging) is assumed to have finite size.

2.1.2 Adapting Distance-Driven Projection to SPECT Imaging

It is apparent that the distance-driven projection method assumes that projections are taken through a point source. This assumption, however, is not valid in pinhole SPECT since the pinhole has finite size, which affects the quality of image dramatically depending on the focal distance (i.e. perpendicular distance of the pinhole to the detector plane). Specifically, with a larger pinhole radius, there is increased blurring due to the increased number of sources that are detected in the same detector pixel. Conversely, if one does not model the physical effects caused by the finite size of the pinhole by, for instance, assuming the pinhole is infinitely small, then the backprojection operation will not update the values of the object voxels in an adequate manner since the detected counts will be distributed to a different region than the one from which it was originally emitted.

Furthermore, in pinhole SPECT imaging, a projected object voxel may occupy a large region of the detector space due to its proximity to the pinhole, its possibly large size, and the tilt of the detector plane. This problem may be exacerbated when the detector surface is tilted as the projected object voxels are deformed and possibly enlarged along the direction of the tilt.

To address the aforementioned problems, we introduce a sampling strategy for the shape of the pinhole and compute the shape of the projected object cell[1] more accurately. Specifically, we sample the perimeter of the pinhole thereby approximating the shape of the pinhole by a polygon. For example, in Figure 2.3 the pinhole has been sampled at 4 locations making the pinhole shape effectively rhombic. As our results will show, choosing 4 sampling points provides a good balance between computational cost and reconstruction accuracy. In this case, it is apparent that rhombus and square pinholes are described exactly, and shapes such as circles are approximated well since at least 64% of the area of the projected voxel is covered (i.e. when the voxel is a point). As can be seen from Figure 2.3b, the choice of the pinhole shape approximation kernel expands (or grows) the *ideal projected object cell* (IPOC) accordingly. In summary, our approach only limits the approximation of the pinhole to polygons so the user may choose to sample the circumference of the pinhole in a manner appropriate to the application (see Figure 2.4a).

It is important to note that the expansion of the projected object cell is dependent on the ratio of the collimator focal distance to the distance of the object cell vertex from the collimator. Notice, for example, that in Figure 2.3, the vertices of the object cell that are closest to the pinhole are expanded more than those further away. This detail is added so as to create a better approximation of the projection of the spatial basis function (e.g. voxel) on the detector space, especially in the case where the detector surface is tilted.

A fundamental difference between our approach and the distance driven approach [19] is that the object cells are projected onto the detector space, therefore the detector plane itself corresponds to the *common plane* in the distance driven approach. The reason for this relates to both the finite size of the pinhole and the computational complexity of the projection of the object cells. Intuitively, both the detector pixels and projected object voxels must be expanded according to the shape of the pinhole after being projected onto a common plane in order to estimate the overlap accurately. However, this increases the

[1]The term "object cell" is used instead of "object voxel" since the proposed projection method does not restrict object space discretization to cubic voxels, but rather any convex shape.

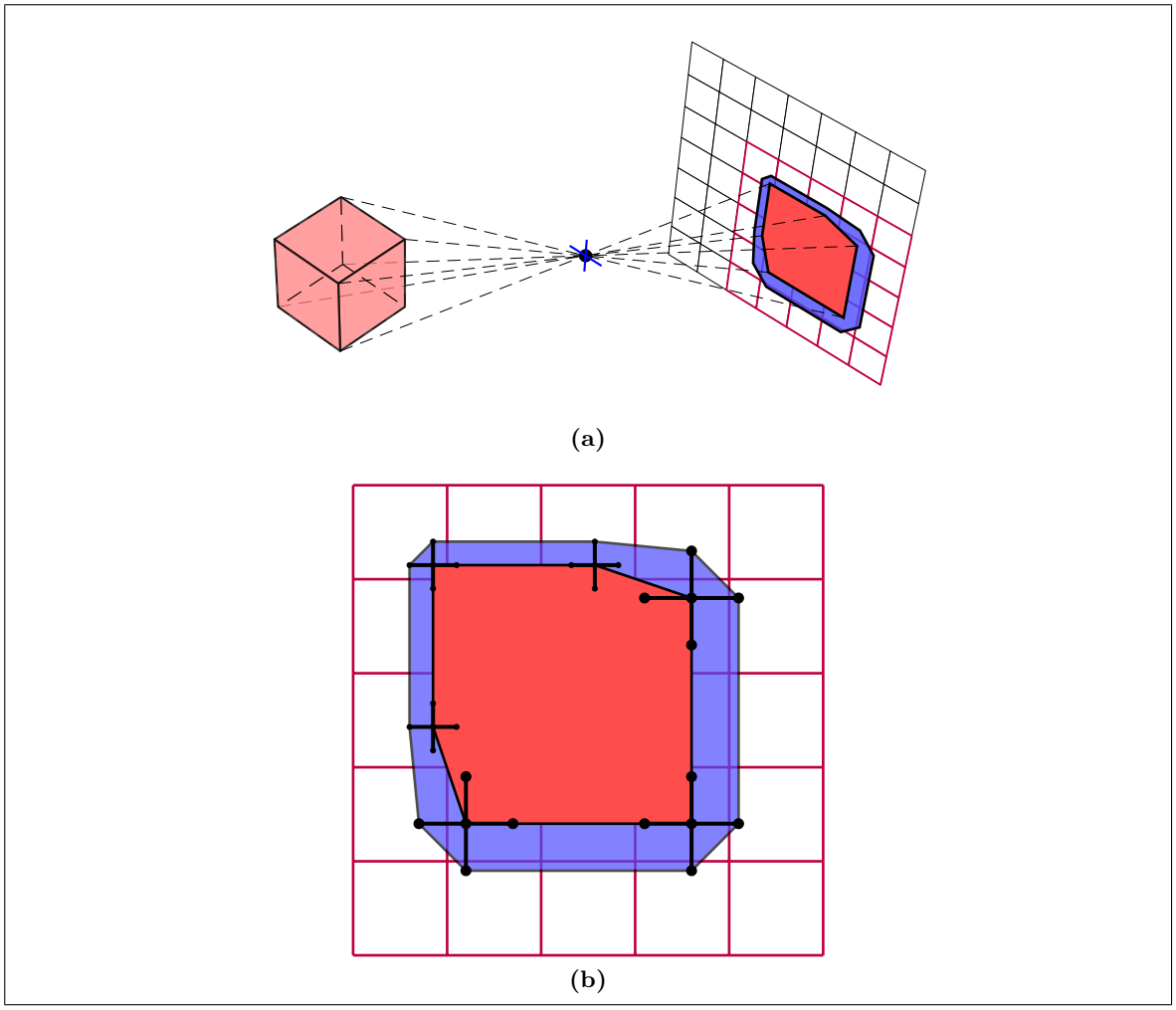

Figure 2.3: *Schematic outline of the proposed distance-driven approach for SPECT imaging. Components in Figure (a): (near-left) object cell, (far-right) the detector plane showing the projected object cell and (in between) the finite-sized pinhole approximated by the points on the cross. Figure (b): a close up of the projected cell shown in Figure (a). The red shape is obtained from the projection of the object cell through an idealized pinhole of infinitely small radius while the blue shape surrounding it shows the approximated "expansion" of the projected object cell (EPOC) through the finite-sized pinhole which is represented by the blue cross at the joining point of the projection lines. Note that the cross approximating the pinhole changes in size depending on the distance of the object cell vertex to the pinhole (i.e. the further away the vertex from the pinhole the smaller the cross and resulting expansion).*

number of elements that need to be projected (i.e. N voxels and M pixels must be projected), and increases the computational cost since more elements need to be expanded. Furthermore, if our approach were to use an intermediate (or common) plane, the cost of estimating intersections between *expanded projected object cells* (EPOC) and detector pixels increases since the regularity of the the bins in the detector plane may not be preserved (e.g. in the cases the detector plane is tilted). For the aforementioned reasons, we exploit the regularity of the detector surface to narrow down the number of candidate detector pixels

that may intersect with a given EPOC. In Figure 2.3a, the detector pixels involved in the polygon intersection and overlap ratio computations for the shown EPOC are highlighted in purple.

It is worth noting that the distance-driven approach proposed here does not address the issue of aperture penetration (see [52] and the references therein for existing approaches), however, the aim is to address this issue in the near future. A short explanation of one possible strategy to implement aperture penetration is provided in Section 2.3.2.

Projecting the Object Cells

To simplify the projection of the object cells, we consider a detector surface-centric coordinate system, where the origin of the detector surface becomes the origin of the whole projection system (as opposed to the origin of the FOV).

Let $\{p^\ell \in \mathbb{R}^3\}_{\ell=1,\dots,L}$ denote the sampling points along the pinhole perimeter (see Figure 2.4) where a rhombic approximation admits $L = 4$, and let $|p|$ denote the distance of the ideal pinhole p^0 from the origin. Then given the detector surface tilting angles α, β, and γ, we obtain the pinhole coordinates as seen from the centre of the tilted detector

$$\begin{aligned} p^\ell &= R_{\text{tilt}}(-\alpha,-\beta,-\gamma) \begin{pmatrix} r\cos(2\pi\ell/L) \\ |p| \\ r\sin(2\pi\ell/L) \end{pmatrix} \\ p^0 &= R_{\text{tilt}}(-\alpha,-\beta,-\gamma) \begin{pmatrix} 0 \\ |p| \\ 0 \end{pmatrix}. \end{aligned}$$

Here, R_{tilt} is the rotation matrix for the tilting of the detector surface, and r is the radius of the pinhole.

Let the object space be discretized into N cells, and let the intensities of the object voxels be denoted by $\{f_i\}_{i=1,\dots,N}$ with $\{x_i^k \in \mathbb{R}^3\}_{i=1,\dots,N}$ denoting the k corners of object cell i (in the case of cubic voxels $k = 1,\dots,8$). The object cell corners as seen from the detector surface origin are computed as

$$\Omega_i^k = R_{\text{tilt}}(-\alpha,-\beta,-\gamma)(R_{\text{head}}(-\theta,-\phi)x_i^k - p)$$

where $p = (0,|p|,0)^\top$, and R_{head} is the rotation matrix for the detector head (i.e. in-plane and out-of-plane angles).

From here one may compute the vertices of the EPOC (blue region in Figure 2.3) denoted by $\{w_i^{k,\ell} \in \mathbb{R}^2\}_{i=1,\dots,N}$ as

$$\begin{pmatrix} w_{i,1}^{k,\ell} \\ w_{i,2}^{k,\ell} \end{pmatrix} = \kappa \begin{pmatrix} -\Omega_{i,1}^k + (p_1^\ell - \Omega_{i,1}^k)\frac{\Omega_{i,2}^k}{p_2^\ell - \Omega_{i,2}^k} \\ -\Omega_{i,1}^k + (p_3^\ell - \Omega_{i,3}^k)\frac{\Omega_{i,2}^k}{p_2^\ell - \Omega_{i,2}^k} \end{pmatrix} \tag{2.5}$$

where

$$\kappa = \begin{cases} -1 & , \quad \frac{\Omega_{i,2}^k}{p_2^\ell - \Omega_{i,2}^k} > 0 \\ 1 & , \quad \text{otherwise} \end{cases}$$

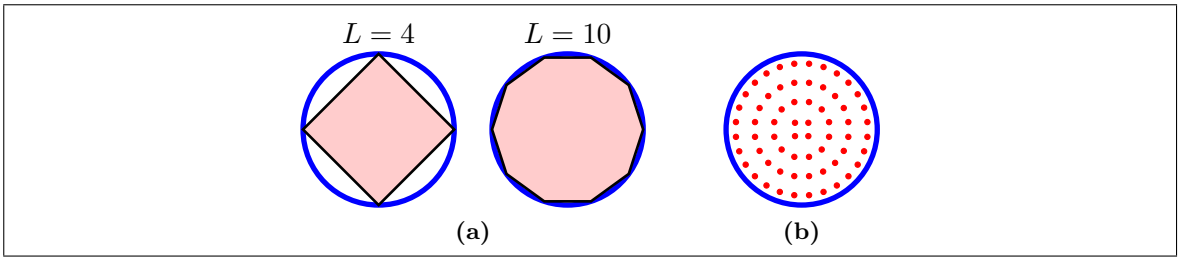

Figure 2.4: *Schematic outline of a circular pinhole shape (blue) sampled using the (a) proposed method and (b) the ray-driven method. In the proposed approach, the perimeter of the pinhole is sampled in order to create a polygonal covering of the pinhole surface. In contrast, in the ray-driven approach the pinhole must be sampled throughout the surface: the sampling shown corresponds to a* 8×8 *concentric map between a square and a circle.*

makes sure the point is projected is the correct orientation even when R_{tilt} rotates the detector in a direction where the image is projected on the back of the detector surface. One may also choose $\kappa = 0$ when $\frac{\Omega^k_{i,2}}{p^\ell_2 - \Omega^k_{i,2}} > 0$ so that no image is projected on the back of the detector.

While the number of computations required for the projection of the object cells increases depending on the number of pinhole sampling points, L, and number of cell vertices, this remains a parallelizable process, since given the pinhole position and its sampling points all operations are component-wise, and therefore does not constitute a performance bottleneck.

Finding the Convex Hull in Detector Space

The aforementioned method projects the object cell vertices using the polygonal pinhole kernel. With this method, the points calculated are not the points on the convex hull, but rather all the points of the object cell projected from all the pinhole sampling points (see the endpoints on the crosses shown in Figure 2.3). To estimate the overlap ratio, the intersection of the convex hull (e.g. using [4, 14, 42]) of the projected object cell vertices with the detector pixels must be determined. In this step, only the vertices $w^{k,\ell}_{i,d}$ which are on the convex hull are maintained, denoted by $\nu^\tau_{i,d}$, where τ indexes the τ-th vertex of the convex hull.

Computing the Intersection of Polygons and Overlap Ratio

The most computationally expensive step in the proposed projection process is the computation of the intersection of the convex hulls of projected object cells and detector pixels. Here we have exploited the typical regularity in location and size of the detector pixels to reduce the number of polygons needed to intersect by predicting possible collisions.

Let the convex hull of an EPOC be denoted by $\mathcal{P}_i$. If the detector cell spacing in each direction d is denoted by h_d then the set of possible intersection pixel indices in each

direction d is within

$$\begin{aligned} s_{\min,d} &= \left\lfloor \frac{\min_\tau \nu_{i,d}^\tau - m_d h_d}{h_d} + 0.5 \right\rfloor, \\ s_{\max,d} &= \left\lfloor \frac{\max_\tau \nu_{i,d}^\tau - m_d h_d}{h_d} + 0.5 \right\rfloor \end{aligned}$$

where $\nu_{i,d}^\tau$ is the τ-th vertex of $\mathcal{P}_i$ in the d-th direction, m_d is the number of detector pixels in direction $d = 1, 2$.

The intersection of the EPOC convex hulls, $\mathcal{P}_i$, to the detector pixel, $\mathcal{Q}_j$, polygon can be obtained by using a clipping algorithm [70,72] and the area of the intersection polygon $\mathcal{I}_{(j,i)}$ can be computed using the signed trapezoidal area of each edge to the abscissa as

$$\text{Area}(\mathcal{I}_{j,i}) = \sum_{u=0}^{U-1} (v_{(j,i),1}^{[u+1]_U} - v_{(j,i),1}^{u}) \frac{v_{(j,i),2}^{[u+1]_U} + v_{(j,i),2}^{u}}{2} \tag{2.6}$$

where $v_{(j,i),d}^u$ is the u-th vertex of the intersection polygon $\mathcal{I}_{j,i}$ in direction d, and $[\,\cdot\,]_U$ is the modulo U operator.

Finally, the overlap ratio can be computed as

$$\omega_{j,i} = \frac{\text{Area}(\mathcal{I}_{j,i})}{\text{Area}(\mathcal{Q}_j)}, \tag{2.7}$$

where the ratio is normalized by the area of the detector pixel. One may also choose to normalize by the size of the convex hull of the EPOC, namely $\text{Area}(\mathcal{P}_i)$, or choose not to use normalization (depending on the application-specific model). However, one must make sure that the overlap ratio is computed using the same scaling during projection and backprojection.

Finally, the contribution of activity from the object to a detector pixel g_j is described by

$$g_j = \sum_{k \in \chi(\mathcal{Q}_j)} t_k(\theta, \phi) \omega_{j,k} \gamma_k f_k \tag{2.8}$$

where $\chi(\mathcal{Q}_j) = \{k | \mathcal{P}_k \cap \mathcal{Q}_j \neq \emptyset\}$, $\omega_{j,k}$ is computed using equation (2.7), $t_k(\theta, \phi)$ is the average object cell "thickness" as seen from the detector head rotation angles θ and ϕ, and γ_k is the geometric factor which determines the sensitivity due to the pinhole aperture and the distance of the source to the pinhole (see [2,41]) computed from either the centre of the object cell (f_k) to the pinhole, or as an average of the geometric factor computed on the vertices of the object cell.

Assuming the object cells are cubic voxels then (2.8) is simplified to

$$g_j = \frac{t}{\cos\theta \cos\phi} \sum_{k \in \chi(\mathcal{Q}_j)} \omega_{j,k} \gamma_k f_k \tag{2.9}$$

where t is the isotropic voxel size. Similarly, the backprojection operator can be computed using the same geometric factor and overlap ratios as described above from

$$f_i = \frac{t}{\cos\theta \cos\phi} \gamma_i \sum_{k \in \vartheta(\mathcal{P}_i)} \omega_{k,i} g_k, \tag{2.10}$$

where $\vartheta(\mathcal{P}_i) = \{k|\mathcal{P}_i \cap \mathcal{Q}_k \neq \emptyset\}$.

It is apparent from equations (2.9) and (2.10) that the forward and back-projection operations are the transposes of each other and therefore the weights $\omega_{j,i}$ that are computed from the forward projections can be used for the back-projection (and vice versa). Specifically, let $W = [w_{j,k}] \in \mathbb{R}^{M\times N}$ be the matrix of overlap weights, and $\Gamma \in \mathbb{R}^{N\times N}$ be the geometric sensitivity matrix, then with $f \in \mathbb{R}^N$ and $g \in \mathbb{R}^M$ as vector representations of the object space and detector space respectively we see that

$$g = \frac{t}{\cos\theta\cos\phi} W\Gamma f \quad \text{and} \quad f = \frac{t}{\cos\theta\cos\phi}\Gamma^\top W^\top g$$

are transpose operations.

In summary, this section has presented an algebraic approximation to perform forward and backprojection in pinhole SPECT imaging by modifying the distance-driven method so as to determine the contribution of activity from an object cell to a detector pixel and vice versa. The proposed approach samples the surface of the pinhole using a polygon in order to account for the blurring caused by the shape and size of the pinhole. This approach, due to the fewer approximations performed at an element-level (i.e. object cell), is more computationally intensive, and therefore better suited for reconstructions at coarser object-space discretization which are typical of SPECT imaging (i.e. 64^3 to 128^3 voxels). It is apparent from [19] that further approximations can be made at finer object-space discretizations.

2.2 Validating the Proposed Model

The proposed model is compared against a ray-driven method in order to gain some insight to the advantages and disadvantages in terms of artifacts introduced in the context of image reconstruction. The ray-driven method used for the comparison uses a slice-interpolated strategy [44,77] whereby the pinhole has been sampled using a concentric mapping of points from a square [68] as shown in Figure 2.4b.

The main difficulty with using a ray-driven approach to sample a finite-sized pinhole, is determining the weighting the overlap of rays in the object space. If we were to take the mean activity of all the rays, we would be assuming that the rays completely overlap (or in other words, measure the same exact region) in the object space, which is exact only for an infinitely small pinhole. The exact weighting would account for the overlapping regions of rays in different sampling points of the pinhole by averaging the activity in the regions that overlap and adding the activity in the regions that do not. This last approach increases the complexity of the forward and backprojection in the ray-driven approach. For the purposes of the experiments presented below, it is assumed that the pinhole is small enough so that the weighting of the rays reduces to averaging.

2.2.1 Experiment Setting

Two phantoms are used in order to compare the quality of images in the presence of noise and the resolution of the reconstructed images.

Point-Source Simulation

Projections of a three dimensional point-source phantom, composed of three point sources with effectively 300 kBq of activity due to multiple acquisitions each with 140 keV energy and a half-life of 6.022 hours, were generated using GATE [3, 11]. The projections were acquired at every 3° for a total of 120 projections on a great circle with a radius of rotation of 27.79 cm around the y-axis with focal length of 21.72 cm, detector discretization of 256×256 pixels, detector bin size of 0.11^2 cm^2, detector bin material CZT (Cadmium Zinc Telluride), and a Tungsten pinhole with radius 0.24 cm. The focal length and radius of rotation were chosen to be relatively large so that the blurring caused by the large pinhole radius would be somewhat diminished. The point sources were positioned at 0, 3.14 and 6.28 centimetres along the x-axis in both a cold background and a warm background with 300 KBq of activity. The reconstructed image has a discretization of $128 \times 128 \times 16$ voxels, each with size 0.22^3 cm^3 where the FOV is truncated along the y-axis since no activity exists outside the selected region. In the ray-driven approach, the pinhole was sampled using 8×8 points concentrically mapped between a square and a circle [68], while in the distance-driven approach the pinhole circumference was sampled at 4 points. The objective of this phantom is to compare the FWHM of the reconstructed point sources with each projection method and at varying detector resolutions

Mini-Deluxe Phantom^{TM}Experiment (Data Spectrum Corp., Durham, North Carolina)

The Mini-Deluxe Phantom^{TM} was filled with Tc-99m at a concentration of 7.4 MBq/ml with total activity 175 MBq and scanned in a Gamma Medica X-SPECT^{TM} system over a 10 hour period to obtain high-count projections with an average of 11,000 counts per projection after decay correction (top left image in Figure 2.5). The projections were acquired using a single pinhole geometry (diameter = 1 mm, 60° acceptance angle) in 128 projections over 360°. The radius of rotation was 8 cm, focal length of 9 cm, detector resolution of 82×82 pixels at (1.5×1.5) mm^2/pixel. The energy window for the detector was set to 140 keV ± 10% (126-154 keV). The reconstructed image has a matrix size of $82 \times 82 \times 42$ voxels covering a $(10 \times 10 \times 5)$ cm^3 FOV. In the ray-driven approach the pinhole was sampled using both 4×4 and 8×8 points concentrically mapped from a square to a circle in order to determine how the quality of reconstructed images is affected by the number of sampling points on the pinhole. In the distance driven approach the circumference of the pinhole was sampled at 4 points.

The Mini-Deluxe Phantom^{TM} phantom is used to show the relation between the quality of the reconstructed images and the total counts in the measured projections from an SNR perspective to find if the proposed distance-driven approach presents any advantages. While the high-count projection set was obtained as described above, lower-count projections were simulated by dividing the measured projection values by a factor $k \in \{2, 5, 10, 20, 30\}$. In each simulated projection, Poisson noise was added to the result by assuming the counts in the projections are the expected values to be used in the noise generation algorithm.

The software used to implement the ray-driven approach is based on OpenRTK [66]. The images are reconstructed by performing OSEM iterations [37] where groups of 8 equiangularly spaced projections are used at each iteration. The algorithm was terminated after

Table 2.1: *The isotropic full width at half maximum values of each of the activity points in the point source phantoms (in cold and warm background) with coarse and fine detector resolutions. In the ray-driven approach 8×8 sampling points were used while in the distance-driven approach only 4 sampling points were used.*

	x-axis position (cm)	Distance Driven Detector Discretization		Ray Driven Detector Discretization	
		64×64	256×256	64×64	256×256
Cold Bg.	0	0.33 cm	0.31 cm	0.44 cm	0.31 cm
	3.14	0.38 cm	0.32 cm	0.48 cm	0.31 cm
	6.29	0.33 cm	0.29 cm	0.45 cm	0.28 cm
Warm Bg.	0	0.33 cm	0.28 cm	0.44 cm	0.31 cm
	3.14	0.37 cm	0.29 cm	0.64 cm	0.48 cm
	6.28	0.34 cm	0.27 cm	0.60 cm	0.45 cm

two complete OSEM iterations. The number of iterations was chosen arbitrarily (i.e. based on what is typically used in clinical practice).

2.2.2 Results of Reconstructions and Quality Metrics

Point-Source Simulation

The point source phantom was reconstructed using both projection methods at different detector discretizations. The lower-resolution projections are generated by increasing the size of the detector pixel by a power of two and accumulating the counts of the pixels in the original projection. Table 2.1 shows the full width at half maximum values obtained from registering a Gaussian function to each reconstructed point source.

Mini-Deluxe Phantom™

3D images were reconstructed at varying projection count levels as shown in Figure 2.5. Attenuation was not modelled in the reconstruction of this phantom because it was considered to be negligible. The SNR in object space was estimated from $SNR = \mu_{\mathrm{FG}}/\sigma_{\mathrm{BG}}$, where μ_{FG} denotes the mean of the foreground and σ_{BG} denotes the standard deviation of the background. It is apparent that possible value correlations between the voxels are ignored using this formulation of the SNR, but the metric is still valid from a comparative standpoint. Two different foreground signals were chosen to estimate two different SNR values, namely the largest rods in the phantom (4.8 mm diameter) and the region with uniform activity at the bottom of the phantom. The empty space between the rods was chosen as the background signal. The SNR of the reconstructed images is shown in Figure 2.6 as a function of the total counts per projection.

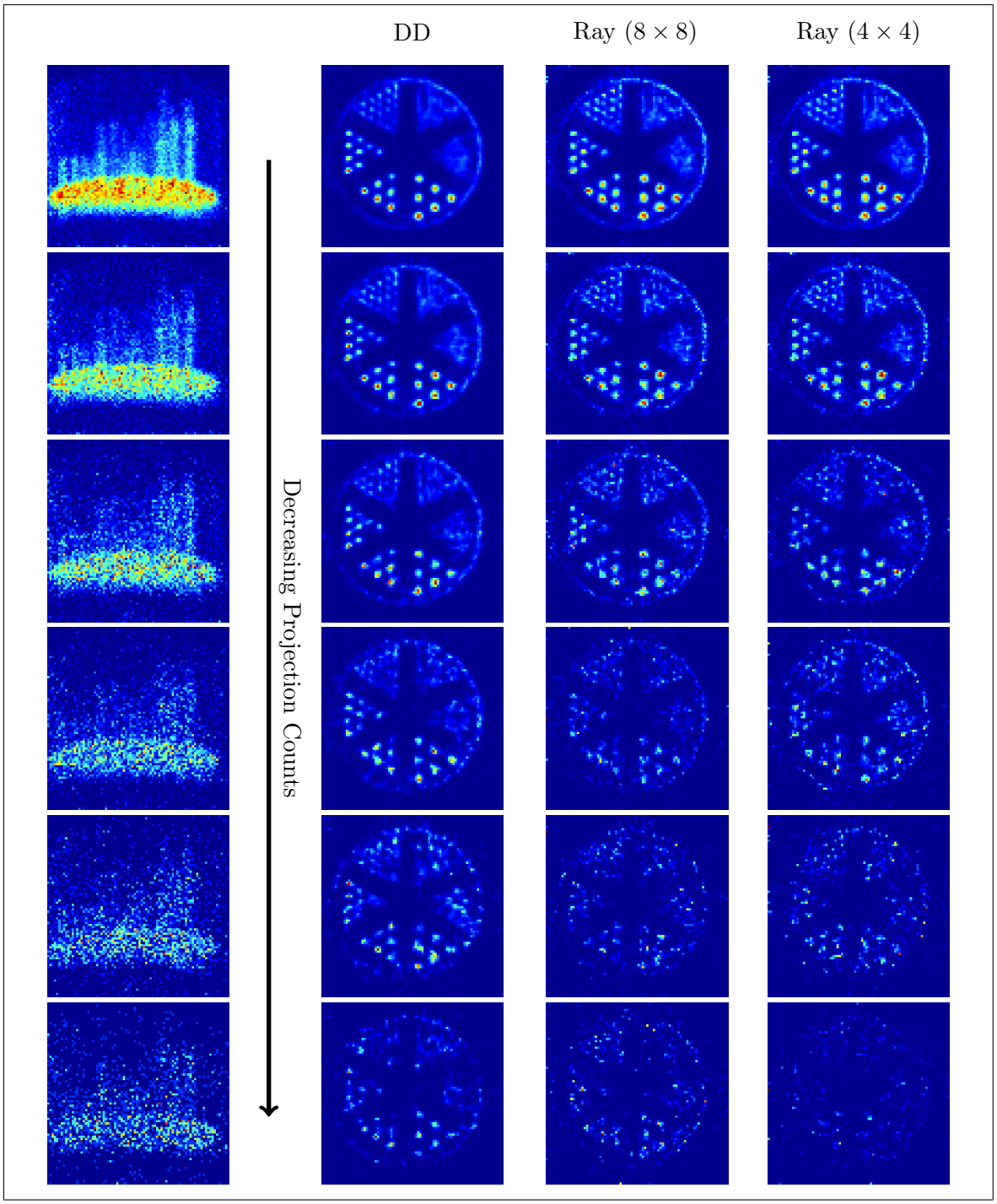

Figure 2.5: *Central axial slices of reconstructed Mini-Deluxe Phantom^{TM} employing distance and ray-driven projection methods: the left column shows example projections with decreasing counts from top to bottom, the second column shows the a cross-sectional slice of images reconstructed using the proposed distance-driven approach, while the rightmost two columns show the reconstructed slices obtained using the ray-driven approach with* 8×8 *and* 4×4 *pinhole sampling points. The color indicates intensity ranging from blue (low) to red (high).*

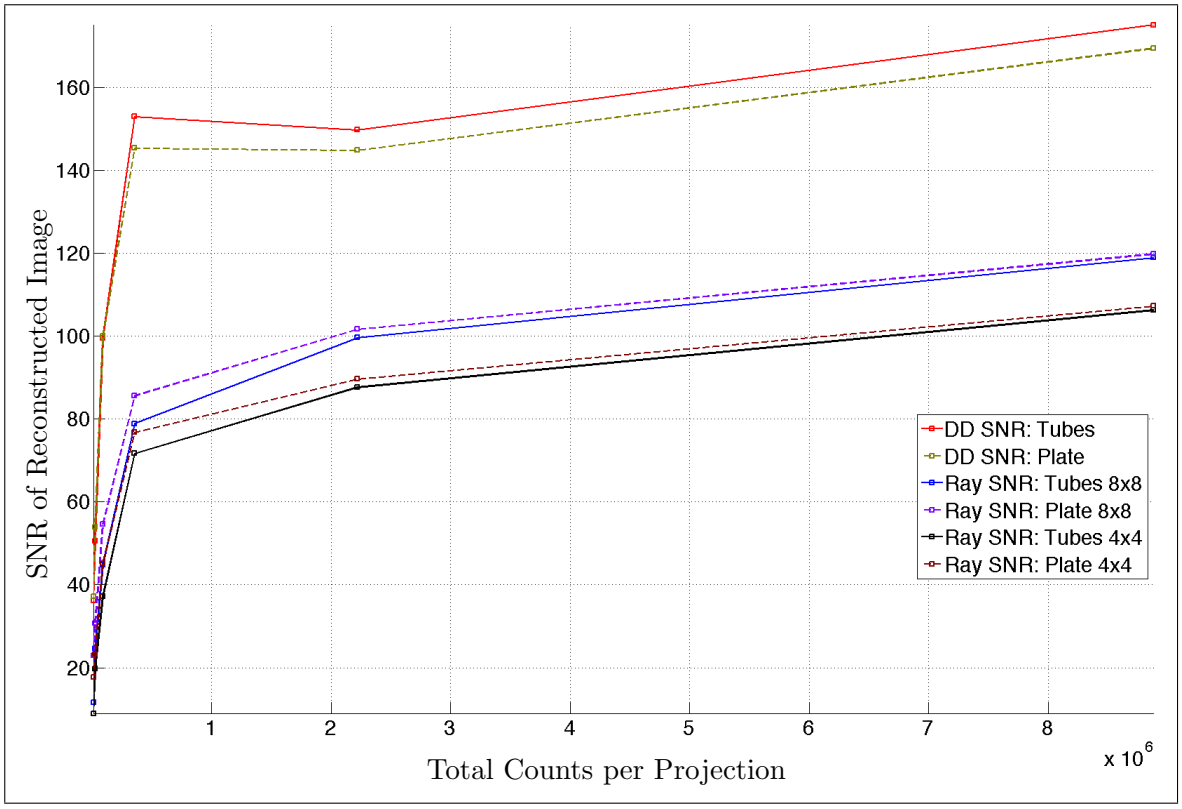

Figure 2.6: *The signal-to-noise ratio (SNR) of the reconstructed Mini-Deluxe Phantom^{TM} plotted against the total photon count per projection averaged over the set of projections. The plots show two SNR curves estimated from the variance of one background signal (empty space between rods) and the mean of two foreground signals (rods and uniform region). The solid lines show the SNR estimated from the mean of the largest rods (diameter = 4.8 mm), while the dashed lines show the SNR estimated from the uniform region at the bottom of the phantom.*

2.3 A Discussion of the Presented Results

2.3.1 Numerical and Visual Observations

The results obtained from the reconstructed phantoms show that the proposed distance-driven approach retains resolution and signal in the presence of noise better than a ray-driven approach of the same detector resolution at 8×8 or 4×4 pinhole sampling points.

The results listed in Table 2.1 indicate the following.

- The ratio of the FWHM between columns 2 and 3 of the cold-background point phantom, averaging a factor of 1.12, is smaller than the ratio between columns 4 and 5, averaging a factor of 1.53. This indicates that the distance-driven projection provides a better and more consistent estimate of the true FWHM at lower detector resolutions, where the true FWHM can be chosen (for instance) from the results of the ray-driven method listed in column 5.

- In the warm-background point source phantom, the effects of the background activity significantly alter the FWHM of the point sources in the ray-driven approach. The

FWHM obtained for the non-central point sources using the ray-driven approach are approximately 1.7 times larger in both coarse and fine discretizations of the detector than the ones obtained using the proposed distance-driven approach.

- Similarly, from columns 2 and 4 one can deduce that the distance-driven method is better suited for reconstructions at coarser detector discretizations. Let the relative error in the cold-background point source phantom be measured as

$$\epsilon_i = \frac{\text{FWHM}_i - \text{FWHM}_5}{\text{FWHM}_5} \tag{2.11}$$

  where i is the column number in Table 2.1, then $\epsilon_2 = 0.157$ and $\epsilon_4 = 0.529$ when averaged over the FWHM of the three point sources. In other words, the relative error of the distance-driven approach is much closer to the ray-driven approach at fine detector discretization than the ray-driven approach at coarse discretization.

- As expected, the FWHM values are similar for both projection methods when using a finely discretized detector surface (columns 3 and 5 in Table 2.1) in the case of the cold background point source phantom, however, the proposed distance-driven approach outperforms ray-driven when background activity is present.

The Mini-Deluxe Phantom$^{\text{TM}}$ experiment shows that reconstructed SNR is higher in the images obtained using the proposed distance-driven approach (see Figure 2.6). Figure 2.5, shows a more complete picture.

- Following the images from top to bottom, it is apparent that the proposed distance-driven approach preserves structure better in the presence of noise. This is due to its apparent "low-pass filtering" property which introduces more blurring in the images than the ray-driven method. The disadvantage of introducing blurring, however, is apparent in the left-most images since the rods in the sector at 11 o'clock appear more faded than those in the ray-driven cases. Figure 2.7, shows two profile lines of the Jaszczak-like phantom that emphasize two rows in the region at 11 o'clock. It is apparent that the blurring introduced by the distance-driven method can sometimes cause some loss of detail, however, it is also apparent that in cold regions the spatial variations are reduced.

- Following the images from left to right, it can be seen that the ray-driven method consistently provides seemingly sharper images in high-count regimes. In fact, the 4×4 ray-driven sampling is even sharper than the 8×8 ray-driven or the distance-driven. This is because when using a smaller sample of back-projection rays the activity is back-projected to fewer object voxels. However, there is a disadvantage to fewer pinhole samples since, as Figure 2.5 shows, the 4×4 ray-driven method exhibits greater loss of structural information in the presence of noise.

As a final remark we would like to state that one can "tweak" the proposed distance-driven approach to yield sharper images by sampling the pinhole at a radius smaller than that of the actual pinhole. In fact one can set a pinhole radius of zero for the proposed approach, thereby yielding an infinitely small pinhole, and computations would reduce to

intersections of polygons projected through a point. We have avoided presenting these scenarios since we wanted to approximate the physical system as best as we could, and without appealing to previous experience.

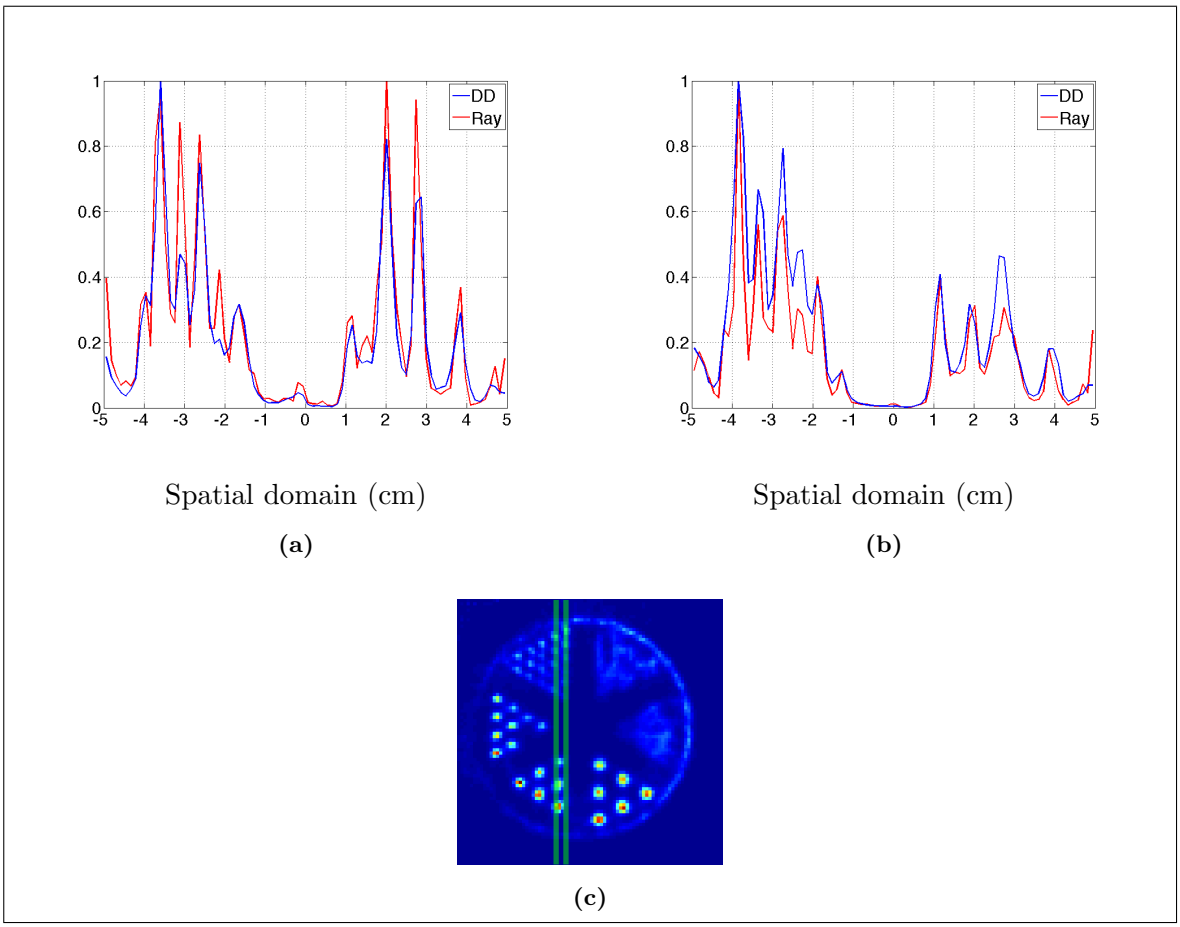

Figure 2.7: *Normalized profile lines of the reconstructed Mini-Deluxe Phantom^{TM} passing through the sections at 7 o'clock and 11 o'clock at two different slices. The lines are chosen to pass through the peaks of the section at 11 o'clock. The left and right slices (highlighted in green) shown in Figure (c) correspond to the profile plots in (a) and (b) respectively.*

The proposed method has a higher computational cost than the ray-driven approach since K (where $K \ll N$) polygon intersection calculations (which constitute the majority of the performance bottleneck) must be performed for each of the N object cells. However, because in the proposed method the backprojection operation is the transpose of the forward projection operation, the polygonal intersection calculations can be performed once for each detector head position and retained for later use. The main difference between the aforementioned approaches is that while the proposed distance-driven method is largely dependent on the number of object cells, the ray-driven approach is mostly dependent on the number of detector pixels. In the instance of the Mini-Deluxe Phantom$^{\text{TM}}$ reconstructions, the distance driven approach takes an average of 30 seconds to forward project (back-project) the object on (or from) 8 detector heads. In comparison, the ray-driven approach takes on

average 4 seconds to forward project and 19 seconds to backproject based on an 8×8 pinhole surface samples.

Provided that in SPECT imaging the discretization the detector surface is coarse (e.g. 64×64 or 128×128) then the discretization of the object space can also be coarse; typically about the same order of voxels in the plane of rotation if we consider a magnification factor of one since finer discretizations may not show any additional information. An argument commonly used in favour of ray-driven projection is that one can greatly increase the number of bins in the detector in order to obtain better quality images at a relatively small computational cost. However, in SPECT imaging, the detector discretization is typically coarse, and the acquired projections always contain noise making the task of interpolating the acquired data onto a finely discretized detector non-trivial. Using the proposed approach, one need not artificially increase the number of detector bins during reconstructions.

As a final remark, we would like to acknowledge that attenuation correction has not been treated in this research. We maintain, however, that with the proposed method, the attenuation factors can be estimated separately as a pre-processing step since these are not directly tied to the estimation of the overlapping factors, and multiplied to the overlap factors for each projected cell.

2.3.2 Future Work and Possible Improvements

Incorporating Aperture Penetration An important aspect of the single-pinhole geometry that has not been addressed in this work is aperture penetration. While exact formulae for aperture penetration would be difficult to implement in the proposed distance-driven approach without venturing into projection methods using separable footprint, a simpler method using a weighted distance-driven approach may still be suitable. Specifically, we propose to sample the pinhole at multiple radii (above the pinhole radius) and weigh the contribution to detector bins by the probability of penetrating the collimator material at the sampled radius.

For example, let us sample a circular pinhole at the pinhole radius and the *effective pinhole radius* [1, 51, 57] as shown in Figure 2.8. Let us assume that the probability of penetrating the pinhole is $p = 1$, while the probability of penetrating the collimator between the pinhole radius, r, and effective radius, r_{eff}, can be approximated by a uniform probability p_{eff}, then the intensity contribution from object cell f_i to bin j is computed as

$$g_j = \omega_{i,j} f_i (1 - p_{\text{eff}}) + \omega_{i,j}^{\text{eff}} f_i p_{\text{eff}}.$$

where $\omega_{i,j}$ and $\omega_{i,j}^{\text{eff}}$ are the overlapping ratios computed from the pinhole radius and effective pinhole radius respectively.

The computational cost of sampling the pinhole at multiple radii is equivalent to performing multiple projections at the same geometric configuration since the overlap ratios must be estimated for each of the sampled radii.

Improving Execution Time In the current form, the proposed distance-driven approach relies on polygon intersection algorithms to estimate the overlap ratio between projected object cells and detector bins. While this approach may be suitable for coarse discretizations

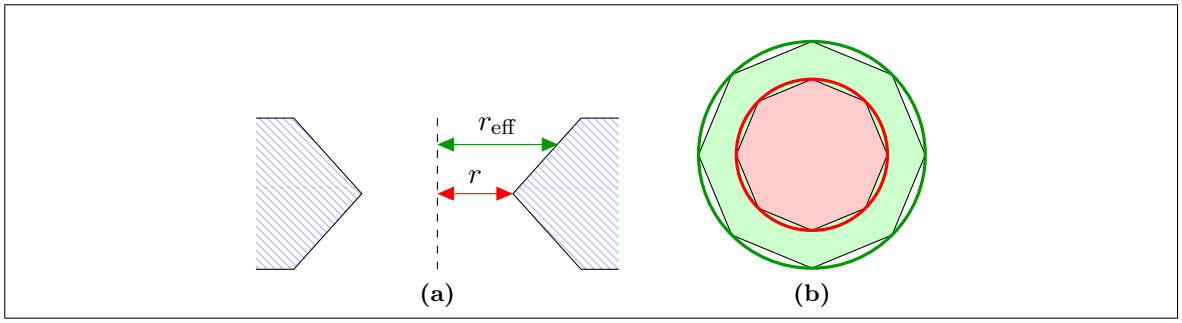

Figure 2.8: *Cross-sectional (a) and top-view (b) of pinhole showing the pinhole radius, r, and effective radius, r_{eff}. The green and red arrows in the cross-sectional view correspond by color to the inner and outer circles in the top-view figure. Figure (b) shows the sampling of the pinhole at the radius and effective radius using a regular octagon.*

of the object and detectors (e.g $\approx 80^3$ voxels and 80^2 bins as used in the experiment) as it provides an exact estimation of the overlap ratio for the geometric entities provided, it becomes computationally infeasible at finer discretizations (e.g. 256^3 voxels and 1024^2 bins) which may be used to provide better approximations of coarser grids. However, there are reasonable approximations that can be made at finer discretizations which can dramatically improve computation time.

One natural approximation is to move away from the concept of polygon intersection and instead exploit the regularity of the detector bins by using the concept of rasterization. Specifically, given a polygon representing a projected object cell we assign an overlap ratio of 1 or 0 by deciding whether a bin is inside or outside the polygon. Of course, there will be bins which will only partially fall inside the polygon, but one can pick a point in the bin (e.g. the bin centre) and use it to decide whether the bin is inside or outside the polygon (see Figure 2.9).

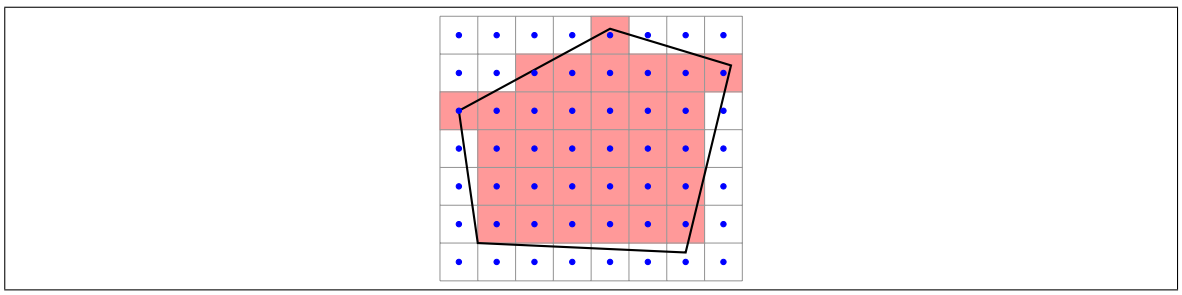

Figure 2.9: *The proposed rasterization considers the central points of each detector bin (blue) and assigns an overlap ratio of 1 or 0 based on whether these points are inside the polygon or not. In this figure, the bins highlighted in red are considered to fall within the polygon and are therefore assigned an overlap ratio of 1.*

While this strategy reduces the complexity of the computations by removing dependency from the detector bin edges, it also has the added advantage of being highly parallelizable (i.e. easily implementable in graphical processing units) since only one element in the bin (the central point) is considered.

2.3.3 Summary

This chapter described a distance-driven approach for pinhole SPECT imaging accounting for a finite pinhole size and possibly tilted detector surface. The proposed method restricts the shape of the object cells used to discretize the object space to convex polyhedrons, which comes at a higher computational cost due to numerous polygon intersection calculations. Our experiments show that the FWHM resulting from the reconstructed point-source phantom are consistently smaller in the distance-driven approach. Additionally, there is a smaller difference in FWHM at different detector discretizations in the proposed method. The proposed distance-driven approach also shows better preservation of structure in low-count regimes.

Chapter 3

Image Reconstruction Methods Employing Kernel Density Estimators for Denoising

Recent years have seen an increase and expansion in the use of dynamic single-photon emission computed tomography (SPECT) for the diagnosis of various cardiac conditions. Significant advances have been made in the past decade in terms of the advancement of the imaging devices and the mathematical modelling relating to the image reconstruction algorithms and data representation (see [35] for a review). The introduction of solid-state organ-specific SPECT imaging systems, such as the GE Discovery NM 530c [7], have enabled dynamic SPECT imaging of the heart through arrays of small pinhole collimator cameras. Such imaging systems offer some advantages in terms of imaging speed and sensitivity, however, low signal-to-noise ratio (SNR) remains a challenge due to its dependence on a combination of factors including washout rapidity of radioactive tracers, the length of acquisition per time-frame, and gated imaging.

The problem of dynamic image reconstruction from noisy data has been addressed in a number of ways in literature which can be categorized into

- **object model based reconstruction**, where the object data representation model includes the correlation of activities between time-frames (either by using temporal basis functions [64], or by assuming a compartmental model or basis for a compartmental model [36,38]), while the image reconstruction method itself performs no penalization, and
- **penalty based reconstruction**, where the object model does not model the correlation of activities between time-frames, and instead the image reconstruction method penalizes "undesired" behaviour in the time-activity functions [27, 28, 33, 47],
- or a combination of the two.

In this chapter, we present two novel dynamic *maximum a posteriori* (MAP) image reconstruction methods for emission tomography: one which uses a *kernel density estimator* (KDE) [30,61,67] to model the prior distribution, and one that employs a Gaussian prior in which the mean is determined from mean-shift filtering [15,16] at each MAP iteration. The aim is to regularize the behaviour of the time-activity functions in each voxel by clustering similar time-activity functions (TAF) during the process of reconstruction.

We employ temporal basis functions [64] for object representation to both compress the temporal object from a possibly large number of acquisition time-frames to a relatively small number of temporal spline coefficients, and to regularize the behaviour of the TAFs by correlating the activity in adjacent time-frames as dictated by the chosen temporal spline basis.

3.1 Kernel Density Estimators and Mean-shift Filtering

In this section, an overview of the kernel density estimators and its application to image denoising is first presented. A detailed explanation of the proposed dynamic MAP image reconstruction and how the KDE is embedded in the prior follows.

Kernel density estimators were initially introduced to find a solution to the problem of estimating the probability density function and mode of a sequence of independent identically distributed random variables in a non-parametric way [61]. Specifically, the probability density function of a sequence of observations $X_1, \ldots, X_n$ is represented by the weighted sum of kernel functions

$$p_n(x) = \frac{1}{nh} \sum_{j=1}^{n} \mathcal{K}\left(\frac{x - X_j}{h}\right)$$

where h is a positive scalar, known as a *scaling parameter*.

Kernel density estimators have also been applied to pattern recognition, where the gradients of the distribution are used to perform data clustering and filtering [16,30] giving rise to mean-shift filtering as a method of image denoising. Mean-shift filtering, as the name describes, clusters data locally using the gradient of the kernel density estimator to shift points toward a local mean, dictated by the scaling parameter h, thereby maximizing the distribution and effectively reducing dimensionality.

Let us now, provide a short overview of mean-shift filtering applied to a multidimensional image, in order to obtain a better understanding of how image data is denoised in object space.

Let each time-activity curve in the object space be represented by a fixed number of temporal splines S, (cf. [64]) and let us denote the unknown coefficients of the temporal splines in each voxel by $c_{[j]} \in \mathbb{R}^S$, $j = 1, \ldots, N$. Furthermore, let the locations of the temporal spline coefficients be denoted by $x_{[j]} \in \mathbb{R}^d$. Then, the probability density measured from some point $(y_{[i]}, \mu_{[i]}) \in \mathbb{R}^{S+d}$, where $\mu_{[i]} \in \mathbb{R}^S$ is situated at location $y_{[i]} \in \mathbb{R}^d$, can be represented by a *multivariate kernel density estimator* [30, 61] with kernel $\mathcal{K}$ as

$$p(y_{[i]}, \mu_{[i]}) = \frac{1}{N h_{\mu,i}^S h_{y,i}^d} \sum_{j=1}^{N} \mathcal{K}\left(\frac{\mu_{[i]} - c_{[j]}}{h_{\mu,i}}\right) \mathcal{K}\left(\frac{y_{[i]} - x_{[j]}}{h_{y,i}}\right) \tag{3.1}$$

where $h_{\mu,i}$ is a positive scalar representing the range scaling parameter, and $h_{y,i}$ is a positive scalar representing the spatial scaling parameter.

While one may choose from a multitude of kernels fulfilling certain conditions (see [12,30]), for this example we have chosen a Gaussian function as the kernel,

$$\mathcal{K}(v) = (2\pi)^{-d/2} \exp\left(-\frac{1}{2} \|v\|_2^2\right). \tag{3.2}$$

Therefore equation (3.1) can be written as

$$p(y_{[i]}, \mu_{[i]}) = \frac{(2\pi)^{-\frac{S+d}{2}}}{N h_{\mu,i}^S h_{y,i}^d} \sum_{j=1}^{N} \exp\left(-\frac{1}{2} \left\| \frac{\mu_{[i]} - c_{[j]}}{h_{\mu,i}} \right\|^2\right) \exp\left(-\frac{1}{2} \left\| \frac{y_{[i]} - x_{[j]}}{h_{y,i}} \right\|^2\right). \tag{3.3}$$

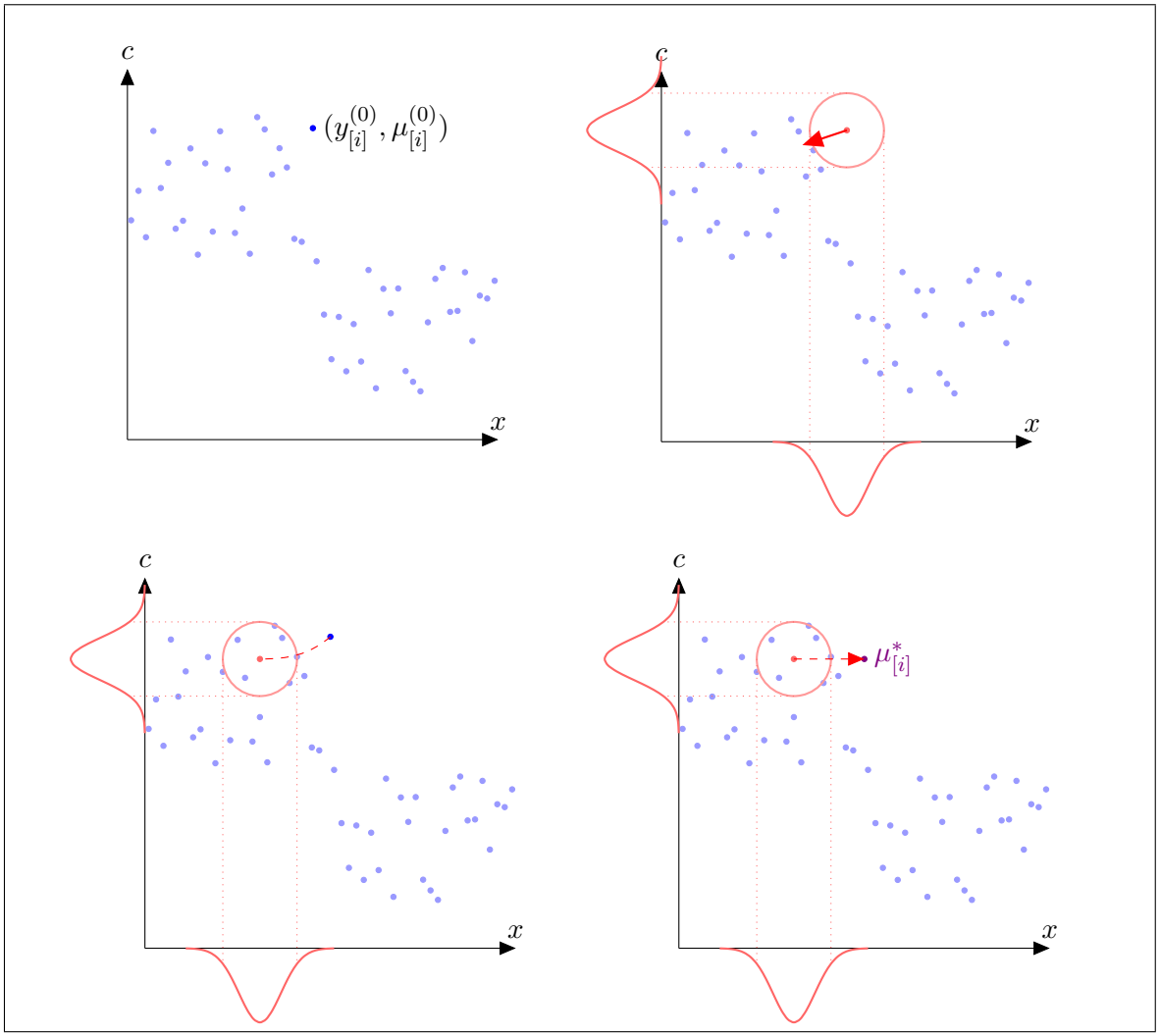

Figure 3.1: *A schematic example of mean shift filtering on a one-dimensional image where the intensity values $c_{[i]}$ are situated at points $x_{[i]}$: (a) in the original image the initial guess is $(y_{[i]}^{(0)}, \mu_{[i]}^{(0)}) = (x_{[i]}, c_{[i]})$, (b) the "net-force" as dictated by the scaling parameters in the kernel wants to shift the points toward nearby points, (c) the point shifts until the "net-force" is zero, (d) the new (mean-shifted) value replaces the initial one at the original spatial location. The procedure is repeated for each of the points in the original image.*

Taking the derivatives with respect to $y_{[i]}$ and $\mu_{[i]}$ of equation (3.3), an iterative scheme known as "mean-shift filtering" that shifts the respective initial values $y_{[i]}^{(0)}$ and $\mu_{[i]}^{(0)}$ toward a local mean is obtained. As shown in Algorithm 3.1, if the initial values are set at the measured points, that is $y_{[i]}^{(0)} = x_{[i]}$, $\mu_{[i]}^{(0)} = c_{[i]}$, and the iterative procedure is applied to each voxel $i = 1, \ldots, N$, then one effectively obtains an image denoising method. Figure 3.1 provides a schematic view of Algorithm 3.1 for a one-dimensional image.

It is apparent that mean-shift filtering, when applied in the object space, will shift each temporal spline coefficients in each voxel toward a local mean determined by the spatial

Algorithm 3.1 Mean-shift Filtering (MSF).

1: Let the input temporal spline coefficients $c_{[i]} \in \mathbb{R}^S$ be located at $x_{[i]} \in \mathbb{R}^d$, $i = 1, \ldots, N$.
2: **for** i=1,...,N **do**
3: $k \leftarrow 0$
4: $\mu_{[i]}^{(k)} \leftarrow c_{[i]}$, $y_{[i]}^{(k)} \leftarrow x_{[i]}$
5: **repeat**
6:
$$\mu_{[i]}^{(k+1)} = \frac{\sum_{j=1}^{N} c_{[j]} \exp\left(-\frac{1}{2}\left\|\frac{\mu_{[i]}^{(k)} - c_{[j]}}{h_{\mu,i}}\right\|^2\right) \exp\left(-\frac{1}{2}\left\|\frac{y_{[i]}^{(k)} - x_{[j]}}{h_{y,i}}\right\|^2\right)}{\sum_{j=1}^{N} \exp\left(-\frac{1}{2}\left\|\frac{\mu_{[i]}^{(k)} - c_{[j]}}{h_{\mu,i}}\right\|^2\right) \exp\left(-\frac{1}{2}\left\|\frac{y_{[i]}^{(k)} - x_{[j]}}{h_{y,i}}\right\|^2\right)}$$
7:
$$y_{[i]}^{(k+1)} = \frac{\sum_{j=1}^{N} x_{[j]} \exp\left(-\frac{1}{2}\left\|\frac{\mu_{[i]}^{(k)} - c_{[j]}}{h_{\mu,i}}\right\|^2\right) \exp\left(-\frac{1}{2}\left\|\frac{y_{[i]}^{(k)} - x_{[j]}}{h_{y,i}}\right\|^2\right)}{\sum_{j=1}^{N} \exp\left(-\frac{1}{2}\left\|\frac{\mu_{[i]}^{(k)} - c_{[j]}}{h_{\mu,i}}\right\|^2\right) \exp\left(-\frac{1}{2}\left\|\frac{y_{[i]}^{(k)} - x_{[j]}}{h_{y,i}}\right\|^2\right)}$$
8: $k \leftarrow k + 1$
9: **until** convergence **or** stopping criteria are met
10: **end for**
11: Place values $\mu_{[i]}^{(k)}$ in original locations $x_{[i]}$, and output $\mu_{[i]}^{(k)}$.

and range scaling parameters $h_{\mu,i}$ and $h_{y,i}$.

Let us now explain the details of formulating a MAP image reconstruction method that clusters intensity values (or time-activity functions) during the reconstruction process. In the next section, the details of constructing an optimization problem based on a maximum a posteriori formulation are presented. This is followed by the details of the priors for each of the proposed reconstruction methods and the resulting iterative algorithms.

3.2 Constructing an Image Reconstruction from a Maximum A Posteriori Formulation

Let us "stack" the aforementioned temporal spline coefficients $c_{[i]} \in \mathbb{R}^S$ such that $c \in \mathbb{R}^{NS}$. Given an imaging system with K (static) heads, each discretized into M bins, with T acquisition time-frames, one obtains ideal measurements $g \in \mathbb{R}^{MKT}$ through a projection matrix $F \in \mathbb{R}^{MKT \times NS}$ as $g = Fc$, where F models both the physical imaging system and the temporal splines.[1]

To formulate the image reconstruction problem in a maximum a posteriori framework we measure the posterior probability as

$$p(g|c) \propto p(c|g)p(c)$$

[1] A detailed explanation of the operator F is provided in Section 3.4.2.

where $p(c|g)$ is the likelihood, and $p(c)$ is the prior probability. The image reconstruction method can then be obtained by solving

$$\begin{aligned} \max_{c} \quad & \log p(g|c) + \log p(c) \\ \text{s.t.} \quad & c \succeq 0 \end{aligned} \tag{3.4}$$

where $p(g|c)$ is justifiably assumed for emission tomography to be the Poisson likelihood.

If one considers the unmeasurable quantities (i.e. complete data), z_{ij}, of photons emitted from voxel i and detected in bin j then problem (3.4) can be modified to

$$c^{(k+1)} \in \arg\max_{c} E_z[\log p(z|c)|c^{(k)}, g] + \log p(c), \tag{3.5}$$

where $E_z[\cdot|c^{(k)}, g]$ is the conditional expectation over z given the estimate at the previous iteration $c^{(k)}$ and the measurements g, and the Poisson log-likelihood takes the form

$$\log p(z|c) = \sum_{i=1}^{NT} \sum_{j=1}^{MKT} \left(-F_{ji}c_i + z_{ij} \log\left(F_{ji}c_i\right)\right) \tag{3.6}$$

with c_i as the i-th element of the vector c. It is worth noting that problem (3.5) is a proximal algorithm [60] formulation of (3.4), as it relies on a previous estimate $c^{(k)}$, that is derived by minorizing the log-likelihood $\log p(g|c)$ [21, 39].

Looking more closely at the first term in equation (3.5), we have

$$E_z\left[\log p(c|z)|c^{(k)}, g\right] = \sum_{i=1}^{NS} \sum_{j=1}^{MKT} \left(\frac{g_j F_{ji} c_i^{(k)}}{\sum_{i'=1}^{NS} F_{ji'} c_{i'}^{(k)}} \log(F_{ji}c_i) - F_{ji}c_i\right), \tag{3.7}$$

which is obtained by realizing that the conditional expectation of the complete (unmeasurable) data z_{ij} given the measurements g and the image $c^{(k)}$ is

$$E_z\left[z_{ij}|g, c^{(k)}\right] = \frac{g_j F_{ji} c_i^{(k)}}{\sum_{i'=1}^{NS} F_{ji'} c_{i'}^{(k)}} \tag{3.8}$$

since the z_{ij} are multinomially distributed given the measurements g. Specifically, in (3.8), g_j represents the number of trials and

$$\frac{F_{ji} c_i^{(k)}}{\sum_{i'=1}^{NS} F_{ji'} c_{i'}^{(k)}}$$

is the probability of an event from object voxel i being measured in bin j. The reader may refer to [45, 49] for the complete details of the derivation described above.

In light of the above, let us write the optimization problem in (3.5) in a more detailed fashion for future reference,

$$c^{(k+1)} \in \arg\max_{c} \sum_{i=1}^{NS} \sum_{j=1}^{MKT} \left(\frac{g_j F_{ji} c_i^{(k)}}{\sum_{i'=1}^{NS} F_{ji'} c_{i'}^{(k)}} \log(F_{ji}c_i) - F_{ji}c_i\right) + \log p(c). \tag{3.9}$$

The prior probability in this last equation will be explored in detail the next two sections where we propose a Gaussian prior and a KDE-based prior, both of which measure proximity to an iterate $c^{(k)}$, but take different approaches.

3.3 A Detailed Explanation of the Proposed Prior Probabilities

3.3.1 An Image Reconstruction Algorithm Employing Mean-Shift Filtering for Denoising

In order to penalize spatio-temporal variation introduced by noise, we would like to incorporate the results of the mean-shift algorithm in the prior and formulate the reconstruction problem as a proximal algorithm.

A well-known form of a proximal algorithm is the *disappearing Tikhonov regularization* [60, Section 4.1.1] which takes the form

$$\min_x \left\{ f(x) + \frac{1}{2\lambda} \left\| x - x^{(k)} \right\|^2 \right\}, \tag{3.10}$$

where the first term is an objective function and the second term is a quadratic Tikhonov penalty around the previous iterate $x^{(k)}$.

Following the disappearing Tikhonov regularization, we introduce a prior that takes the form

$$p(c) = p(c; \mu^{(k)}) = \exp\left(-\frac{1}{2} \left\| \frac{c - \mu^{(k)}}{\sigma^2} \right\|^2 \right) \tag{3.11}$$

where $\mu^{(k)} = \mathrm{MSF}(c^{(k)})$ is a mean-shift denoised version of $c^{(k)}$ obtained from Algorithm 3.1, c represents the unknown temporal spline coefficient image, and σ is a scalar.

In light of the chosen prior, the maximization problem shown in (3.9) takes the form

$$c^{(k+1)} \in \arg\max_c \sum_{i=1}^{NS} \sum_{j=1}^{MKT} \left(\frac{g_j F_{ji} c_i^{(k)}}{\sum_{i'=1}^{NS} F_{ji'} c_{i'}^{(k)}} \log(F_{ji} c_i) - F_{ji} c_i \right) - \frac{1}{2} \left\| \frac{c - \mu^{(k)}}{\sigma^2} \right\|^2 \tag{3.12}$$

From here, we find the first order conditions for optimization with respect to c,

$$\left(\frac{c - \mu}{\sigma^2} : c \right) + \left(F^\top \vec{1}_{MKT} : c \right) - \left(c^{(k)} : F^\top \left(\frac{g}{F c^{(k)}} \right) \right) = 0 \tag{3.13}$$

where the operator ":" denotes component-wise multiplication, and $\vec{1}_{MKT} \in \mathbb{R}^{MKT}$ is a vector of ones.

Because equation (3.13) is a quadratic equation and all operations are component-wise, the system can be solved using

$$c^{(k+1)} = \frac{1}{2} \left(-\sigma^2 F^\top \vec{1}_{MKT} + \mu^{(k)} + \sqrt{(\sigma^2 F^\top \vec{1}_{MKT} - \mu^{(k)})^2 + 4\sigma^2 c^{(k)} : F^\top \left(\frac{g}{F c^{(k)}} \right)} \right) \tag{3.14}$$

where again the operator ":" denotes component-wise multiplication, and $\vec{1}_{MKT} \in \mathbb{R}^{MKT}$ is a vector of ones. Notice that the solution proposed here greatly resembles that proposed in [45], with the main difference appearing in the prior whereby the proposed method makes no assumptions about an underlying compartmental model.

Equipped with equation (3.14) and Algorithm 3.1, we propose an iterative solution to the proposed dynamic image reconstruction problem as shown in Algorithm 3.2. For simplicity in the rest of this paper we will address the MAP method proposed here as MAPMS.

Algorithm 3.2 Proposed MAP Iterative Scheme (MAPMS).

1: Set $k \leftarrow 0$.
2: Obtain an initial guess $c^{(k)}$ by performing one or more EM iterations, or set manually.
3: Let $x \in \mathbb{R}^{Nd}$ represent the locations of the temporal spline coefficients of image $c^{(k)} \in \mathbb{R}^{NS}$.
4: **repeat**
5: $\mu^{(k)} \leftarrow \mathbf{MSF}(c^{(k)}, x)$ [as per Algorithm 3.1].
6: $c^{(k+1)} = \frac{1}{2}\left(-\sigma^2 F^\top \vec{1}_{MKT} + \mu^{(k)} + \sqrt{(\sigma^2 F^\top \vec{1}_{MKT} - \mu^{(k)})^2 + 4\sigma^2 c^{(k)} : F^\top \left(\frac{g}{Fc^{(k)}}\right)}\right)$.
7: $k \leftarrow k + 1$
8: **until** convergence **or** stopping criteria are met
9: Output: $c^{(k)}$.

Convergence Analysis

A thorough theoretical convergence analysis of MAPMS remains to be performed. Algorithm 3.2 exhibits *apparent convergence* since for all parameters σ in our simulations $\left\|c^{(k+1)} - c^{(k)}\right\| \leq \left\|c^{(k)} - c^{(k-1)}\right\|$, where k is the iteration number (see Figure 3.2 for an example).

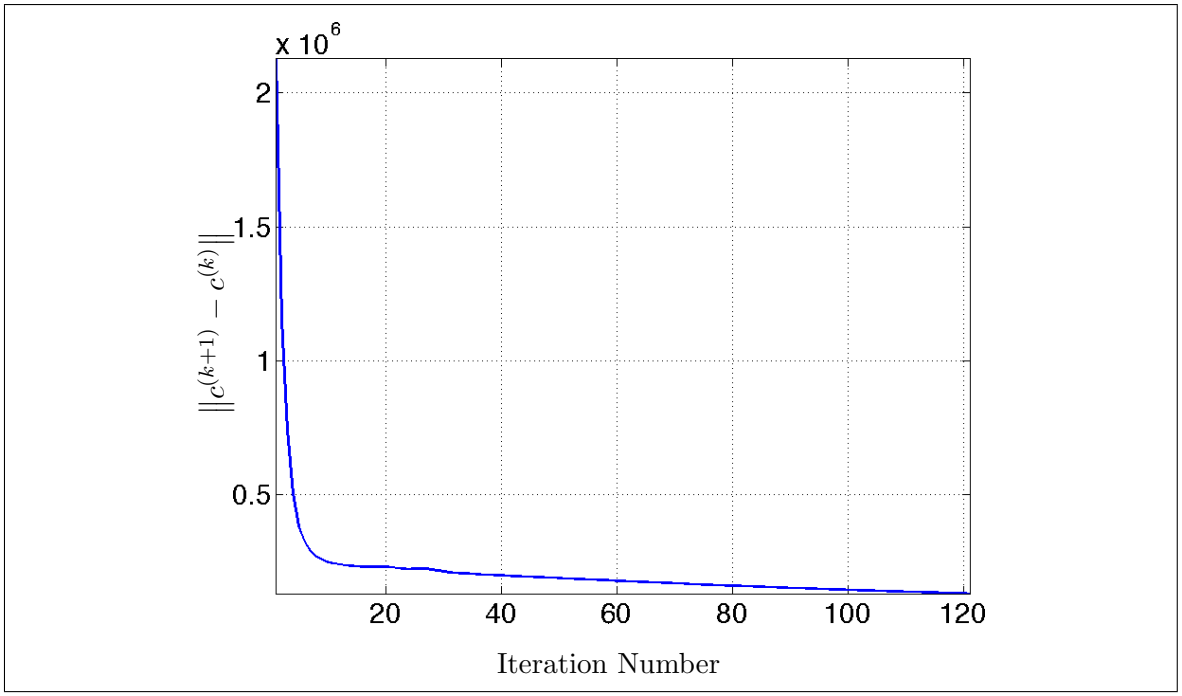

Figure 3.2: *An example of the distance between consecutive iterates in MAPMS as a function of the iteration number measured by the l_2-norm.*

Experimentally, we have found that the constraint $c \succeq 0$ holds for all tested values

of σ. This was expected since, if we analyze Line 6 of Algorithm 3.2, we find that

$$(-\sigma^2 F^\top \vec{1}_{MKT} + \mu^{(k)})^2 \preceq (\sigma^2 F^\top \vec{1}_{MKT} - \mu^{(k)})^2 + 4\sigma^2 c^{(k)} : F^\top \left(\frac{g}{Fc^{(k)}}\right) \tag{3.15}$$

always holds due to the fact that $\mu^{(k)} \succeq 0$ since mean-shift denoising shifts the values $c^{(k)}$ to local means within the range of $c^{(k)}$, and the term

$$4\sigma^2 c^{(k)} : F^\top \left(\frac{g}{Fc^{(k)}}\right) \succeq 0 \quad \forall c^{(k)} \succeq 0.$$

We conjecture that MAPMS should converge for all σ. If σ is very small each iterate $c^{(k)}$ will strongly tend toward $\mu^{(k)}$ and therefore mean-shift will "dominate" the algorithm. Since mean shift is a robust method for image denoising [16] and will always converge given a valid kernel, then the iterates $c^{(k)}$ will also converge. In the extreme case, $\sigma = 0$ yields $c^{(k)} = \mu^{(k)}$.

On the other hand, for very large σ the term $\mu^{(k)}$ will become comparatively insignificant and the iterations will appear as

$$c^{(k+1)} = \frac{1}{2}\left(-\sigma^2 F^\top \vec{1}_{MKT} + \sqrt{(\sigma^2 F^\top \vec{1}_{MKT})^2 + 4\sigma^2 c^{(k)} : F^\top \left(\frac{g}{Fc^{(k)}}\right)}\right) \tag{3.16}$$

which is the solution to the quadratic equation

$$(c^{(k+1)})^2 + \sigma^2 c^{(k+1)} : F^\top \vec{1}_{MKT} - \sigma^2 c^{(k)} : F^\top \left(\frac{g}{Fc^{(k)}}\right) = 0. \tag{3.17}$$

Assuming that the first term in (3.17) can be dropped for very large σ then we would obtain

$$c^{(k+1)} = \frac{c^{(k)}}{F^\top \vec{1}_{MKT}} : F^\top \left(\frac{g}{Fc^{(k)}}\right),$$

which effectively reduces MAPMS to expectation maximization (EM).

Mean-shift Filtering: Scaling Parameters and Computation

An important aspect of the proposed image reconstruction method is choosing the scaling parameters for mean-shift filtering ($h_{y,i}$, $h_{\mu,i}$). One may choose these parameters manually, however, through experiments we found that there are alternatives to choosing the scaling parameters.

Full-width at Half Maximum (FWHM) Strategy Let us set $h_{y,i} = h_y$, where h_y is defined by the user, and define

$$\chi_i = \{j : \left\|x_{[i]} - x_{[j]}\right\| \leq 2\sqrt{2\ln 2} h_y\}.$$

Also, let the distance between two time-activity curves be defined by the distance of the temporal spline coefficients (since the two are related by a scaling factor) as

$$d_{i,j} = \left\|c_{[i]} - c_{[j]}\right\| \text{ for } j \in \chi_i$$

with mean

$$m_i = \frac{1}{|\chi_i|} \sum_{j \in \chi_i} d_{i,j},$$

then the range scaling parameter is set to

$$h_{\mu,i} = \sqrt{\frac{1}{|\chi_i|} \sum_{j \in \chi_i} (d_{i,j} - m_i)^2}. \tag{3.18}$$

k-nearest Neighbours (kNN) Strategy Let us introduce a positive integer k (set by the user) such that χ_i is the set of size k of the indices of points $x_{[j]}$ closest to $x_{[i]}$ in an ℓ_2 sense. Let us also define the distance measures

$$d_{x,i,j} = \left\| x_{[i]} - x_{[j]} \right\|, \quad d_{c,i,j} = \left\| c_{[i]} - c_{[j]} \right\|$$

with means

$$m_{x,i} = \frac{1}{k} \sum_{j \in \chi_i} d_{x,i,j}, \quad m_{c,i} = \frac{1}{k} \sum_{j \in \chi_i} d_{c,i,j},$$

then the spatial and range scaling parameters can be computed from

$$\begin{aligned} h_{x,i} &= \sqrt{\frac{1}{k} \sum_{j \in \chi_i} (d_{x,i,j} - m_{x,i})^2}, \\ h_{c,i} &= \sqrt{\frac{1}{k} \sum_{j \in \chi_i} (d_{c,i,j} - m_{c,i})^2}. \end{aligned} \tag{3.19}$$

All MAPMS reconstructions presented in Section 3.4.2 have been obtained using the aforementioned FWHM strategy.

3.3.2 An Image Reconstruction Algorithm with a Kernel Density Estimator Based Prior

Let us now model the prior probability, $p(c)$, in (3.9) by the kernel density estimator shown in (3.3) in the form of a proximal algorithm [60]. That is, we measure the probability density of the unknown temporal spline coefficients, $c_{[i]} \in \mathbb{R}^S$, spatially located at $y_{[i]} \in \mathbb{R}^d$ to neighbouring components of a previous estimate, $c^{(k)}_{[j]}$, an their corresponding locations by

$$p(y_{[i]}, c_{[i]}; y^{(k)}_{[i]}, c^{(k)}_{[i]}) = \frac{(2\pi)^{-\frac{S+d}{2}}}{N h^S_{c,i} h^d_{y,i}} \sum_{j=1}^{N} G(c_{[i]}, c^{(k)}_{[j]}) G(y_{[i]}, y^{(k)}_{[j]}) \tag{3.20}$$

where

$$G(x_i, x_j) = \exp\left(-\frac{1}{2} \left\| \frac{x_i - x_j}{h_{x,i}} \right\|^2 \right). \tag{3.21}$$

Then the prior takes the form

$$p(y, c; c^{(k)}, y^{(k)}) = \prod_{i=1}^{N} p(y_{[i]}, c_{[i]}), \tag{3.22}$$

and the log-prior, in turn, becomes

$$\log p(y, c; c^{(k)}, y^{(k)}) = \sum_{i=1}^{N} \log \left(\frac{(2\pi)^{-S/2}}{N h_{c,i}^{S} h_{y,i}^{d}} \right) + \sum_{i=1}^{N} \log \left(\sum_{j=1}^{N} G(c_{[i]}, c_{[j]}^{(k)}) G(y_{[i]}, y_{[j]}^{(k)}) \right). \quad (3.23)$$

Since we also want to solve for the spatial locations $y \in \mathbb{R}^{Nd}$ of the coefficients $c \in \mathbb{R}^{NS}$ then problem (3.5) becomes

$$(c^{(k+1)}, y^{(k+1)}) \in \arg\max_{c,y} E_z[\log p(z|c)|c^{(k)}, g] + \log p(y, c; c^{(k)}, y^{(k)}). \quad (3.24)$$

To find a solution to (3.24) the first order conditions for optimization must be satisfied, that is

$$\partial_{c_{[i]}} E_z \left[\log p(c|z)|c^{(k)}, g \right] + \partial_{c_{[i]}} \log p(y, c) = 0, \quad (3.25)$$

$$\partial_{y_{[i]}} \log p(y, c) = 0. \quad (3.26)$$

The solution to (3.26) results in mean-shift iterations, while the solution to (3.25) is obtained from

$$c_{[i]}^2 + c_{[i]} : \left(\left(F^\top \vec{1}_{MKT} \right)_{[i]} - \frac{\sum_{j=1}^{N} c_{[j]}^{(k)} G(c_{[i]}^{(k)}, c_{[j]}^{(k)}) G(y_{[i]}^{(k)}, y_{[j]}^{(k)})}{\sum_{j=1}^{N} G(c_{[i]}^{(k)}, c_{[j]}^{(k)}) G(y_{[i]}^{(k)}, y_{[j]}^{(k)})} \right) - c_{[i]}^{(k)} : \left(F^\top \frac{g}{F c^{(k)}} \right)_{[i]} = 0 \quad (3.27)$$

for $i = 1, \ldots, N$. Here, the operator ":" denotes component-wise multiplication, division is performed component-wise, and the operator $(\cdot)_{[i]}$ extracts the temporal spline vector of size $\mathbb{R}^S$ at voxel i given a vector in $\mathbb{R}^{NS}$. Since all operations in (3.27) are performed component-wise, the quadratic formula can be used to solve for $c_{[i]}$. Algorithm 3.3 illustrates the proposed iterative MAP scheme employing KDE (MAPKDE).

It is worth noting that in (3.27), we have made a simplification which allows us to solve a quadratic system. Specifically, the terms $G(c_{[i]}^{(k)}, c_{[j]}^{(k)})$ are computed "late", that is, we made the substitution $c_{[i]} \leftarrow c_{[i]}^{(k)}$ in the term $G(c_{[i]}, c_{[j]}^{(k)})$. This type of substitution in the prior probability was first proposed in [33,34], and is known as the "one step late" approach.

Convergence Analysis

A thorough theoretical analysis for the convergence of MAPKDE remains to be carried out, however, our experiments show that MAPKDE appears to converge since the series of iterates $\{c^{(k)}\}$ contracts, that is

$$||c^{(k+1)} - c^{(k)}||_2 \leq ||c^{(k)} - c^{(k-1)}||_2.$$

Figure 3.3 an example of the ℓ_2 difference between consecutive iterates during a reconstruction.

The non-negativity constraint, $c \succeq 0$, of MAPKDE holds for all tested scaling parameters. Upon closer inspection of Line 7 in Algorithm 3.3, it is apparent that the constraint

$$(h_{c,i}^2 (F^\top 1_{MKT})_{[i]} - \mathbf{MSF}(c_{[i]}^{(k)}))^2 \preceq (h_{c,i}^2 (F^\top 1_{MKT})_{[i]} - \mathbf{MSF}(c_{[i]}^{(k)}))^2 + 4 h_{c,i}^2 c_{[i]}^{(k)} \left(F^\top \frac{g}{F c^{(k)}} \right)_{[i]} \quad (3.28)$$

Algorithm 3.3 4D Maximum a Posteriori Image Reconstruction Algorithm Employing Kernel Density Estimators (MAPKDE).

Let $1_{MKT} \in \mathbb{R}^{MKT}$ be a vector of ones.
Set $k \leftarrow 0$.
Perform one or more EM iterations to obtain initial estimate $c^{(k)} \in \mathbb{R}^{NS}$, or set manually.
Set $y_{[i]}^{(k)} \in \mathbb{R}^d$ to be the spatial locations of the temporal spline coefficients $c_{[i]}^{(k)} \in \mathbb{R}^S$.
repeat
  for $i = 1, \ldots, N$ **do**

$$c_{[i]}^{(k+1)} = \frac{1}{2}\Bigg\{ -\left(h_{c,i}^2 \left(F^\top 1_{MKT}\right)_{[i]} - \frac{\sum_{j=1}^N c_{[j]}^{(k)} G(c_{[i]}^{(k)}, c_{[j]}^{(k)}) G(y_{[i]}^{(k)}, y_{[j]}^{(k)})}{\sum_{j=1}^N G(c_{[i]}^{(k)}, c_{[j]}^{(k)}) G(y_{[i]}^{(k)}, y_{[j]}^{(k)})}\right) + \sqrt{\left(h_{c,i}^2 \left(F^\top 1_{MKT}\right)_{[i]} - \frac{\sum_{j=1}^N c_{[j]}^{(k)} G(c_{[i]}^{(k)}, c_{[j]}^{(k)}) G(y_{[i]}^{(k)}, y_{[j]}^{(k)})}{\sum_{j=1}^N G(c_{[i]}^{(k)}, c_{[j]}^{(k)}) G(y_{[i]}^{(k)}, y_{[j]}^{(k)})}\right)^2 + 4h_{c,i}^2 c_{[i]}^{(k)} \left(F^\top \frac{g}{Fc^{(k)}}\right)_{[i]}} \Bigg\}$$

$$y_{[i]}^{(k+1)} = \frac{\sum_{j=1}^N y_{[j]}^{(k)} G(c_{[i]}^{(k)}, c_{[j]}^{(k)}) G(y_{[i]}^{(k)}, y_{[j]}^{(k)})}{\sum_{j=1}^N G(c_{[i]}^{(k)}, c_{[j]}^{(k)}) G(y_{[i]}^{(k)}, y_{[j]}^{(k)})}$$

  end for
  $k \leftarrow k + 1$
until convergence **or** stopping criteria are met

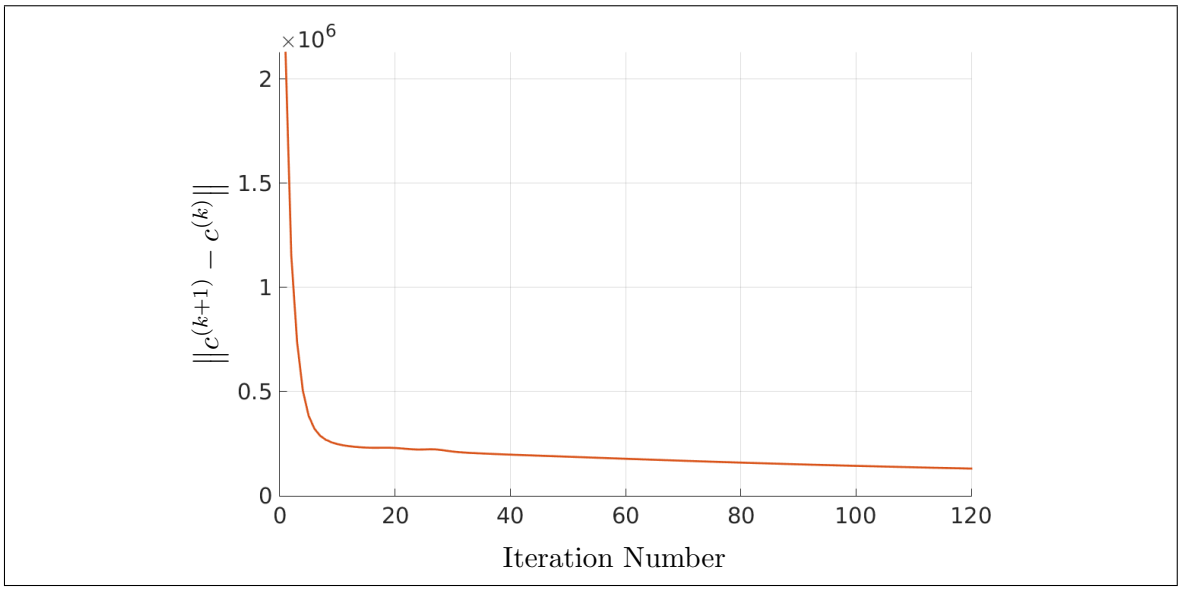

Figure 3.3: *An example of the distance between consecutive iterates as a function of the iteration number measured by the l_2-norm using MAPKDE.*

where

$$\mathbf{MSF}(c_{[i]}^{(k)}) = \frac{\sum_{j=1}^N c_{[j]}^{(k)} G(c_{[i]}^{(k)}, c_{[j]}^{(k)}) G(y_{[i]}^{(k)}, y_{[j]}^{(k)})}{\sum_{j=1}^N G(c_{[i]}^{(k)}, c_{[j]}^{(k)}) G(y_{[i]}^{(k)}, y_{[j]}^{(k)})}$$

is always satisfied since the term

$$4h_{c,i}^2 c_{[i]}^{(k)} \left(F^\top \frac{g}{Fc^{(k)}}\right)_{[i]} \succeq 0 \quad \forall c_{[i]}^{(k)} \succeq 0.$$

We conjecture that the proposed method converges for all scaling parameter values $h_{c,i} > 0$. Let us assume for simplicity (but without loss of generality) that $h_{c,i} = h_c$. Then for very small values h_c the iterative step in Line 7 of Algorithm 3.3 will be dominated by the term, $\mathbf{MSF}(c_{[i]}^{(k)})$, which in fact is a single step of the mean-shift algorithm. Since the positivity constraint cannot be broken, as shown above, then the values $c^{(k)}$ will strongly tend toward $\mathbf{MSF}(c_{[i]}^{(k)})$. In fact, if $h_c = 0$, then Algorithm 3.3 reduces in principle to Algorithm 3.1, which again is a robust algorithm for image denoising and is shown to always converge [16]. Setting $h_c = 0$ is, of course, not possible since the function **MSF** itself does not admit this value for the scaling parameters.

On the other hand, if one picks a very large h_c then the term $\mathbf{MSF}(c_{[i]}^{(k)})$ is comparatively insignificant and the iteration shown in Line 7 of Algorithm 3.3 effectively becomes

$$c^{(k+1)} = \frac{1}{2}\left(-h_c^2 F^\top \vec{1}_{MKT} + \sqrt{(h_c^2 F^\top \vec{1}_{MKT})^2 + 4h_c^2 c^{(k)} : F^\top \left(\frac{g}{Fc^{(k)}}\right)}\right) \tag{3.29}$$

which is the solution to

$$\frac{(c^{(k+1)})^2}{h_c^2} + c^{(k+1)} : F^\top \vec{1}_{MKT} - c^{(k)} : F^\top \left(\frac{g}{Fc^{(k)}}\right) = 0.$$

Assuming h_c is large enough for the first term to be ignored then the iterations reduce to expectation maximization, or

$$c^{(k+1)} = \frac{c^{(k)}}{F^\top \vec{1}_{MKT}} : F^\top \left(\frac{g}{Fc^{(k)}}\right).$$

Our experiments support the aforementioned mathematical approximations.

Choosing the Scaling Parameters

In the presented work, the scaling parameters were chosen manually and uniformly, that is $h_{y,i} = h_y$ and $h_{c,i} = h_c$ for all $i = 1, \ldots, N$. Whether these parameters can be extracted from the data during the reconstruction will be shown in future work. There is an advantage, however, to using h_y and h_c in MAPKDE instead of the free parameter σ in Gaussian prior (as done for MAPMS). The scaling parameters represent physical quantities, namely the scale of the domain and the scale of the range, while the relationship between the parameter σ and the underlying data is not as straightforward.

In our experiments, the parameter h_y was always chosen to be approximately the isotropic size of the object voxel, while the parameter h_c was chosen based on the expected intensity in the time-activity curve. On the other hand, choosing σ needed more guesswork even when the expected range of the TAFs was known.

In real life experiments the expected activity may not be known, however, it is conceivable that one may be able to infer the expected range of activity based on the number of counts in the projections and the sensitivity of the system.

Practical Aspects and Implementation

It is apparent that Algorithm 3.3 can be very computationally intensive. For instance, if the object is discretized to N voxels with S temporal splines in each voxel then the complexity of our algorithm is $\mathcal{O}((NS)^2)$. In practice, performing all these computations is infeasible and extremely time consuming even for an object with a coarse discretization of 64^3 voxels with 16 temporal splines.

To speed up our algorithm the number of computations was reduced by spatially truncating the kernel. That is, computations were performed only on the set

$$Q_i = \{(y_{[j]}, c_{[j]}) : \left\|y_{[i]} - y_{[j]}\right\|_\infty \leq 3h_{y,i}\} \tag{3.30}$$

thereby reducing the complexity to $\mathcal{O}(NLS^2)$ where L is the average cardinality of the sets Q_i. It is expected that $L \ll N$ since one is expected to choose $h_{y,i}$ to be about the value of the desired spatial resolution (e.g. isotropic voxel size) of the reconstructed object.

While truncation dramatically reduced execution time, it was not sufficient for discretizations above $32^3 \times 16$, therefore the truncated prior was implemented on a GPU using CUDA with very satisfactory results as an object of size $64^3 \times 16$ is computed in approximately 12 seconds.

Our choice of using GPUs to speed up computation was one among many. In literature computational optimization of mean-shift is an active field of research and alternatives to a GPU implementation exist (cf. [71, 76]).

3.4 Experiments on Dynamic Simulated Phantoms

Two phantoms were used to evaluate the quality of the images obtained from the proposed methods, namely, the XCAT heart phantom, and a Jaszczak-like phantom. The XCAT heart phantom was used to observe the effects of the large blood-pool (BP) signal on the comparatively thin abutting left ventricular myocardium (LVM). The Jaszczak-like phantom was used with the intent of observing the effects of mean-shift filtering on the resolution of the reconstructed images. The signal-to-noise ratio (SNR) and bias were used as measures of quality to compare the proposed method to EM, and a MAP method employing a Gibbs prior as described in the following section.

3.4.1 A Short Description of the Gibbs Prior

A Gibbs MAP reconstruction method was used to compare the quality and properties of the proposed MAP methods, namely MAPMS and MAPKDE. The Gibbs prior takes the same form as the prior proposed for MAPMS in (3.11), however, $\mu^{(k)}$ is computed as

$$\mu_{[i]}^{(k)} = \frac{1}{\left|\mathcal{N}_r(c_{[i]}^{(k)})\right|} \sum_{j \in \mathcal{N}_r(c_{[i]}^{(k)})} c_{[i]}^{(k)} - c_{[j]}^{(k)} \tag{3.31}$$

for $i = 1, \ldots, N$, where

$$\mathcal{N}_r(c_{[i]}) = \left\{ j : \left\|c_{[i]} - c_{[j]}\right\|_2 \leq r \right\} \tag{3.32}$$

is the neighbourhood of component $c_{[i]} \in \mathbb{R}^S$ in a ball of radius r, and $\left|\mathcal{N}_r(c_{[i]})\right|$ is the cardinality of the set.

Table 3.1: *Arterial input function parameters chosen to simulate low- and high-count regimes.*

Parameter (unit)	Low-activity XCAT Heart	Low-activity Jaszczak	High-activity XCAT/Jaszczak
a_1	`1.0e4`	`1.0e5`	`1.0e7`
a_2	`1.0e3`	`1.0e4`	`1.0e6`
b_1 (min^{-1})	`6.0e-1`	`6.0e-1`	`6.0e-1`
b_2 (min^{-1})	`6.0e-2`	`6.0e-2`	`6.0e-2`

We compare against this Gibbs prior with the expectation that the proposed methods will yield better sharpness of the images since values are shifted toward the mean of a spatial neighbourhood with similar intensity values (or time-activity curves), while the Gibbs prior computes the mean of the spatial neighbourhood indiscriminately.

3.4.2 Experiment Setting

Geometry of Scanner Each acquisition was performed using 19 fixed detector heads in an attempt to approximate (but not replicate) the GE Discovery NM 530c cardiac SPECT camera:

- 9 detector heads are located in a great circle (equator) equiangularly distributed between 0° and 180°,
- 5 detector heads are located in a great circle tilted 30° from the equator between 0° and 180°,
- 5 detector heads are located in a great circle tilted −30° from the equator between 0° and 180°.

Simulated TAF Parameters A reversible one-tissue model was used to simulate the kinetics of the radioactive tracer in each object voxel. The arterial input function (representing the activity at a point in time) is described by the sum of two exponentials as

$$q_B(t) = a_1 e^{-b_1 t} + a_2 e^{-b_2 t} \tag{3.33}$$

where b_1 and b_2 are washout rates, and a_1 and a_2 indicate activity (in arbitrary units). The parameters were set to simulate low and high activity regimes as shown in Table 3.1.

The time-activity function of the simulated *measured myocardial activity* is modelled as

$$q_m(t) = (1 - \phi_v) q_B(t) * (k_{21} e^{-k_{12} t}) + \phi_v q_B(t) \tag{3.34}$$

where $*$ is the convolution operator, k_{21} and k_{12} represent the forward and reverse kinetic parameters respectively, and ϕ_v represents the fractional blood volume (cf. [75, 80]). The values of the kinetic parameters for each tissue region have been taken from [75] and are listed in Table 3.2. The time-activity functions by region are shown in Figure 3.4.

Table 3.2: *Kinetic parameters used to simulate tissue kinetics: k_1 and k_2 represent the kinetic parameters of a reversible single-compartment model, and ϕ_v is the fractional volume; values taken from [75].*

Region	Kinetic Parameters		Fractional Volume
	k_{21} (min^{-1})	k_{12} (min^{-1})	ϕ_v
LVM	0.590	0.229	0.166
RVM	1.109	0.295	0.606
LAM	0.482	0.236	0.184
RAM	0.760	0.255	0.276

Dynamic Acquisition The simulated projection data was acquired over 720 seconds in 72 time-frames, starting with 5 s acquisitions in the first 180 seconds, followed by 15 s acquisitions.

XCAT Heart Phantom Parameters Focal length 3.75 cm, radius of rotation 15 cm, pinhole radius 0.11 cm, detector discretization 64×64, detector bin size $0.125 \times 0.125\,\text{cm}^2$, object voxel size $0.234^3\,\text{cm}^3$ discretized at 64^3 voxels.

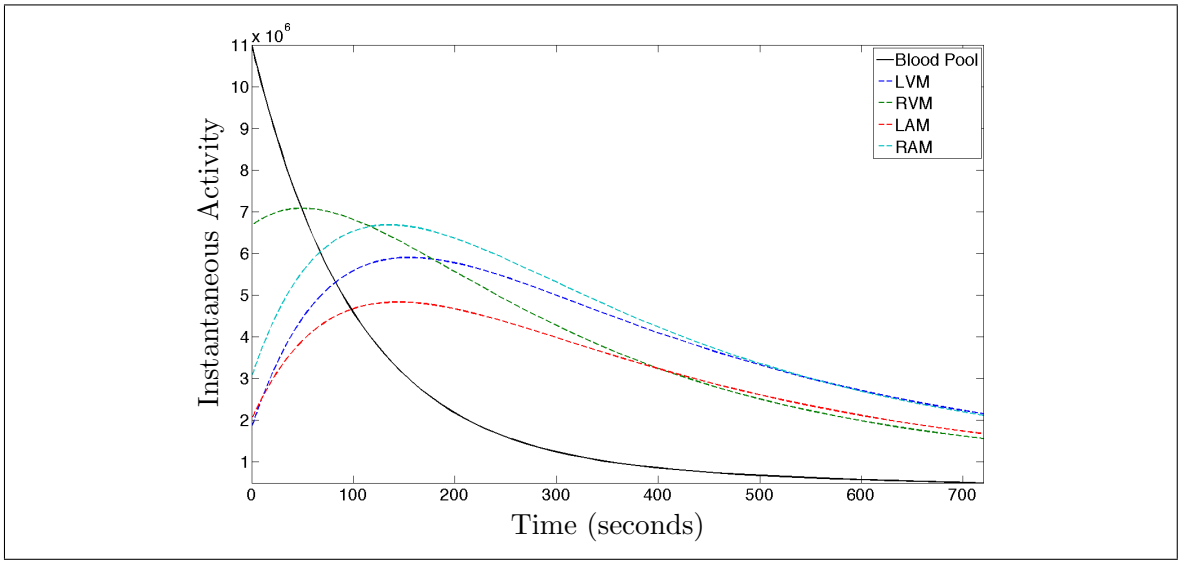

Figure 3.4: *Simulated time-activity functions for different regions in the XCAT heart phantom and the Jaszczak-like phantom. The simulated tissue activities are not representative of an actual physiological process.*

Jaszczak Phantom Parameters Focal length 8 cm, radius of rotation 15 cm, pinhole radius 0.06 cm, detector discretization 64×64, detector bin size $0.125 \times 0.125\,\text{cm}^2$, object voxel size $0.442^3\,\text{cm}^3$ discretized at 64^3 voxels. The time-activity curves simulated in the Jaszczak-like phantom match the regions Blood Pool, LVM (left ventricular myocardium),

RVM (right ventricular myocardium), LAM (left atrial myocardium), and RAM (right atrial myocardium) starting in the sector at 7 o'clock in Figure 3.5 and moving clockwise.

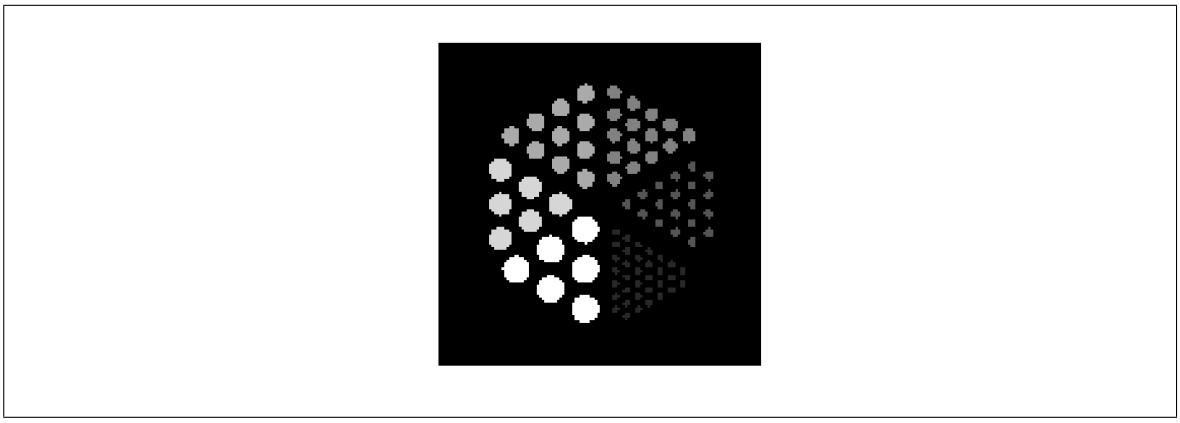

Figure 3.5: *A cross-sectional slice of the simulated Jaszczak-like phantom. The black background is a cold region, while the rods contain activity.*

Object Representation Each voxel in the field of view is represented using 16 geometrically-spaced temporal splines (see Figure 3.6). The spline coefficient representation is used to both "compress" the data to be reconstructed (i.e. reconstruct 16 temporal coefficients as opposed to 72 time-frames), and correlate the time-frames in the object space by the chosen spline basis.

We chose the basis so that it could capture the fastest variations in the TAFs, which happen at the beginning of the acquisition. Since the smallest time-frame of the acquisitions is 5 seconds, we chose the first spline to cover 2.5 seconds, then geometrically spaced 16 splines to cover the entire time of simulated acquisition (720 seconds) as shown in Figure 3.6.

In literature, the number of splines used to represent each voxel is typically much smaller (between 4 and 6 depending on the application), however, we intentionally use large number of splines so as to focus on the effect of the proposed prior rather than the chosen basis. The choice of the temporal spline basis is outside the scope of this research so we refer the reader to [64,65] and the references therein for the complete details on what types of splines can be used and how they are chosen, the effects of noise in the reconstructed coefficients, and artifacts introduced by insufficient sampling.

In addition to compressing the data to be reconstructed, the temporal splines allow us to reconstruct the *instantaneous activity* in the object space, as opposed to the cumulative activity in a time-frame. Specifically, if an acquisition time-frame τ starts at time $t_{s,\tau}$ and ends at $t_{e,\tau}$, then the cumulative activity object $f \in \mathbb{R}^{NT}$ at a voxel $v = 1, \ldots, N$ at frame $\tau = 0, \ldots, T-1$ can be described by a spline basis $\{\eta_s(t)\}_{s=0,\ldots,S-1}$ as shown in Figure 3.6 by

$$\begin{aligned} f_{v+N\tau} &= \sum_{s=0}^{S-1} c_{v+Ns} \int_{t_{s,\tau}}^{t_{e,\tau}} \eta_s(t)dt \\ &= \sum_{s=0}^{S-1} c_{v+Ns}\beta_{s,\tau} \end{aligned} \tag{3.35}$$

where S is the total number of splines, c_{v+Ns} is the spline coefficient of the s-th spline, $\eta_s(t)$, at voxel v and $\beta_{s,\tau} = \int_{t_{s,\tau}}^{t_{e,\tau}} \eta_s(t)dt$. If we organize β as a matrix of $\mathbb{R}^{T\times S}$ and $B = \mathbf{I}_N \otimes \beta$ where $\otimes$ represents the Kronecker product, and $\mathbf{I}_N$ is a $N \times N$ identity matrix then

$$f = Bc \tag{3.36}$$

where $B \in \mathbb{R}^{NT\times NS}$ and $c \in \mathbb{R}^{NS}$. Forward projections can then be obtained from

$$g = Hf = HBc = Fc \tag{3.37}$$

where $H \in \mathbb{R}^{MKT\times NT}$ is the forward projection matrix that models the physical system (scanner), and $F = HB \in \mathbb{R}^{MKT\times NS}$ incorporates both the modelling of the physical system and the temporal spline interpolation.

Reconstruction Parameters The proposed image reconstruction methods were compared against EM, and the MAP method with a Gibbs prior described above. All results shown were obtained after 120 iterations. The number of iterations was deliberately chosen to be relatively large in order to observe the resulting reconstruction "near convergence", and thereby avoiding pragmatic decisions such as terminating the algorithm early in order to obtain "better" reconstructions (as is often done with EM in practice).

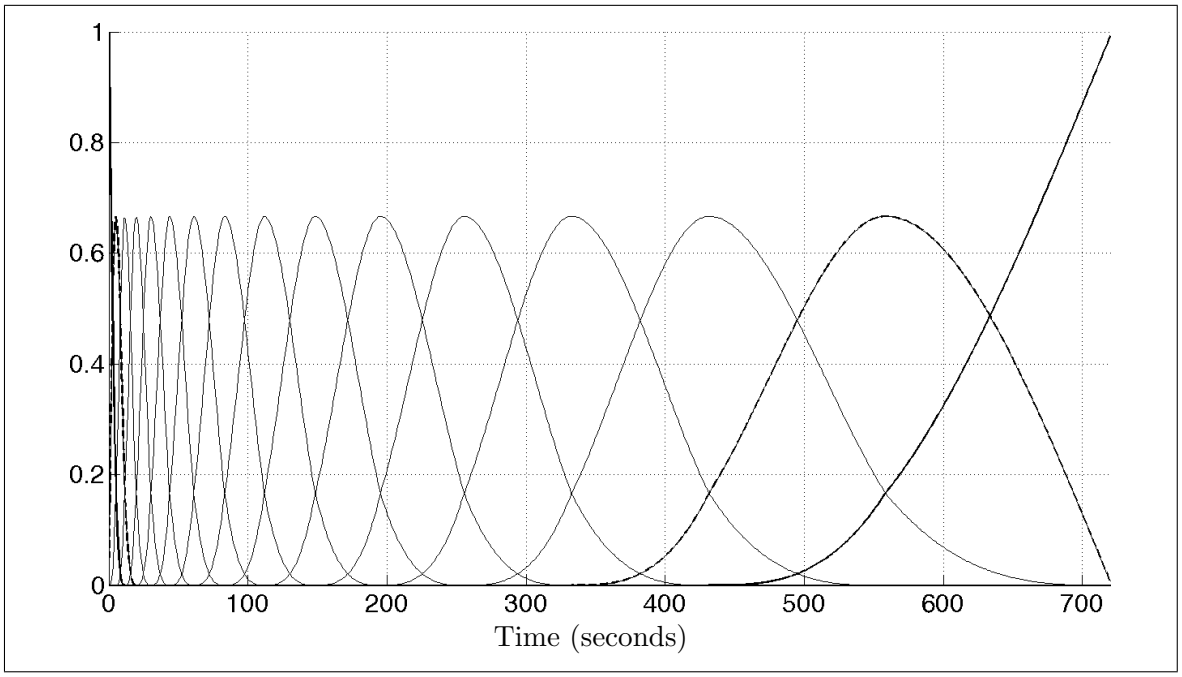

Figure 3.6: *Temporal spline basis used to represent time-activity functions in each object voxel.*

3.4.3 Reconstruction Results and Quality Measures

Coefficient images for both low-count and high-count regimes, averaging 250 counts and 300 K counts per projection respectively, were reconstructed using expectation maximization (EM),

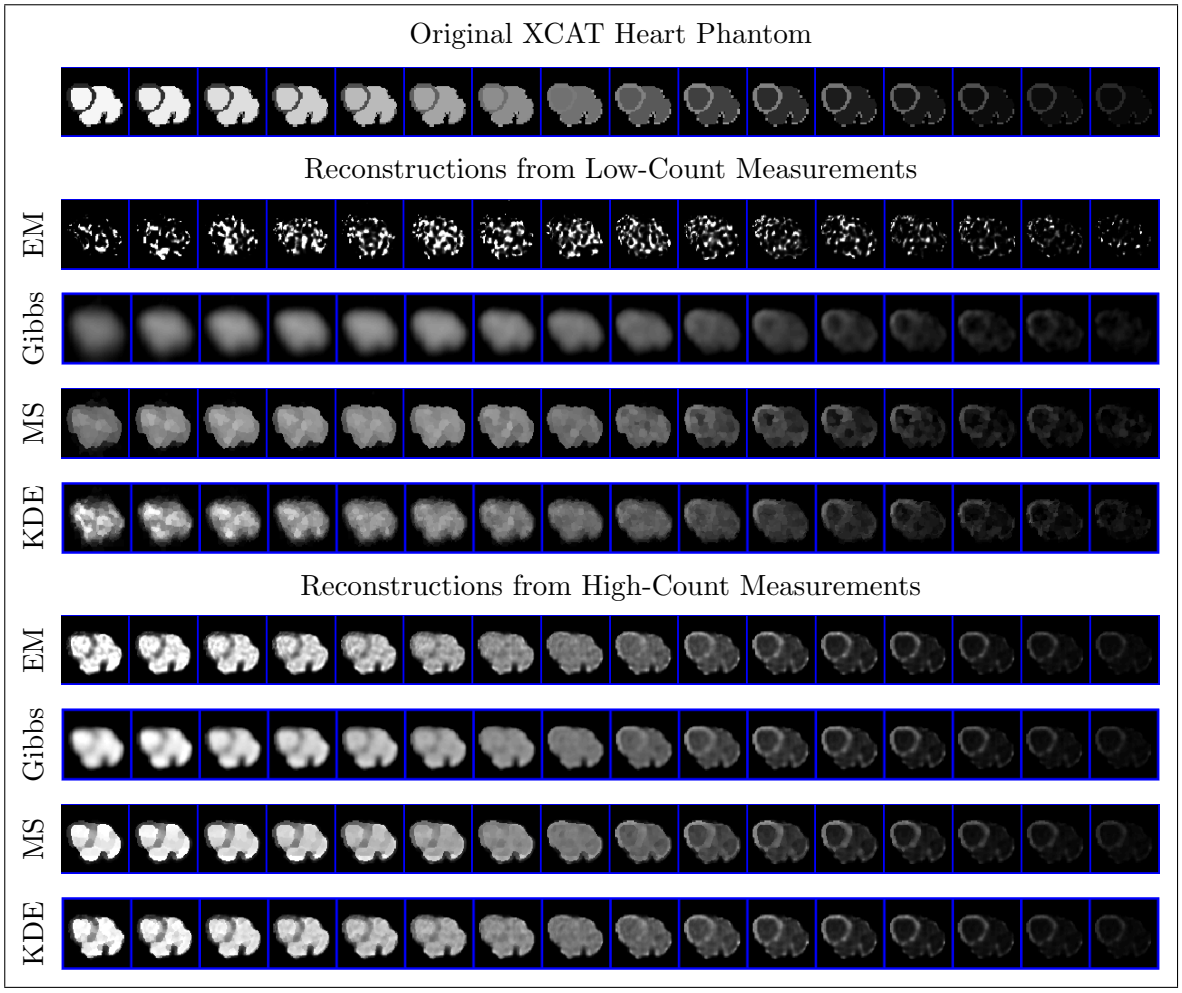

Figure 3.7: *Axial slices of reconstructed temporal spline coefficient images of the XCAT heart phantom at low and high count regimes with MAPMS (labelled MS), MAPKDE (labelled KDE), using a Gibbs prior (labelled Gibbs), and EM.*

MAP employing the aforementioned Gibbs prior, MAPMS, and MAPKDE. Temporal spline coefficient images for reconstructed phantoms are shown in Figures 3.7 and 3.8.

Figures 3.9 and 3.10 show the time-activity functions by voxel in low- and high-activity regimes respectively, where voxels in each regions are grouped by colour (blue for LVM and red for blood pool). The simulated activity for each corresponding region is also shown in the same figures by thick black lines.

Table 3.3 shows the signal to noise ratio (computed only for the Jaszczak phantom) and the bias (for both phantoms) using EM, the aforementioned Gibbs prior, MAPMS, and MAPKDE. The bias is computed using

$$\text{Bias} = \frac{\sum_{i=1}^{NS}(f_i - f_i^*)}{\sum_{i=1}^{NS} f_i} \tag{3.38}$$

where f represents the original phantom (ground truth), and f^* is the reconstructed image. The SNR is computed only for the Jaszczak phantom as the ratio of the mean intensity

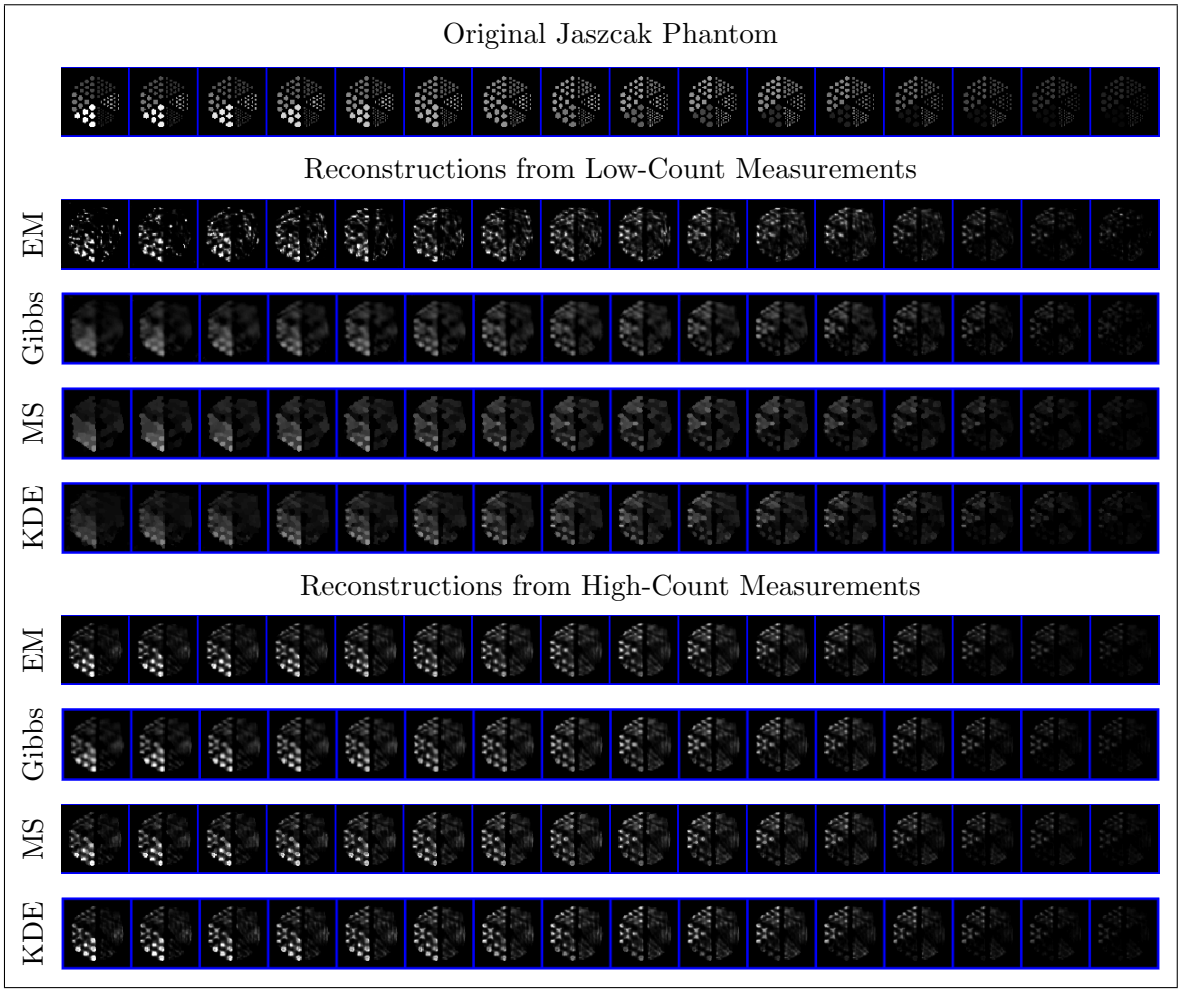

Figure 3.8: *Axial slices of reconstructed temporal spline coefficient images of a Jaszczak-like phantom at low and high count regimes with MAPMS (labelled MS), MAPKDE (labelled KDE), using a Gibbs prior (labelled Gibbs), and EM.*

value of the thickest rods to the variance of the cold region between the rods or "background signal". The SNR cannot be computed for the XCAT heart phantom fairly since the cold region is outside the phantom. For reference, based on (3.38) a positive bias indicates that the total activity in the reconstructed phantom is lower than in the original phantom.

3.5 A Discussion on the Obtained Results and Future Work

The proposed MAP reconstruction methods were designed with the intent of regularizing the behaviour of the time-activity functions (TAFs) over space and time by clustering similar TAFs where the similarity is determined by the scaling parameters. As expected, in high-count regimes it was observed that the proposed methods clusters similar TAFs together, effectively segmenting regions. Figure 3.10 shows high-count reconstructions of the XCAT heart phantom; the TAFs obtained using EM and Gibbs prior are more "spread out" than those obtained using the proposed methods.

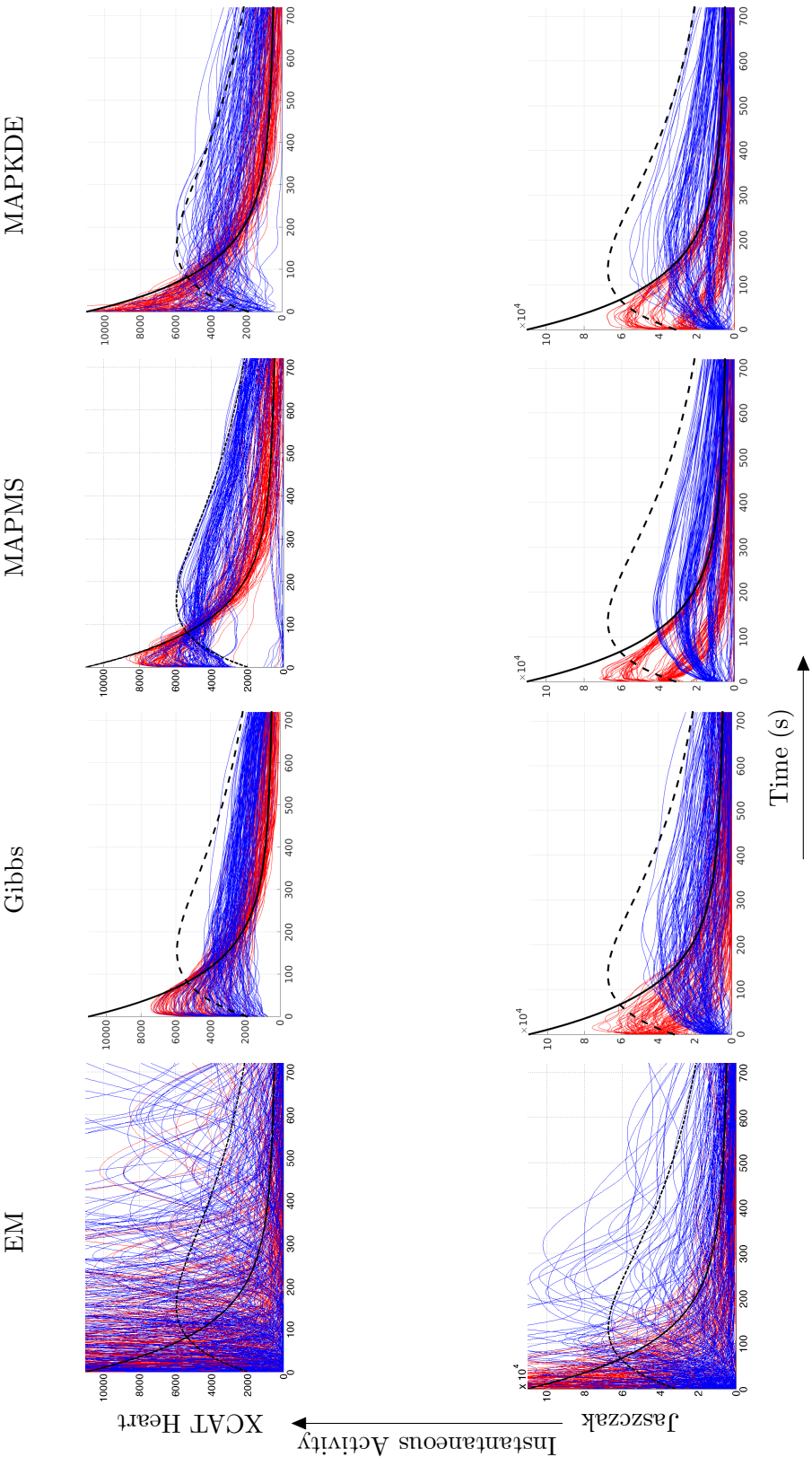

Figure 3.9: *Low-count time-activity functions of the blood pool (red) and left ventricular myocardium (blue) of individual voxels from reconstructed images inside each region are shown, along with simulated curves for the blood pool (thick black) and LVM (thick dashed) for two phantoms. Each column shows the algorithm used to reconstruct the images, and each row shows a phantom.*

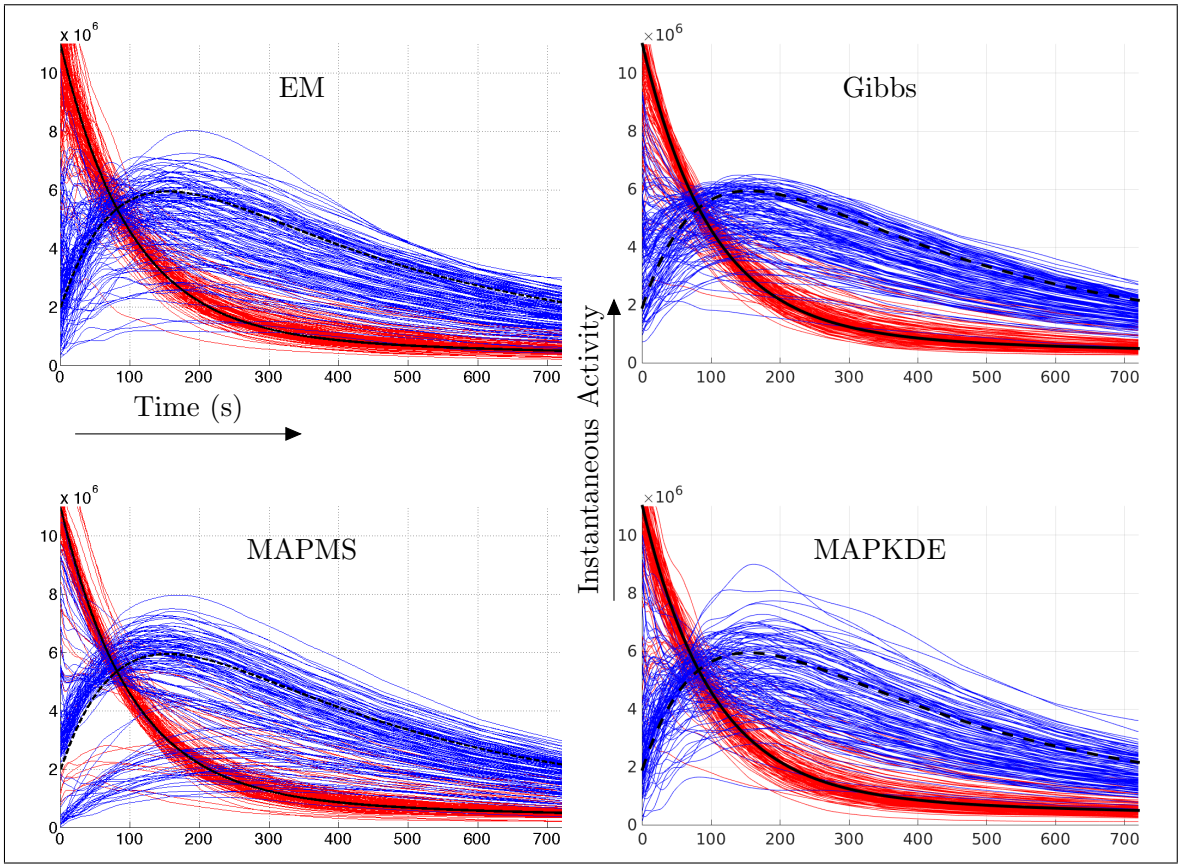

Figure 3.10: *High-count time-activity functions of the blood pool (red) and left ventricular myocardium (blue) of individual voxels from the reconstructed images of the XCAT heart phantom shown over simulated curves for the blood pool (thick black) and LVM (thick dashed). The time-activity functions obtained using the proposed MAP methods (bottom row) are more "tightly bundled" when compared to those obtained using EM (top left) and Gibbs (top right).*

In low-count regimes the proposed method outperforms EM when it comes to preserving image structure and visual salience (see Figures 3.7 and 3.8), with TAFs which better resemble the ground truth (see Figure 3.9). On the other hand, the Gibbs prior is also able to preserve structure and greatly reduce the variation on the TAFs, but it does so while reducing the sharpness across regions with different activity. Finally, TAFs appear more visibly clustered from MAPMS and MAPKDE than the Gibbs prior (see bottom row of Figure 3.9).

Loss of detail is possible with the proposed methods as can be seen from the low-count reconstructions in Figure 3.8. In the case of MAPMS the parameter σ was chosen so that the effect of mean-shift would be predominant. If one chooses a larger σ more detail appears, but with a loss of sharpness and more noise-related variation in the TAFs. The analogy holds for MAPKDE also, based on the range scaling parameter h_c.

As shown in Table 3.3, the proposed method has a comparable bias to EM in low and high count regimes, however, the SNR for low-count regimes is higher for MAPMS and MAPKDE than EM. When comparing against the Gibbs prior, it is apparent that the bias

Table 3.3: *The bias and SNR for reconstructed phantoms using EM and the proposed MAP. Bias and SNR are averaged over the time-frames.*

Regime	Phantom	Method	Avg. SNR	Avg. Bias
Low Count	XCAT Heart	EM	–	1.1856e-02
		Gibbs (σ:2e3)	–	1.3921e-01
		MS (σ:8e2)	–	9.5844e-02
		KDE (h_y:2.34e-1, h_c:8.00e2)	–	6.9849e-02
	Jaszczak	EM	7.9918e-01	1.8578e-01
		Gibbs (σ:2e4)	1.0910e+00	9.4715e-02
		MS (σ:5e3)	1.0785e+00	8.8426e-02
		KDE (h_y:2.34e-1, h_c:4.00e3)	1.0791e+00	1.6472e-01
High Count	XCAT Heart	EM	–	6.1623e-03
		Gibbs (σ:8e5)	–	6.5763e-02
		MS (σ:8e5)	–	7.1924e-02
		KDE (h_y:2.34e-1, h_c:4.00e6)	–	1.7790e-02
	Jaszczak	EM	9.7556e-01	1.8076e-01
		Gibbs (σ:8e5)	9.5975e-01	7.8171e-02
		MS (σ:8e5)	9.1961e-01	8.1756e-02
		KDE (h_y:2.34e-1, h_c:4.00e6)	9.0453e-01	1.3936e-01

and SNR are very similar, but this is because these measures do not capture sharpness.

Finally, it is apparent (especially from the images reconstructed from low-counts) that both MAPMS and MAPKDE exhibit some loss of intensity. We believe there are two main reasons for this.

- The initial guess used in our experiments is always as a flat image of ones, which is of lower intensity than the true image. This means that for the experiments presented we are always approaching the solution from "below", and due to the nature of the proximal algorithm, a new iterate is "attracted" toward the previous iterate which is of lower intensity.
- Due to the regularization that the prior introduces, the activity which would otherwise be "clumped" together (as it happens in the images reconstructed using EM from low-counts) is spread out more uniformly in the original activity region.

Both statements are supported by the positive bias of the reconstructed images (Table 3.3).

Differences Between MAPMS and MAPKDE There are two main differences between MAPMS and MAPKDE in terms of design. While both are proximal algorithms that essentially measure the distance to the previous iterate, MAPKDE effectively measures

the distance after a single mean-shift iteration whereas MAPMS measures the distance to a mean-shift denoised image. That is, in MAPMS the mean-shift algorithm is run until convergence, while in MAPKDE the update is performed simultaneously from both the likelihood and prior terms. (based on the chosen scaling parameters) "holds together" time-activity functions which are close and similar in previous iterations. In either case, this implies that the initial guess should affect the result (i.e. provide a different solution).

The other major difference between MAPMS and MAPKDE is the free (or penalty) parameter σ. In MAPMS, one can change the σ in the Gaussian prior and can therefore control how much the previous mean-shifted iterate $\mu^{(k)}$ can affect the next $c^{(k+1)}$. In fact, one can effectively convert MAPMS to EM by setting $\sigma = 0$. The same cannot be done with MAPKDE, where one can never nullify the effect of the KDE-based prior due to the fact that there is no free parameter.

There is an advantage, however, to using MAPKDE. The free (penalty) parameters have typically no physical meaning and therefore their relationship with the data is not straightforward, while the scaling parameters are more clearly related to the spatial and intensity values to be reconstructed. As explained above, in our experiments the parameter h_y was always chosen to be approximately the isotropic size of the object voxel, while the parameter h_c was chosen based on the expected variation of intensity in the time-activity functions, and, while one may not always know the expected intensity, it is likely that one can estimate it from the sensitivity of the imaging system and the number of counts in the measured projections.

Future Work: Anisotropic Scaling Parameters The design of MAPKDE and MAPMS in this chapter assumes that the scaling parameters $h_{y,i}$ and $h_{c,i}$ are isotropic in time. That is, they may vary by voxel (as the index indicates), but the kernel size used for clustering is the same for all spline coefficients, $c_{[i]} = (c_i, c_{i+N}, \ldots, c_{i+(S-1)N})^\top$ in a voxel. While the spatial scaling parameter may not need to vary over time, the consequences of an isotropic range scaling parameter are much more apparent. For instance in Figure 3.10, the time-activity functions are more clustered at the highest intensities (at the beginning of the acquisition), while at lower intensities (toward the end of the acquisition) less clustering is visible. We believe that this phenomenon is due to the isotropic scaling parameter, because the chosen h_c were targeted toward the variation of the highest intensities thereby making the kernel too wide for the lower intensities at later times.

Summary

This chapter has presented two iterative methods of dynamic image reconstruction, namely, MAPMS and MAPKDE. While there are a number of alternatives to solving problems (3.9) and (3.24), the iterative schemes shown in Algorithms 3.2 and 3.3 were chosen to avoid (costly) line-searches, as one needs to perform projections on failed line-searches, or the addition of other parameters related to the solver itself. Of course, alternatives exist to the proposed solvers that may show faster convergence (cf. [9,20]). The convergence properties of the proposed algorithms are a subject for future study.

Chapter 4

On Sampling in Fan Beam Tomography with a Linear Detector as a Perturbation of an Equiangular Scheme

An integral part of the imaging chain is constructing a data acquisition scheme which not only meets sampling conditions (i.e. the data is sufficiently sampled), but does so in an efficient way such that the cost and time of sampling is minimized. Because our research revolves around myocardial imaging with multiple single-pinhole detector heads, we explore the sampling conditions for a flat-detector single-pinhole transform in 2D. We assume that there is no truncation and no noise in the measured projections.

We propose finding an efficient sampling scheme for the flat-detector single-pinhole transform (aka. linear fan-beam) by analyzing the asymptotic properties of the standard fan-beam transform and using the efficient sampling scheme of the latter to approximate the first. Specifically, we find conditions for which the approximation becomes exact, so that the same reconstruction scheme can be used for both.

We explore two main approaches of finding equivalence criteria between the fan-beam and single-pinhole transforms, namely, the coarse grid approach which uses unions of coarse sampling lattices to approximate irregular sampling lattices, and the non-uniform sampling approach that provides bounds which are indicative of the equivalence between a perturbed and a uniform sampling lattice.

4.1 Introduction to Sampling in Tomography

When using a single pinhole collimator in tomography, a sampling scheme is defined by a number of parameters including the radius of rotation, focal length, detector resolution, and number of detector heads. The number of parameters quickly increases if the physical system has multiple detector heads that do not lie in a great circle (i.e. there is not a single radius of rotation) with each detector head having a different resolution.

In the research presented here the parameters are narrowed down to the "classical" configurations where we consider only the radius of rotation, detector resolution (all detectors have the same resolution), and number of angular sampling points (detector heads lie in a great circle). Since we aim to find conditions for which the flat-detector single-pinhole transform, is equivalent to the angular fan-beam transform, an explanation of these integral transforms is in order.

4.1.1 The Angular Fan-beam and Flat-detector Single-pinhole Integral Transforms

Let an object to be reconstructed from measured projections be denoted by $f : \mathbb{R}^2 \to \mathbb{R}$. Furthermore, let an X-ray source be denoted by $\vec{v}$, then the measurements can be described

by

$$(\mathcal{P}f)(\vec{v},\vec{\zeta}) = \int_{-\infty}^{\infty} f(\vec{v}+\ell\vec{\zeta})d\ell \tag{4.1}$$

where $\vec{\zeta}$ is the unit direction of the integral line.

In the case of the angular fan-beam transform equation (4.1) becomes

$$(\mathcal{D}f)(\beta,\alpha) = \int_{-\infty}^{\infty} f(\vec{v}(\beta)+\ell\vec{\zeta}(\beta,\alpha))d\ell \tag{4.2}$$

where

$$\begin{aligned} \vec{v}(\beta) &= (r\cos\beta, r\sin\beta)^\top \\ \vec{\zeta}(\beta,\alpha) &= (-\sin(\beta+\alpha+\pi/2), \cos(\beta+\alpha+\pi/2))^\top \end{aligned} \tag{4.3}$$

where β is the projection position, α is the incidence angle of the integral line, and r is the radius of rotation as shown in Figure 4.1. Since the object has finite support with radius $\rho = 1$ then the incidence angle $\alpha \in [-\alpha_M, \alpha_M]$ where $\alpha_M = \arcsin(1/r)$.

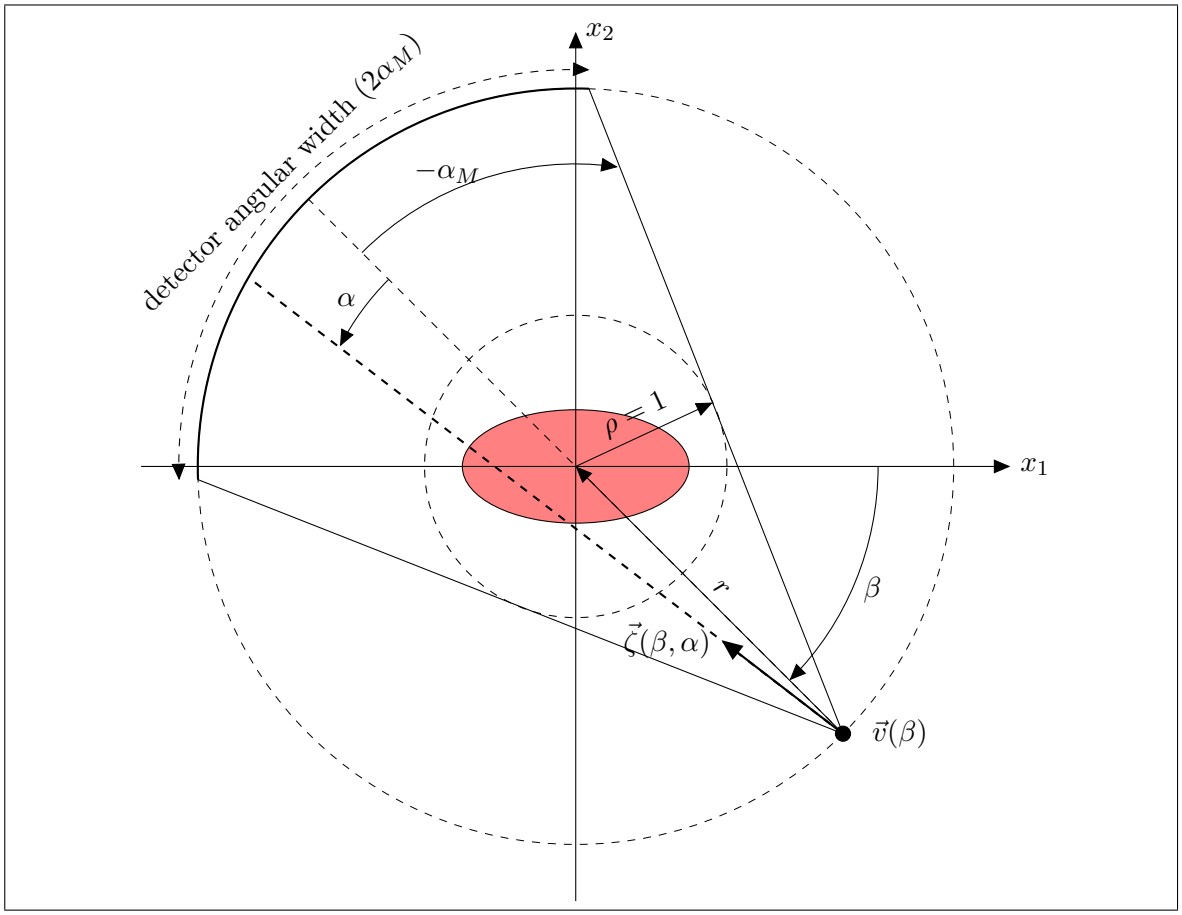

Figure 4.1: *Schematic view of the fan-beam transform: the object being imaged has support of radius $\rho = 1$, the angle β defines the location of the x-ray source $\vec{v}(\beta)$ with radius of rotation r, the detector has angular support α_M, and α defines the direction $\vec{\zeta}(\alpha)$ of the integral line.*

In a similar fashion, the flat-detector pinhole transform (aka. linear fan-beam) can be described by

$$(\mathcal{T}f)(\beta, s) = \int_{\infty}^{\infty} f(\vec{v}(\beta) + \ell\vec{\zeta}(\beta, s))d\ell \tag{4.4}$$

where

$$\begin{aligned} \vec{v}(\beta) &= (r\cos\beta, r\sin\beta)^{\top} \\ \vec{\zeta}(\beta, s) &= (-\sin(\beta + \arctan(s/r) + \pi/2), \cos(\beta + \arctan(s/r) + \pi/2))^{\top} \end{aligned} \tag{4.5}$$

where $s \in [-s_M, s_M]$ is the incidence point of the integral line on the virtual detector surface and $s_M \geq r\tan(\arcsin(1/r))$. A schematic view of this transform is shown in Figure 4.2.

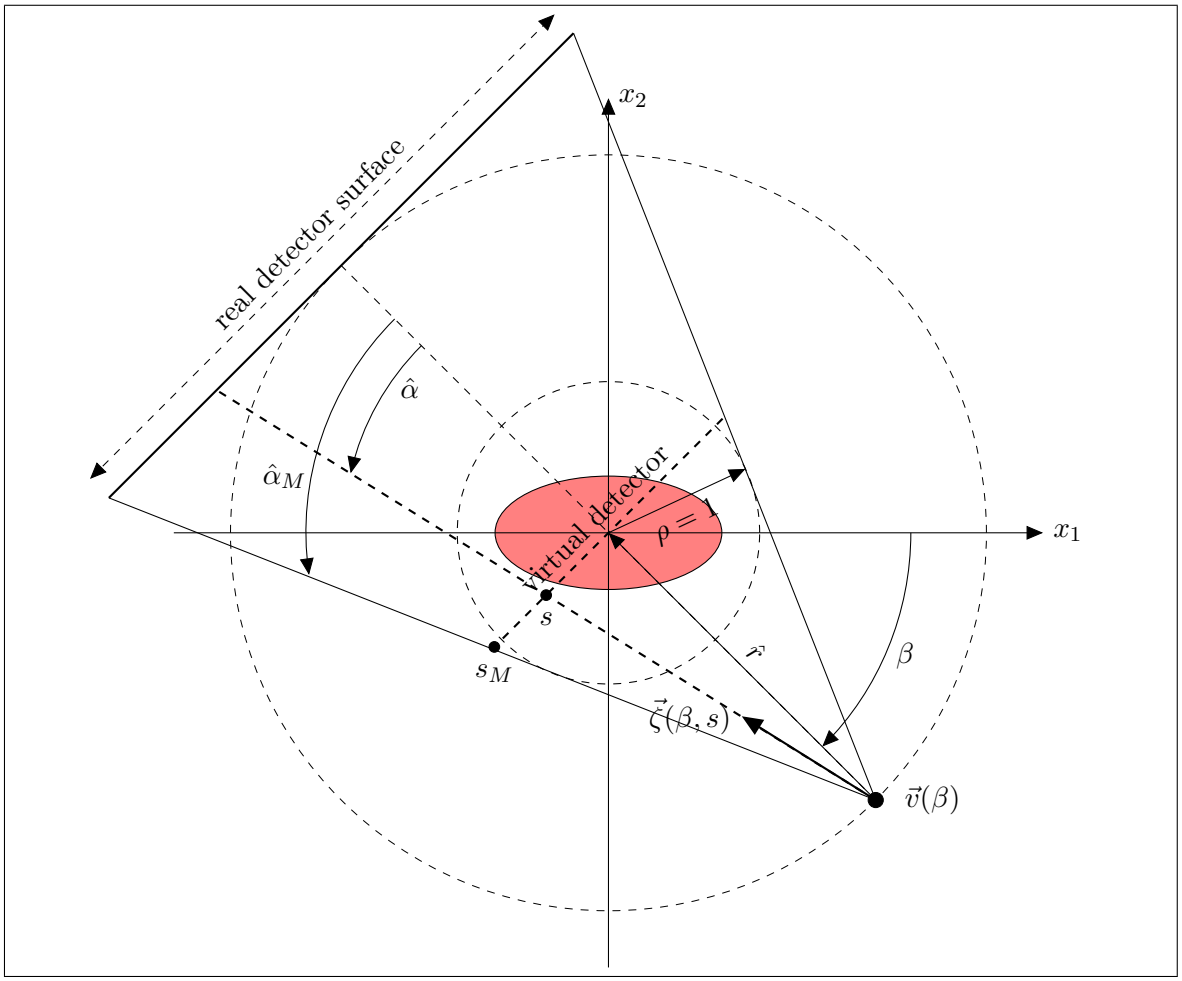

Figure 4.2: *Schematic view of the flat-detector single-pinhole transform: the object being imaged has support of radius $\rho = 1$, the angle β defines the location of the x-ray source $\vec{v}(\beta)$ with radius of rotation $\hat{r}$, the virtual detector has support s_M , and s is the point of incidence of the integral line on the virtual detector surface. The angles $\hat{\alpha}$ and $\hat{\alpha}_M$ are the fan-beam equivalent angles of s and s_M respectively.*

The reader will notice that the transform shown in Figure 4.2 is not immediately representative of the single-pinhole transform, however, it is equivalent to it. Without loss

of generality, we make use of a virtual detector to reduce the number of variables that we must optimize.

While the transforms in equations (4.2) and (4.4) are only different parametrizations of one another in a continuous framework, in a discrete framework the two differ greatly since the first admits sampling points which are equiangular, while the latter admits points which are equidistant (and are therefore non-linear in angular space).

The theory we want to develop relies on the assumption that the object being imaged (i.e. the function to be sampled) has both finite support and is bandlimited, therefore, in the next section we provide the background theory for sampling bandlimited functions in one and many dimensions.

4.1.2 Sampling of Essentially Bandlimited Functions

Given an integral transform, we would like to know how to sample a bandlimited (or essentially bandlimited) function f in order to recover it from projective measurements. Specifically, we would like to know the the radius of rotation, number of projections, and detector resolution when given the *essential bandwidth* Ω of the function f and its support. For simplicity we assume that $f(x) = 0$ for $\|x\|_2 > 1$.

Definition 4.1.1. A function f is essentially bandlimited with bandlimit Ω if the Fourier transform $\hat{f}$ of this function has the property that $\hat{f}(\xi) = 0$ for $|\xi| > \Omega$.

In one dimension, an Ω-bandlimited function f can be reconstructed exactly from its samples if the sampling scheme abides by the conditions set in the Whittaker-Shannon-Kotel'nikov (WSK) sampling theorem.

Theorem 4.1.1 (WSK Sampling Theorem [10])**.** *Every signal function $f(x)$ defined on $\mathbb{R}$ that is bandlimited to an interval $[-\Omega, \Omega]$ for some $\Omega > 0$, can be completely reconstructed for $x \in \mathbb{R}$ from its sampled values $f(k\pi/\Omega)$, taken at the nodal points $k\pi/\Omega$, $k \in \mathbb{Z}$, equally spaced apart on the real axis $\mathbb{R}$, in terms of*

$$f(x) = \sum_{k=-\infty}^{\infty} f\left(\frac{k\pi}{\Omega}\right) \frac{\sin(\Omega t - k\pi)}{\Omega t - k\pi} = \sin(\Omega t) \sum_{k=-\infty}^{\infty} f\left(\frac{k\pi}{\Omega}\right) \frac{(-1)^k}{\Omega t - k\pi}.$$

Example 4.1.1 (Sampling a Bandlimited Function in 1D)**.** Let a function $f : \mathbb{R} \to \mathbb{R}$ be Ω-bandlimited such that $\hat{f}(\xi) = 0$ for $|\xi| > \Omega$, where $\xi \in \mathbb{R}$. Since the Fourier transform of this function is compactly supported in the segment $[-\Omega, \Omega]$, then according to the WSK theorem the signal can be exactly recovered if it is sampled at the points $x = \pi n/\Omega$, for $n \in \mathbb{Z}$ as shown in Figure 4.3.

Theorem 4.1.1 is generalized and extended to bandlimited functions in multiple dimensions by the Petersen-Middleton sampling theorem [63].

Theorem 4.1.2 (Petersen-Middleton Sampling Theorem)**.** *A function $f(\mathbf{x})$ in $\mathbb{R}^n$, whose Fourier transform $\hat{f}(\xi)$ vanishes over all but a finite portion of the wave-number space, can be everywhere reproduced from its sample values taken over a lattice of points defined by $\{l_1\mathbf{v}_1, l_2\mathbf{v}_2, \ldots, l_n\mathbf{v}_n\}$, $l_i = 0, \pm 1, \pm 2, \ldots$, $i = 1, \ldots, n$, provided that the vectors $\mathbf{v}_i$ are small enough to ensure non-overlapping of the spectrum $\hat{f}(\xi)$ with its images on a periodic lattice defined by the vectors $\{\mathbf{u}_k\}$, with $\langle \mathbf{v}_i, \mathbf{u}_k \rangle = 2\pi\delta_{ik}$.*

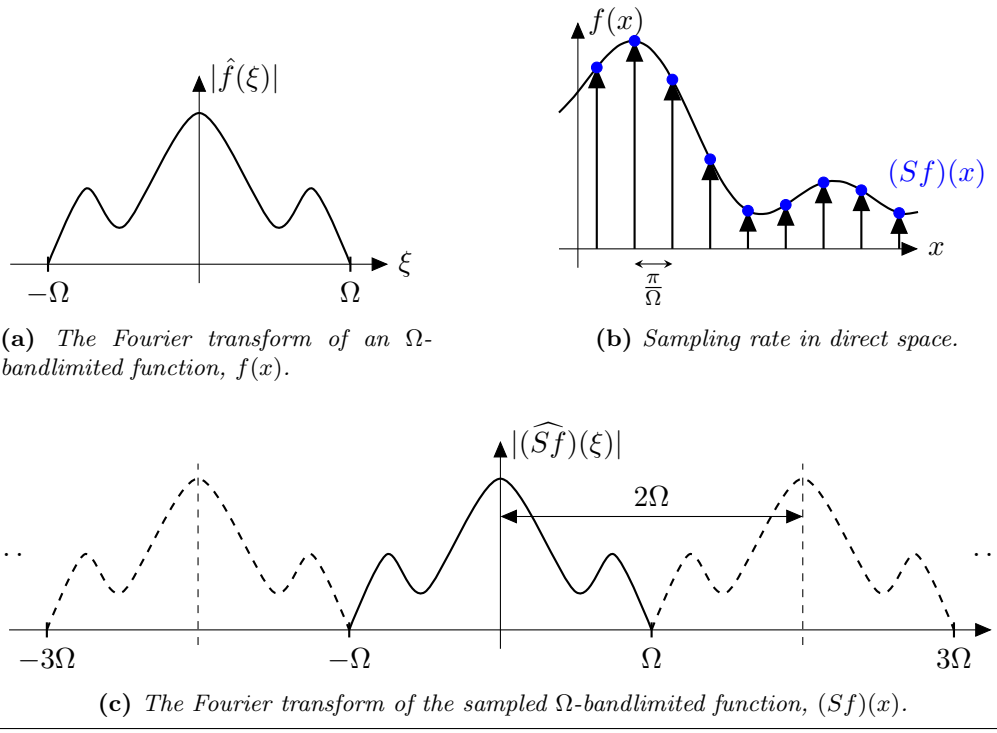

(a) *The Fourier transform of an Ω-bandlimited function, $f(x)$.*

(b) *Sampling rate in direct space.*

(c) *The Fourier transform of the sampled Ω-bandlimited function, $(Sf)(x)$.*

Figure 4.3: *Example of a 1D Ω-bandlimited function sampled at the Nyquist rate.*

Example 4.1.2 (Sampling a Bandlimited Function in 2D)**.** Let a function $f : \mathbb{R}^2 \to \mathbb{R}$ be Ω-bandlimited such that $\hat{f}(\xi) = 0$ for $||\xi||_2 > \Omega$, where $\xi \in \mathbb{R}^2$. The support of the function f in Fourier space is shown in Figure 4.4a. Since the Fourier transform of this function is compactly supported in a ball of radius Ω, then according to the Petersen-Middleton theorem [63] the signal can be exactly reconstructed from sampling schemes which admit no overlapping of their Fourier support sets (i.e. there is no aliasing). One such sampling scheme, known as the standard sampling scheme, is shown in Figure 4.4.

4.1.3 Sampling in Fan-beam Tomography

Theorem 4.1.2 can be extended to fan-beam tomography by analyzing the properties of the integral transform of interest in Fourier space. Let an essentially Ω-bandlimited function $f(x)$ in $\mathbb{R}^2$ with $\text{supp}(f) = \{x \in \mathbb{R}^2 | \quad ||x||_2 \leq 1\}$ be projected according to the fan-beam geometry as shown in Figure 4.1, then the support of the sinogram, $(\mathcal{D}f)$, of such a function in Fourier space also has essentially finite support and takes the form [54, 55, 58]

$$K = \{(k, m) \in \mathbb{Z}^2 \mid |k - m| < \Omega r, \quad |k|r < |k - m|\} \tag{4.6}$$

shown in Figure 4.5a. Here, k and m are the corresponding variables of β and α in Fourier space.

Now, let us introduce the idea of a sampling lattice, and how it is used to represent the sampling of bandlimited or periodic functions.

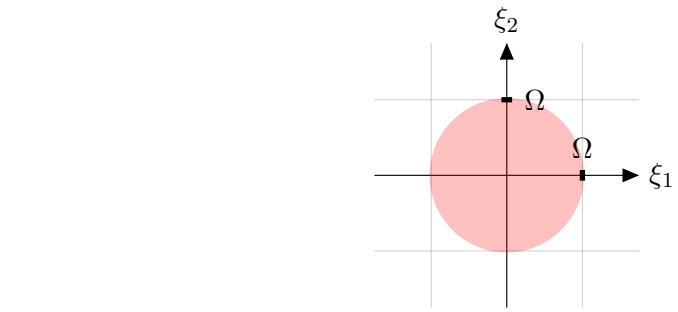

(a) *The support set of Fourier transform of an Ω-bandlimited function, $f(x)$.*

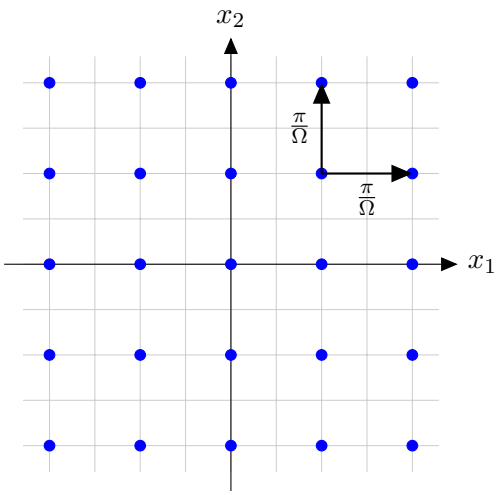

(b) *A sampling of the function f in $\mathbb{R}^2$.*

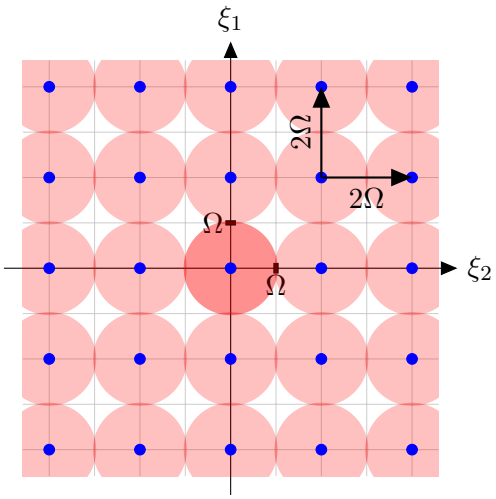

(c) *The support of the Fourier transform of the sampled function, $(Sf)(x)$, at regular intervals along each direction.*

Figure 4.4: *Example of a 2D function whose Fourier transform is compactly supported in a ball of radius Ω.*

Definition 4.1.2. Let a lattice of points in $\mathbb{R}^n$ be denoted by L_W, and let a non-singular matrix $W = [\mathbf{v}_1, \ldots, \mathbf{v}_n]$ where $\mathbf{v}_i \in \mathbb{R}^n$, then

$$L_W = W\mathbb{Z}^n.$$

The angular fan-beam integral transform, $(\mathcal{D}f)$, is periodic in both the rotation angle β and the incidence angle α with period 2π and π respectively (see Figure 4.1), then this function is P-periodic with period

$$P = \begin{bmatrix} 2\pi & 0 \\ 0 & \pi \end{bmatrix}. \tag{4.7}$$

To sample a P-periodic function with a sampling lattice L_W, one must assume that $L_P \subseteq L_W$, which is the case only if $P = WM$, with M as an integer matrix.

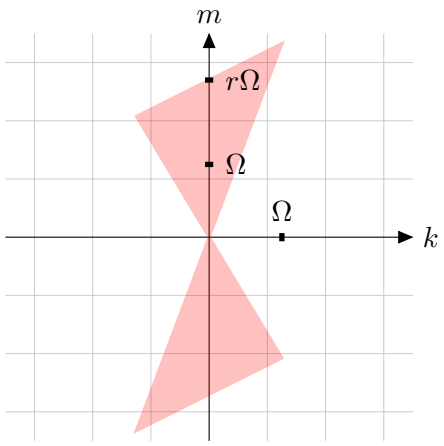

(a) *Essential support set K of the fan-beam transform of an Ω-bandlimited function f with support radius $\rho = 1$. The coordinates k and m correspond to the projection angle β and line-integral incidence angle α respectively.*

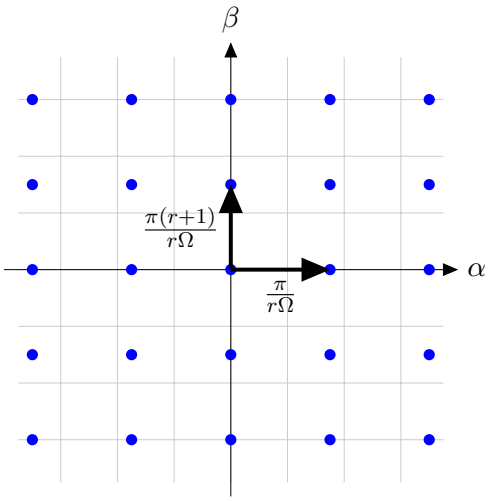

(b) *An efficient standard sampling scheme in direct space.*

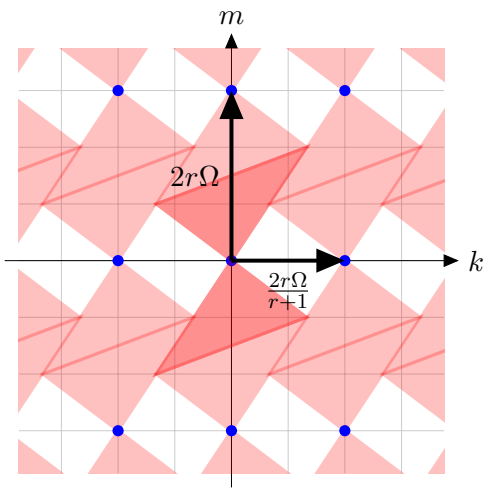

(c) *The tiling of the essential set K in Fourier space when using an efficient standard sampling scheme.*

Figure 4.5: *Essential support set K of the fan-beam transform of an Ω-bandlimited function f with support radius $\rho = 1$ and its efficient standard fan-beam sampling scheme.*

Example 4.1.3 (Sampling a Periodic Function in One Dimension [55])**.** Let $p_1 = 2\pi$ such that $P = [p_1] = 2\pi$, then a suitable sampling lattice is L_W generated by $W = 2\pi/M$, where $M > 0$ in $\mathbb{Z}$, and therefore $P = WM$. The sampling points become apparent in the canonical quotient set $L_W/L_P = \{0, \frac{2\pi}{M}, \ldots, \frac{2\pi}{M}(M-1)\}$.

Let us now define the reciprocal lattice of a lattice L_W, which is its representation in Fourier space, and provide the details of sampling in fan-beam tomography.

Definition 4.1.3. The reciprocal lattice, $L_W^{\perp}$ of a lattice $L_W = W\mathbb{Z}^n$ is $L_W^{\perp} = 2\pi W^{-\top}\mathbb{Z}^n$.

Theorem 4.1.3 (Sampling in Fan-beam Tomography [26,53])**.** *Let $g(\mathbf{z}) = (\mathcal{D}f)(\beta,\alpha)$, such that $g \in C^{\infty}([0,2\pi)\times[-\pi,\pi))$, L_W a sampling lattice, and K be a finite subset of $\mathbb{Z}^2$ such that its translates $K+\xi$, $\xi \in L_W^{\perp}$, are disjoint. Let χ_K denote the indicator function of the essential support set K, with*

$$S_W g(\mathbf{z}) = \frac{(2\pi)^{-1}}{PQ} \sum_{\mathbf{y}\in L_W} \tilde{\chi}_K(\mathbf{z}-\mathbf{y}) g(\mathbf{y}) \tag{4.8}$$

where

$$\tilde{\chi}_K(x) = \sqrt{\frac{2}{\pi}}\Omega \mathrm{sinc}(\Omega x)$$

and the sinogram has been sampled at P projection angles, each with resolution Q, then

$$|g(\mathbf{z}) - S_W g(\mathbf{z})| \leq 2(2\pi)^{-1} \int_{\mathbb{Z}^2\setminus K} |\hat{g}(\zeta)| d\zeta. \tag{4.9}$$

Theorem 4.1.3 indicates that if $\hat{g}$ vanishes outside of the essential set K (i.e. $\hat{g}(\xi) = 0$ for $\xi \notin K$) then the sinogram can be recovered exactly from its samples on the lattice L_W, or $S_W g = g$.

Let the function $f(x)$ in $\mathbb{R}^2$ be sampled through a fan-beam geometry at angles $\{\beta_i\}_{i=0,\ldots,P-1}$ spaced regularly over a great circle, and let the resolution of the detector be dictated by $\{\alpha_j\}_{j=0,\ldots,Q-1}$ equiangularly spaced points, then the generating matrix for the lattice of sampling angles can be

$$W = \begin{bmatrix} \frac{2\pi}{P} & 0 \\ 0 & \frac{2\pi}{Q} \end{bmatrix}.$$

Based on the essential set K stated in (4.6) and Theorem 4.1.3 an efficient standard sampling scheme can be generated from

$$W = \begin{bmatrix} \frac{\pi}{\Omega}\frac{r+1}{r} & 0 \\ 0 & \frac{\pi}{r\Omega} \end{bmatrix}, \quad W^{\perp} = 2\pi W^{-\top} = \begin{bmatrix} \frac{2r\Omega}{r+1} & 0 \\ 0 & 2r\Omega \end{bmatrix} \tag{4.10}$$

where the sampling lattice L_W yields

$$\begin{aligned} \beta_i &= i\Delta\beta = i\frac{\pi}{r\Omega}, \\ \alpha_j &= j\Delta\alpha = j\frac{\pi}{\Omega}\frac{r+1}{r}. \end{aligned}$$

This means $P \geq 2r\Omega$ and $Q \geq \frac{1}{2}\left(\frac{2r\Omega}{r+1} - 1\right)$. The efficient standard sampling scheme is shown in Figure 4.5.

With these sampling conditions, one may use a reconstruction algorithm to obtain the original object f sampled through a fan-beam geometry (see [55, Algorithm 5.3] for an example).

4.1.4 Summary

This section presented the sampling schemes which, based on the Petersen-Middleton theorem [63], yield exact reconstructions of bandlimited functions from tomographic measurements at regular intervals in the angular fan-beam (AFB) transform context. However, the flat-detector single-pinhole transform (aka. linear fan-beam or LFB) irregularly samples the object space from an angular perspective, and therefore its asymptotic properties in Fourier space are more complex. Specifically, we do not know the essential support set of LFB, therefore we try to find conditions under which LFB is exactly the same as AFB, and therefore their essential support set is the same. Knowing the essential support set allows us to construct an efficient sampling scheme from which the original signal can be recovered exactly.

4.2 Non-uniform Sampling, Unions of Sampling Lattices and Applications to Linear Fan-Beam Tomography

This section provides background on methods of sampling on irregular lattices. There are two main approaches to reconstructing functions which have been irregularly sampled. The first approach, explained in Section 4.2.1, constructs a periodic irregular sampling lattice from the union of multiple regular sampling lattices, while the second approach, explained in Section 4.2.2, treats an irregular sampling lattice as a perturbation of a regular sampling lattice.

4.2.1 Sampling on Unions of Coarse Lattices and Their Application to Linear Fan-beam Tomography

Section 4.1 explained the sampling theory related to the standard (angular) fan-beam transform. In summary, it provides us with an interpolation scheme that exactly recovers the original function from its samples, given the proper sampling conditions that allow the for the shifted versions of the essential sets K in (4.6) not to overlap. In this section, we present another interpolation scheme that allows us to reconstruct the original function from the union of multiple sampling schemes (or lattices) each of which undersamples the signal thereby allowing for translates of K to overlap.

Specifically, let a sampling lattice L_W be too coarse to satisfy the conditions of Theorem 4.1.3, that is, the sets

$$K + 2\pi W^{-\top} k, \quad k \in \mathbb{Z}^n, \tag{4.11}$$

are not mutually disjoint. This means that the set K will be partitioned into L sets where $K = \bigcup_{\ell=1}^{L} K_\ell$. More precisely, if we let

$$M_\xi = L_W^\perp \cap (K - \xi), \quad \text{for} \quad \xi \in K$$

then M_ξ will assume finitely many different values $M_1, \ldots, M_\ell$ as ξ travels through K, and each tile K_ℓ can be described by

$$K_\ell = \{\xi \in K | M_\xi = M_\ell\}.$$

Example 4.2.1. Let a one dimensional function with essential set $K = [-1, 1]$ in $\mathbb{R}$ be sampled from a coarse sampling lattice $L_W^{\perp} = L_{2\pi W^{-\top}} = \mathbb{Z}$ (i.e. $2\pi W^{-\top} = 1$), then we have

$$M_\xi = L_W^{\perp} \cap (K - \xi) = \begin{cases} \{1, 2\} & \xi \in \{-1\} \\ \{0, 1\} & \xi \in (-1, 0) \\ \{-1, 0, 1\} & \xi = \{0\} \\ \{-1, 0\} & \xi \in (0, 1) \\ \{-1, -2\} & \xi = \{1\} \end{cases}$$

The set K is then effectively partitioned into the set $K_1 = (-1, 0)$ and $K_2 = (0, 1)$ (the sets $K_3 = \{-1\}$, $K_4 = \{0\}$, and $K_5 = \{1\}$, are ignored because they have measure zero). This means $L = 2$, and $M_1 = \{0, 1\}$, $M_2 = \{-1, 0\}$. Focusing on the partition K_1, we see that

$$K_1 = \{\xi \in K \mid (L_W^{\perp} \cap (K - \xi)) = M_1\} = (-1, 0).$$

One can nevertheless achieve a correct sampling from L_W by combining $\overline{m}$ copies of the shifted coarse sampling lattices, L_W^{ζ}, $\zeta = 1, \ldots, \overline{m}$, of L_W where

$$L_W^{\zeta} = \{\tau_\zeta + Wk, k \in \mathbb{Z}^n\}. \tag{4.12}$$

Specifically,

$$\forall \ell \in \{1, \ldots, L\}, \exists M_\ell = \{k_{\ell,0}, \ldots, k_{\ell,m_\ell - 1}\} \subset \mathbb{Z}^n, 1 \leq m_\ell < \infty$$

such that

$$\forall \xi \in K_\ell, k \in \mathbb{Z}^n : \left(\xi - 2\pi W^{-\top} k\right) \in K \iff k \in M_\ell \tag{4.13}$$

where m_ℓ is the number of overlappings of set K_ℓ from the sets $K + 2\pi W^{-\top} k$, $k \in \{k_{\ell,0}, \ldots, k_{\ell,m_\ell - 1}\}$. It turns out that the number $\bar{m}$ of lattices required for a correct sampling is $\overline{m} = \max_{\ell=1}^{L} m_\ell$.

The shifts $\tau_\zeta \in \mathbb{R}^n$ are chosen so that $\forall \ell = 1, \ldots, L$ the linear system

$$\sum_{\zeta=0}^{M-1} \beta_\zeta^\ell = 1 \tag{4.14}$$

$$\sum_{\zeta=0}^{M-1} \beta_\zeta^\ell \exp\left(-2\pi \left\langle (W^{-1}\tau_\zeta), k_{\ell,j} \right\rangle_{\mathbb{R}^2}\right) = 0, \quad \text{for} \quad j = 1, \ldots, m_\ell - 1 \tag{4.15}$$

can be solved for the coefficients $\beta_\zeta^\ell \in \mathbb{C}$, $\zeta = 0, \ldots, \bar{m} - 1$. The interpolation formula is then defined by

$$S_W f(x) = \sum_{\zeta=0}^{M-1} \sum_{k \in \mathbb{Z}^n} f(\tau_\zeta + Wk) g_\zeta(x - \tau_\zeta - Wk) \tag{4.16}$$

where

$$g_\zeta(y) = (2\pi)^{-n/2} |\det W| \sum_{\ell=1}^{L} \beta_\zeta^\ell \hat{\chi}_{K_\ell}(-y),$$

and $\hat{\chi}_{K_\ell}(-y)$ is the indicator function of the set K_ℓ in Fourier space.

In [25] this theory was applied to the Radon transform of an essentially bandlimited function, where the coarse lattice is chosen to sample at half the sufficient rate so that each tile would be overlapped twice. It was found that a function can exactly be reconstructed from the union of coarse sampling lattices (i.e. system (4.15) is solvable) as long as shifted lattices do not correspond. This intuitively makes sense since the original signal can only be recovered from the union of undersampled signals that are not exactly the same (i.e. the undersampled signals must complement each other's information). The details of this study are not directly relevant to our research so we refer the reader to [22, 25] and the references therein for more details. For our purposes, it suffices that there is an interpolation formula which we can use "out of the box" to recover a function from the union of coarse sampling lattices.

Let us now construct LFB as a union of coarse AFP as shown in Figure 4.6.

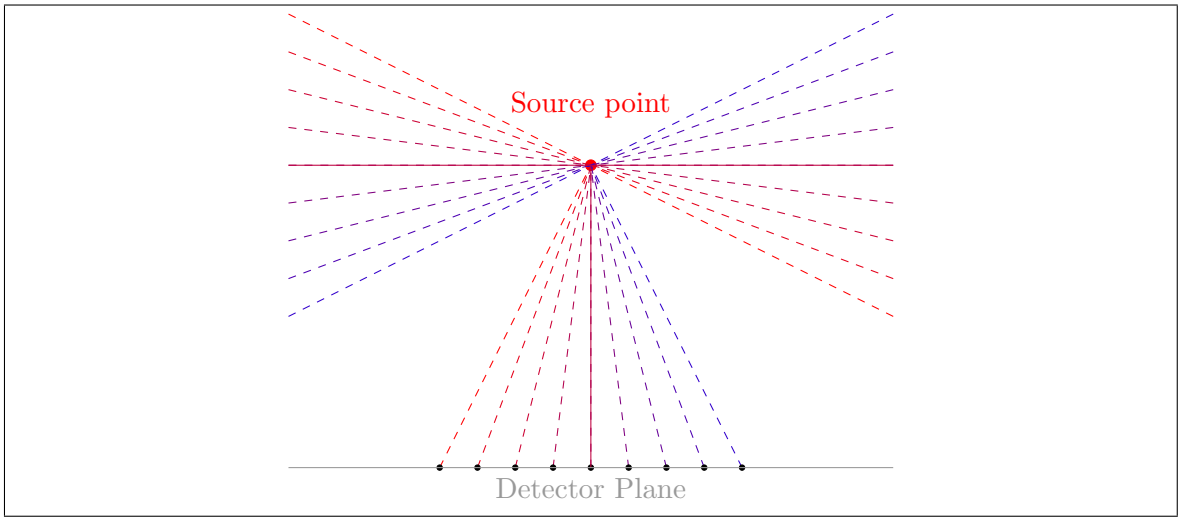

Figure 4.6: *The original integral lines (solid purple) of the coarse angular fan-beam transform are shifted symmetrically from the initial configuration to the points of incidence of linear fan-beam (black dots) on the detector plane. The lines of each of the shifted versions of the coarse angular fan-beam transform correspond by color.*

We know that the standard sampling scheme for the angular fan-beam transform in Fourier space is generated from (4.10), namely

$$W^{\perp} = 2\pi W^{-\top} = \begin{bmatrix} \frac{2r\Omega}{r+1} & 0 \\ 0 & 2r\Omega \end{bmatrix}.$$

To simplify our problem, we oversample the data in the angular direction β (see Figure 4.1) so as to avoid overlaps arising from angular sampling, thereby obtaining the matrix

$$W_S^{\perp} = 2\pi W^{-\top} = \begin{bmatrix} \Omega & 0 \\ 0 & 2r\Omega \end{bmatrix}, \quad W_S = \begin{bmatrix} \frac{2\pi}{\Omega} & 0 \\ 0 & \frac{\pi}{r\Omega} \end{bmatrix}. \tag{4.17}$$

leading to the tiling of the Fourier space shown in Figure 4.7.

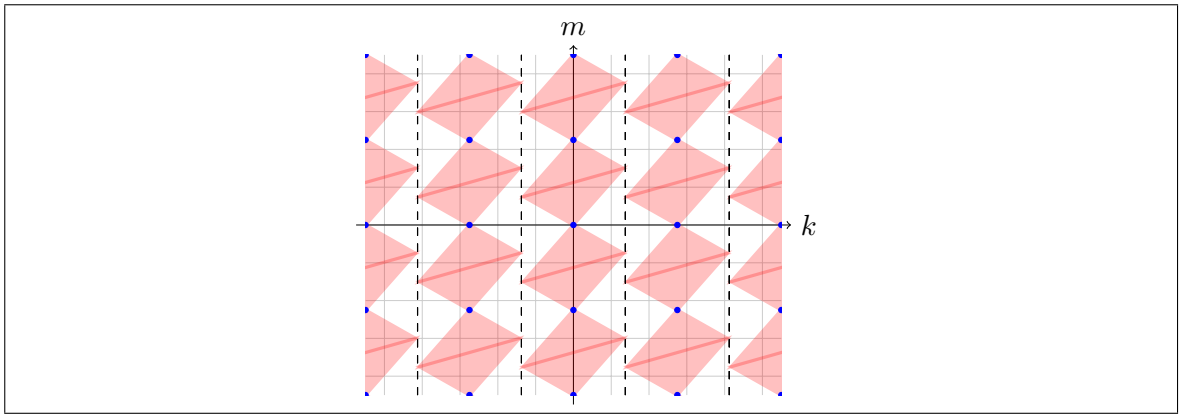

Figure 4.7: *The β-oversampled standard sampling lattice of the angular fan-beam scheme in Fourier space.*

Now we can generate a coarse sampling lattice using

$$W_{CS} = \begin{bmatrix} h_\beta & 0 \\ 0 & (2Q+1)h_\alpha \end{bmatrix} \quad \text{where} \quad h_\beta = \frac{2\pi}{\Omega}, h_\alpha = \frac{\pi}{r\Omega} \tag{4.18}$$

where $2Q+1$ is the number of sampling points in the detector of the linear fan-beam transform. That is, W_{CS} undersamples the signal by a factor of $2Q+1$ in the angle of incidence α. The original lattice is obtained by the union of $2Q+1$ coarse lattices, or conversely, in Fourier space the coarse lattice is obtained as the shifted union of standard lattices, or

$$\begin{aligned} W_{CS}^{-\top}\mathbb{Z}^2 &= \bigcup_{k\in\mathbb{Z}^2} \left(\frac{k_1}{h_\beta}, \frac{k_2}{2Q+1}\frac{1}{h_\alpha}\right) \\ &= \bigcup_{t=-Q}^{Q} \bigcup_{k\in\mathbb{Z}^2} \left(\frac{k_1}{h_\beta}, \frac{k_2}{h_\alpha}\right) + \left(0, \frac{t}{(2Q+1)h_\alpha}\right) \\ &= \bigcup_{t=-Q}^{Q} W_S^{-\top}\mathbb{Z}^2 + \left(0, \frac{t}{(2Q+1)h_\alpha}\right) \\ &= \bigcup_{t=-Q}^{Q} W_S^{-\top}\mathbb{Z}^2 + \left(0, \frac{\tau_t}{2Q+1}\right) \end{aligned}$$

where $\tau_t = \left(0, \frac{t}{h_\alpha}\right)^\top$ is the *shift vector* the generates the shifted lattice as shown in (4.12).

What we would like to find is the following relationship. Given an LFB scheme with a radius of rotation $\hat{r}$ sampled at $2Q+1$ angular points, we want to find the smallest radius of rotation r of the AFB scheme (also sampled at $2Q+1$ points) for which the sampling is equivalent and therefore a reconstruction algorithm that exactly recovers the function from one should do the same for the other.

Assuming that we have $2Q+1$ sampling points on our angular fan-beam detector and that the function has compact support $\rho = 1$, then it follows that we need sample only

the space $\alpha \in [-\alpha_M, \alpha_M]$, $\alpha_M = \arcsin(1/r)$ (see Figure 4.1). In light of this, let us write h_α as a function of the maximum angle α_M as $h_\alpha = \alpha_M/Q$, and therefore

$$W_{CS} = \begin{bmatrix} h_\beta & 0 \\ 0 & \frac{Q}{\alpha_M(2Q+1)} \end{bmatrix}, \tag{4.19}$$

and

$$\tau_t = \left(0, \frac{t}{Q}\alpha_M\right)^\top. \tag{4.20}$$

In order to be able to find equivalence criteria between the linear and angular fan-beam transforms, we need to ensure that the perturbation between the two schemes is small enough and the system of equations in (4.14) is still solvable. For this we use a theorem from [22].

Theorem 4.2.1. *Let $\{u_i\}_{i=1,\dots,N}$ be orthonormal vectors such that $\langle u_i, u_j\rangle = \delta_{ij}$. If $\{v_i\}_{i=1,\dots,N}$ are normal vectors such that*

$$\sum_{i=1}^{N} \langle v_i, u_i\rangle^2 > N - 1$$

then the vectors $\{v_i\}_{i=1,\dots,N}$ are linearly independent.

In the case of the coarse equiangular basis, the vectors in (4.15) become

$$\begin{aligned}
(\omega_{2Q}^n)^t &= \exp\left(-2\pi i \left\langle \begin{bmatrix} h_\beta & 0 \\ 0 & \frac{Q}{\alpha_M(2Q+1)} \end{bmatrix} \begin{pmatrix} 0 \\ \frac{t}{Q}\alpha_M \end{pmatrix}, \begin{pmatrix} k_{1,\ell,n} \\ k_{2,\ell,n} \end{pmatrix} \right\rangle\right) \\
&= \exp\left(-2\pi i \left\langle \begin{bmatrix} h_\beta & 0 \\ 0 & \frac{Q}{\alpha_M(2Q+1)} \end{bmatrix} \begin{pmatrix} 0 \\ \frac{t}{Q}\alpha_M \end{pmatrix}, \begin{pmatrix} k_1 \\ k_2(2Q+1)+n \end{pmatrix} \right\rangle\right) \\
&= \exp\left(-2\pi i \frac{t}{2Q+1}(k_2(2Q+1)+n)\right) \\
&= \exp\left(-2\pi i \frac{tn}{2Q+1}\right)
\end{aligned} \tag{4.21}$$

where $k_{1,\ell,n} = k_1$ since no overlaps are caused from the angular direction, and $k_{2,\ell,n} = k_2(2Q+1)+n$ where the overlaps are indexed by n.

Now we need an expression for the basis of the linear fan-beam transform. The perturbed shift vector, that is, the shift vector that corresponds to the linear fan-beam scheme is

$$\vartheta_t = \begin{pmatrix} 0 \\ \arctan\left(\frac{t}{Q}\tan(\hat{\alpha}_M)\right) \end{pmatrix} \tag{4.22}$$

where $\hat{\alpha}_M$ is the maximum angle of incidence assumed for the linear fan-beam scheme. The

vector basis in this case is

$$\begin{aligned}(\omega_{2Q}^{k_{\ell,n}})_t &= \exp\left(-2\pi i\left\langle\begin{bmatrix} h_\beta & 0 \\ 0 & \frac{Q}{\alpha_M(2Q+1)}\end{bmatrix}\begin{pmatrix} 0 \\ \arctan\left(\frac{t}{Q}\tan(\hat{\alpha}_M)\right)\end{pmatrix}, \begin{pmatrix} k_{1,\ell,n} \\ k_{2,\ell,n}\end{pmatrix}\right\rangle\right) \\ &= \exp\left(-2\pi i\frac{Q}{\alpha_M(2Q+1)}\arctan\left(\frac{t}{Q}\tan\hat{\alpha}_M\right)(k_{2,\ell}(2Q+1)+n)\right) \\ &= \exp\left(-2\pi i\frac{nQ}{\alpha_M(2Q+1)}\arctan\left(\frac{t}{Q}\tan\hat{\alpha}_M\right)\right)\exp\left(-2\pi i\frac{k_{\ell,2}Q}{\alpha_M}\arctan\left(\frac{t}{Q}\tan\hat{\alpha}_M\right)\right),\end{aligned} \tag{4.23}$$

and, the inner product of the two bases, that is, the coarse equiangular basis and the coarse linear basis, is

$$\begin{aligned}\left\langle\omega_{2Q}^{n},\omega_{2Q}^{k_{\ell,n}}\right\rangle = \sum_{t=-Q}^{Q}&\exp\left(-2\pi i\frac{Qk_{\ell,n}}{\alpha_M}\arctan\left(\frac{t}{Q}\tan\hat{\alpha_M}\right)\right) \\ &\times\exp\left(-2\pi i\frac{n}{2Q+1}\left(t-\frac{Q}{\alpha_M}\arctan\left(\frac{t}{Q}\tan\hat{\alpha_M}\right)\right)\right).\end{aligned}$$

Ultimately, we would like to find $\hat{\alpha}_M$ given $\alpha_M = \arcsin(1/r)$ for which the condition

$$\min_{k_{\ell,n}}\frac{\sum_{n=-Q}^{Q}\left|\left\langle\omega_{2Q}^{n},\omega_{2Q}^{k_{\ell,n}}\right\rangle\right|^2}{(2Q+1)^2} > 2Q \tag{4.24}$$

holds.

It is obvious that (4.24) will not hold for all combinations of Q, α_M, and $\hat{\alpha}_M$. We solved

$$\frac{\sum_{n=-Q}^{Q}\left|\left\langle\omega_{2Q}^{n},\omega_{2Q}^{k_{\ell,n}}\right\rangle\right|^2}{(2Q+1)^2} - 2Q = 0.$$

for $k_{\ell,n} = 0$, which is expected to cause the least perturbation to the system[1], in order to get an idea of what is the minimum linear fan-beam radius, $\hat{r} = \sin(\hat{\alpha}_M)^{-1}$, based on the discretization Q that be approximated to an angular fan-beam using this approach. The results are shown in Figure 4.8 and listed in Table 4.1 along with the corresponding angular fan-beam system.

It is apparent from Figure 4.8 that as the number of samples Q increases, the smallest radius of rotation for which this approximation is valid quickly increases. For instance, one must have a radius of rotation of about 11.5 units when imaging an object of radius 1 unit with 201 samples (i.e. $Q = 100$) on the virtual detector surface to still be able to analyze the linear fan-beam system through the properties of angular fan-beam. In some applications a factor of about 11 between the radius of rotation and the support of the subject may not be feasible. This factor becomes even larger as the discretization increases. Let us then explore an alternative (and somewhat simpler) approach to finding this same equivalence.

[1]This was found numerically and was expected due to Proposition 4 in [22].

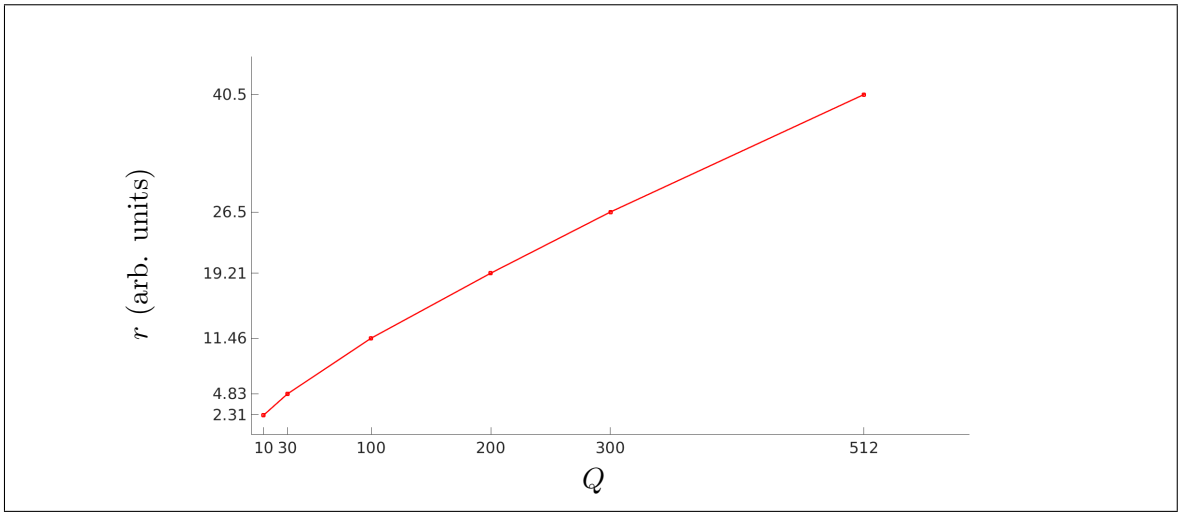

Figure 4.8: *The minimum radius of rotation of the linear fan-beam scheme as a function of the discretization Q for which the coarse sampling lattice approximation is applicable. If a linear fan-beam radius of rotation $\hat{r}$ falls below the line at the given discretization Q, it cannot be approximated by an angular fan-beam system using the proposed method.*

4.2.2 Non-uniform Sampling and Its Possible Application to Fan-beam Tomography

As established earlier in this chapter, the flat-detector single-pinhole transform irregularly samples the object space from an angular perspective (i.e. the samples are not equiangular, though they are equidistant). Non-uniform sampling theory allows us to view equidistant samples as a perturbation of equiangular samples. In this section we present the Paley-Wiener-Levinson theorem which is pertinent to our objective, and explore how it applies to our work.

Given a function $f(t)$ in $\mathbb{R}$ with spectral support $[-\Omega, \Omega]$, and a sampling set $\{t_k\}_{k\in\mathbb{Z}}$ of sampling points where $t_{-k} = -t_k$, we would like to know the interpolation formula that recovers the signal $f(t)$ exactly from its samples $f(t_k)$. This problem was first treated in [48, 59] and the result is summarized in Theorem 4.2.2 below.

Theorem 4.2.2 (Paley-Wiener-Levinson Sampling Theorem)**.** *Let $\{t_k\}_{k\in\mathbb{Z}}$ be a sequence of real numbers such that $t_{-k} = -t_k$ and*

$$D = \sup_{k\in\mathbb{Z}} \left| t_k - k\frac{\pi}{\Omega} \right| < \frac{1}{4}\frac{\pi}{\Omega}, \tag{4.25}$$

and let

$$G(t) = (t - t_0) \prod_{k=1}^{\infty} \left(1 - \frac{t}{t_k}\right)\left(1 - \frac{t}{t_{-k}}\right),$$

then for any Ω-bandlimited function f, we have

$$f(t) = \sum_{k=-\infty}^{\infty} f(t_k) \frac{G(t)}{(t - t_k)G'(t_k)} \quad (t \in \mathbb{R}).$$

Table 4.1: *Linear and angular fan-beam schemes that are equivalent from a union of coarse lattices perspective: r is the radius of rotation of the angular fan-beam scheme, Q is the chosen discretization, h_α is the angular resolution, $\hat{r}$ is the radius of rotation of the linear fan-beam transform, and h_s is the virtual detector resolution. The angular fan-beam configurations correspond to those in Figure 4.8.*

Angular Fan-beam			Linear Fan-beam	
r	Q	Implied h_α ($\times 10^{-3}$)	$\hat{r}$	Implied h_s
2.27	10	45.67	2.31	0.1110
4.80	30	6.98	4.83	0.0341
11.45	100	0.87	11.46	0.0100
19.21	200	0.26	19.21	0.0050
26.50	300	0.13	26.50	0.0033
40.50	512	0.05	40.50	0.0020

For a complete proof see [32].

Theorem 4.2.2 is a generalization of Theorem 4.1.1 since it allows us to reconstruct a function exactly from irregular samples, as long as those samples are within a quarter of the regular sampling distance.

As before, let us sample both the angular and linear fan-beam transforms with $2Q+1$ points, then the respective sampling points are described by

$$\frac{t}{Q}\alpha_M \quad \text{and} \quad \arctan\left(\frac{t}{Q}\tan\hat{\alpha_M}\right),$$

where α_M is the maximum sampling angle in angular fan-beam (see Figure 4.1), $\hat{\alpha}_M$ is the maximum angle in the linear fan-beam (see Figure 4.2), and $t = -Q, \ldots, Q$.

To find the smallest perturbation between the equidistant and equiangular points we pose the optimization problem

$$\min_{\hat{\alpha}_M} \max_{t=-Q,\ldots,Q} \left|\arctan\left(\frac{t}{Q}\tan\hat{\alpha_M}\right) - \frac{t}{Q}\alpha_M\right|. \tag{4.26}$$

Solving (4.26) is not straightforward since to solve for $\hat{\alpha}_M$ one must know the t that maximizes the perturbation, which changes with $\hat{\alpha}_M$. Let us instead make the substitution $t/Q \leftarrow x$ and let $x \in \mathbb{R}$, then we have

$$\min_{\hat{\alpha}_M} \max_{x} \left|\arctan\left(x\tan\hat{\alpha_M}\right) - x\alpha_M\right|.$$

Since the objective function is symmetric around the origin, we can reduce the solution set for x to $\mathbb{R}^+$ thereby modifying the problem to

$$\min_{\hat{\alpha}_M} \max_{x\in\mathbb{R}^+} \arctan\left(x\tan\hat{\alpha_M}\right) - x\alpha_M.$$

From the first-order conditions of

$$\max_{x\in\mathbb{R}^+} \arctan\left(x\tan\hat{\alpha_M}\right) - x\alpha_M$$

we find that

$$x = \sqrt{\frac{\tan\hat{\alpha}_M - \alpha_M}{\alpha_M \tan^2(\hat{\alpha}_M)}}. \tag{4.27}$$

Finally, we make another simplification to our optimization problem in (4.26) by recognizing that the largest perturbations will occur at the edge of the detector ($x = 1$), where $\alpha_M - \hat{\alpha}_M$ is largest, and at a point inside the detector, where

$$\sqrt{\frac{\tan\hat{\alpha}_M - \alpha_M}{\alpha_M \tan^2(\hat{\alpha}_M)}}\alpha_M - \arctan\left(\sqrt{\frac{\tan\hat{\alpha}_M - \alpha_M}{\alpha_M \tan^2(\hat{\alpha}_M)}}\tan\hat{\alpha}_M\right)$$

is largest. In other words, we must solve

$$\frac{\alpha_M}{\tan\hat{\alpha}_M}\sqrt{\frac{\tan\hat{\alpha}_M}{\alpha_M} - 1} - \arctan\left(\sqrt{\frac{\tan\hat{\alpha}_M}{\alpha_M} - 1}\right) = \alpha_M - \hat{\alpha}_M \tag{4.28}$$

to find α_M (or $\hat{\alpha}_M$) given $\hat{\alpha}_M$ (or α_M) which cause the least perturbation. This means that given a linear (or angular) fan-beam scheme, we can find a respective angular (or linear) fan-beam scheme which is closest to it.

For our theory to apply however, we need to also satisfy condition (4.25). That is, the largest variation must also be smaller than a quarter of the discretization of the angular fan-beam scheme, or

$$\alpha_M - \hat{\alpha}_M < \frac{\alpha_M}{4Q}. \tag{4.29}$$

This last condition implies that based on the discretization Q the condition becomes more stringent and will not be met for some combinations of α_M, $\hat{\alpha}_M$, and Q. Figure 4.9 shows a graph that relates the discretization Q to the minimal radius of rotation of the linear fan-beam system which can be approximated by angular fan-beam using this method. Table 4.2 shows the corresponding angular fan-beam scheme for the data in Figure 4.9.

Table 4.2: *Linear and angular fan-beam schemes that are equivalent from a non-uniform sampling perspective: r is the radius of rotation of the angular fan-beam scheme, Q is the chosen discretization, h_α is the angular resolution, $\hat{r}$ is the radius of rotation of the linear fan-beam transform, and h_s is the virtual detector resolution. The angular fan-beam configurations correspond to those in Figure 4.9.*

Angular Fan-beam			Linear Fan-beam	
r	Q	Implied h_α	$\hat{r}$	Implied h_s
1.92	10	0.0548	1.96	0.1162
3.22	30	0.0105	3.24	0.0350
5.81	100	0.0017	5.82	0.0102
8.22	200	0.0006	8.23	0.0050
10.09	300	0.0003	10.10	0.0033
13.30	512	0.0001	13.30	0.0020

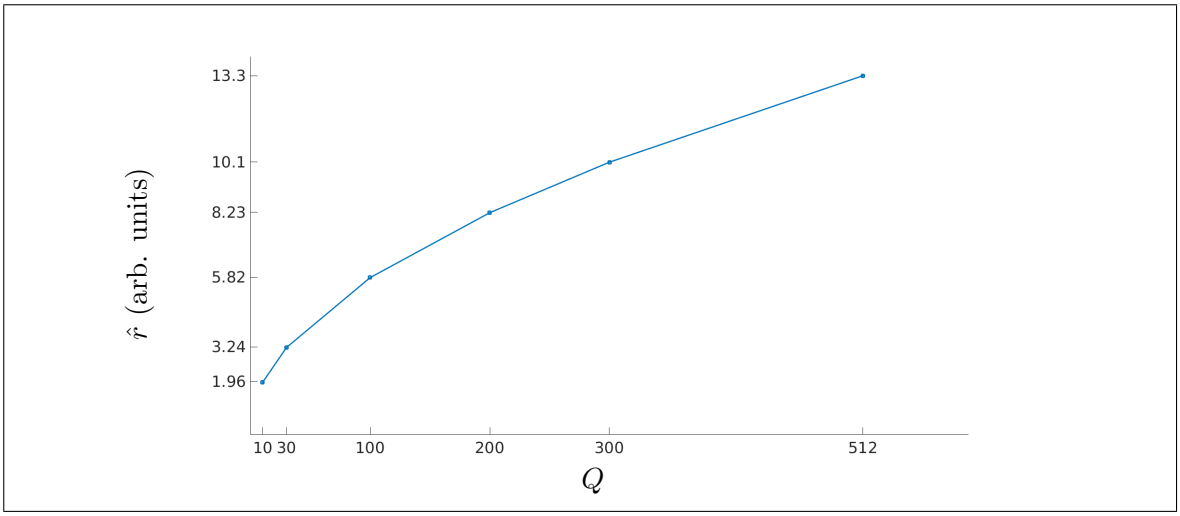

Figure 4.9: *The minimum radius of rotation of the linear fan-beam scheme as a function of the discretization Q for which the non-uniform approximation is applicable. If a linear fan-beam radius of rotation $\hat{r}$ falls below the line at the given discretization Q, then it cannot be approximated by an angular fan-beam transform using the proposed approximation.*

So far, the discussion regarding non-uniform sampling has revolved around the sampling of the detector space which is a one-dimensional problem, however, we would like to apply this perturbation theory to tomography. In tomography, we must ensure that the perturbation introduced in the detector space does not introduce aliasing in the angular sampling space β. In fact, if we choose an angular sampling of $\Delta\beta = \frac{\pi}{r\Omega}$ which corresponds to the efficient standard sampling scheme (see Figure 4.5c), then it is possible to alias the signal. To avoid aliasing from the angular direction, then we oversample the signal using $\beta \geq 2\pi/\Omega$ to obtain a sampling scheme like the one in Figure 4.7. We conjecture that in this configuration the perturbations associated to the detector sampling can be treated separately from the angular sampling scheme and therefore Theorem 4.2.2 is applicable.

4.3 Discussion, Next Steps and Future Work

4.3.1 A Discussion on the Proposed Approximation Approaches

It is apparent from Figure 4.10 that the coarse grid approach provides a stricter bound for the approximation of the two sampling schemes than non-uniform sampling. This is expected since the criterion in (4.24) measures the perturbation of the whole system, while the non-uniform approach measures only the largest perturbation in the detector space as dictated by (4.25). It follows that given a discretization $2Q+1$, the radius $\hat{r}$ obtained using the coarse grid approach will be larger than the one resulting from non-uniform sampling.

Figure 4.10 is indicative of the aforementioned. The radius of rotation of the linear fan-beam system for which said system can be treated as an angular fan-beam system is determined by the discretization $2Q + 1$. For example, in the case of the non-uniform approach a linear fan-beam sampling scheme with $Q = 100$, given object support radius $\rho = 1$, can only be treated by its equivalent angular fan-beam scheme if $\hat{r} > 5.82$. In other words, the radius of rotation needs to be about a factor of 6 larger than the radius of support

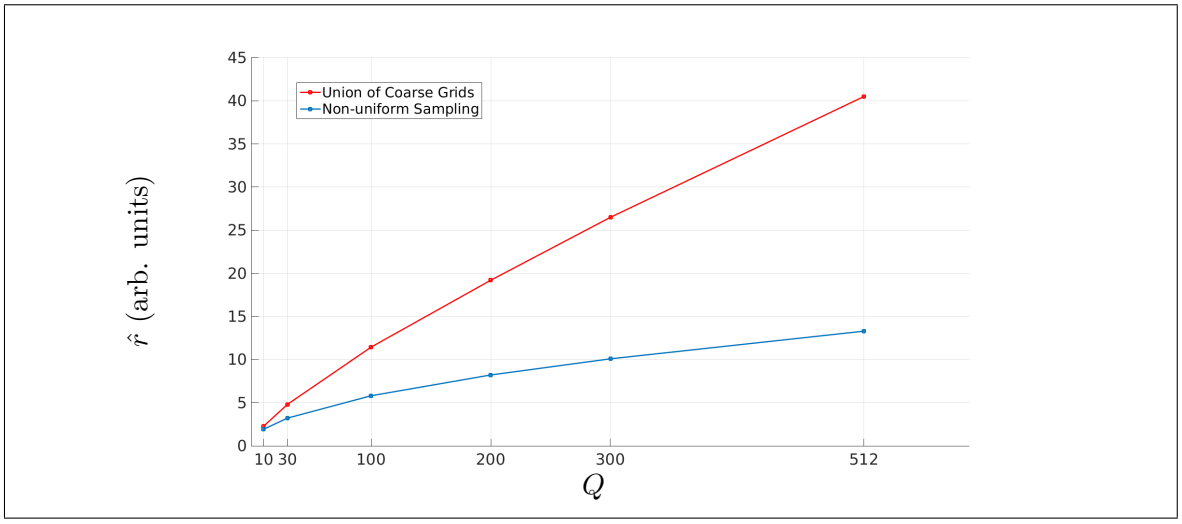

Figure 4.10: *A combined view of Figures 4.8 and 4.9 for comparison: the minimum radius of rotation of the linear fan-beam scheme using the proposed approximation methods*

of the object being imaged. In the same case, using the coarse grid approach we would need a radius of rotation that is 13 times the radial support of the object being imaged.

From our preliminary results, it seems the non-uniform approach provides a more feasible "valid approximation" set for $\hat{r}$ compared to the coarse-grid approach, albeit for large Q the factor $\hat{r}$ may prove infeasible.

4.3.2 Next steps

An important next step for the work presented in this chapter is to experimentally confirm our findings. That is, given the radius of rotation of the linear and angular fan-bean transforms for which the two are equivalent, we want to show that essentially bandlimited functions sampled using each scheme can be reconstructed exactly using either an angular or linear fan-beam reconstruction algorithm.

When using the "union of coarse sampling lattices" approach the images can be reconstructed using the known angular or linear fan-beam algorithms (cf. [55, Chapter 5]), however, in the case of the "non-uniform sampling" we predict that we will need to design a different reconstruction algorithm since this theory hinges on the interpolation scheme in Theorem 4.2.2.

4.3.3 Future Work

While the work presented here can be applied to fan-beam imaging systems under the assumption that there is no correlation of signal from different slices in the object space (i.e. signal emitted in one object slice is detected in one row of the fan-beam detector), our objective is to extend the theory to three dimensions so as to apply the same principles to single-pinhole collimators in SPECT (or equivalently cone-beam CT). This is not a straightforward task as the essential set K must be found for the angular cone-beam transform (in 3D) in order to check the perturbation conditions for the flat-detector cone-beam transform.

We recognize, however, that progress has been made in this respect as some results on the essential support for cone-beam CT have been published in [8].

Finally, while the immediate objective of our approach is to find sampling conditions for single-pinhole collimators with flat-detectors, we aim to develop the proposed approximation theory to a point where we can provide a theoretical framework for the approximation of transforms whose sampling conditions are not known by those whose sampling conditions are known.

Chapter 5

Concluding Remarks and Future Outlook

The presented research attempts to address the key steps in the SPECT medical imaging pipeline using pinhole collimators, namely, data acquisition, projector modelling, and image reconstruction.

The proposed distance-driven projector is geared toward SPECT imaging, where the object space discretization is typically coarser compared to other imaging modalities (such as CT), and therefore fewer approximations are made (compared to conventional distance-driven projection typically used for CT) with the intent of providing more accurate *overlap ratios*. The intent of proposed distance-driven approach is to improve the quality and accuracy of reconstructed SPECT images obtained from scanners such as the GE Discovery NM 530c.

The proposed projector is incorporated in image reconstruction methods that employ *kernel density estimators*, to regularize the variations of time-activity functions over proximal regions with similar temporal behaviour. Kernel density estimators and mean-shift filtering have been extensively studied and used in image processing as a method of image denoising. Here, we propose to apply the same concept in image reconstruction since KDE-based priors seem suited for reconstruction from noisy measurements due to the ability to "extract" signal embedded in the noise under the (general) assumption that the prior distribution can be described as a sum of kernel functions. That is, a KDE-like prior "lets the data decide" whether the signal is significant.

In the future, it would be beneficial to evaluate the proposed projection and reconstruction methods through *receiver operating characteristic* (ROC) studies, with the aim of evaluating whether the proposed approaches facilitate the detection and diagnosis of heart lesions such as ischemia or infarction in the context of dynamic emission tomography.

A completing step in the presented research is the study of sampling conditions in tomography, where we attempt to find conditions for which the properties of the flat-detector single-pinhole transform in 2D can be approximated using the (well-known and thoroughly studied) fan-beam transform. Sampling is of great importance to the medical imaging process since without an adequate acquisition it becomes difficult to assess whether reconstructed images provide reliable or meaningful information (in a clinical sense). That is, without adequate acquisition one cannot expect the image reconstruction algorithm to "insert" relevant information. In the future, we envision the application of the presented sampling theory to emission tomography scanners with varying shapes of the detector surface.

Bibliography

[1] H. O. Anger. Radioisotope Cameras. *Instrumentation in Nuclear Medicine*, 1:485–552, 1967.

[2] H. O. Anger and D. J. Rosenthal. Scintillation Camera and Positron Camera. *Medical Radioisotope Scanning*, pages 59–82, 1959.

[3] K. Assié, V. Breton, I. Buvat, C. Comtat, S. Jan, M. Krieguer, D. Lazaro, C. Morel, M. Rey, G. Santin, L. Simon, S. Staelens, D. Strul, J. M. Vieira, and R. Van de Walle. Monte Carlo Simulation in PET and SPECT Instrumentation Using GATE. *Nuclear Instrumentation and Methods in Physics Research*, A527:180–189, 2004.

[4] C. B. Barber, D. P. Dobkin, and H. Huhdanpaa. The Quickhull Algorithm for Convex Hulls. *ACM Transactions on Mathematical Software*, 22(4):469–483, 1996.

[5] J. Benedetto and A. Zayed, editors. *Sampling, Wavelets, and Tomography*, volume 21. Birkhäuser, 2004.

[6] Bleistein, N. and Handelsman, R. *Asymptotic Expansion of Integrals*. Holt, Rinehart, and Winston, 1975.

[7] M. Bocher, I. Blevis, L. Tsukerman, Y. Shrem, G. Kovalski, and L. Volokh. A Fast Cardiac Gamma Camera with Dynamic SPECT Capabilities: Design, System Validation and Future Potential. *European Journal of Nuclear Medicine and Molecular Imaging*, 37(10):1887–1902, 2010.

[8] J. Brokish and Y. Bresler. Sampling Requirements for Circular Cone Beam Tomography. In *Nuclear Science Symposium Conference Record, 2006. IEEE*, volume 5, pages 2882–2884, Oct 2006.

[9] J. Browne and A. R. De Pierro. A Row-Action Alternative to the EM Algorithm for Maximizing Likelihoods in Emission Tomography. *IEEE Transactions on Medical Imaging*, 15(5):687–699, 1996.

[10] P. L. Butzer, G. Schmeisser, and R. L. Stens. An Introduction to Sampling Analysis. In *Nonuniform Sampling*, pages 17–121. Kluwer Academic / Plenum Publishers, 2001.

[11] I. Buvat and D. Lazaro. Monte Carlo Simulations in Emission Tomography and GATE: an Overview. *Nuclear Instrumentation and Methods in Physics Research*, 569:323–329, 2006.

[12] T. Cacoullos. Estimation of a Multivariate Density. *Annals of the Institute of Statistical Mathematics*, 18:179–189, 1966.

[13] M. Carli. *Cardiac PET and PET/CT Imaging*. Springer Science & Business Media, LLC., 2007.

[14] T. M. Chan. Optimal Output-sensitive Convex Hull Algorithms in Two and Three Dimensions. *Discrete and Computational Geometry*, 16:361–368, 1996.

[15] D. Comaniciu and P. Meer. Mean shift analysis and applications. In *Computer Vision, 1999. The Proceedings of the Seventh IEEE International Conference on*, volume 2, pages 1197–1203, 1999.

[16] D. Comaniciu and P. Meer. Mean Shift: A Robust Approach Toward Feature Space Analysis. *IEEE Transactions on Pattern Analysis and Machine Intelligence*, 24(5):603–619, 2002.

[17] D. Comaniciu, V. Ramesh, and P. Meer. The Variable Bandwidth Mean Shift and Data-driven Scale Selection. In *Computer Vision, 2001. ICCV 2001. Proceedings. Eighth IEEE International Conference on*, volume 1, pages 438–445, 2001.

[18] B. De Man and S. Basu. Distance-driven Projection and Backprojection. In *IEEE Nuclear Science Symposium and Medical Imaging Conference*, 2002.

[19] B. De Man and S. Basu. Distance-driven projection and backprojection in three dimensions. *Physics in Medicine and Biology*, 49:2463–2475, 2004.

[20] A. R. De Pierro and M. E. B. Yamagishi. Fast EM-Like Methods for Maximum "A Posterior" Estimates in Emission Tomography. *IEEE Transactions on Medical Imaging*, 20(4):280–288, 2001.

[21] A. P. Dempster, N. M. Laird, and D. B. Rubin. Maximum Likelihood from Incomplete Data via the EM Algorithm. *Journal of the Royal Statistical Society: Series B*, 39(1):1–38, 1977.

[22] L. Desbat. Efficient Sampling on Coarse grids in Tomography. *Inverse Problems*, 9:152–269, 1993.

[23] E. Di Bella, H. Khare, D. Kadrmas, and G. Gullberg. SPECT Imaging of Teboroxime during Myocardial Blood Flow Changes. *IEEE Transactions on Nuclear Science*, 47(3):982–988, 2000.

[24] E. Di Bella, S. Ross, D. Kadrmas, H. Khare, P. Christian, S. McJames, and G. Gullberg. Compartmental Modeling of Technetium-99m-labeled Teboroxime with Dynamic Single-photon Emission Computed Tomography: Comparison with Static Thallium-201 in a Canine Model. *Investigative Radiology*, 36(3):178–185, 2001.

[25] A. Faridani. An Application of a Multidimensional Sampling Theorem to Computed Tomography. In *Integral Geometry and Tomography*, volume 113, pages 65–80. American Mathematical Society, 1990.

[26] A. Faridani. Fan-beam Tomography and Sampling Theory. In *Proceedings of Symposia in Applied Mathematics*, volume 63, 2006.

[27] T. H. Farncombe, S. Blinder, A. Celler, D. Noll, J. Maegt, and R. Harrop. A Dynamic Expectation Maximization Algorithm for Single Camera Rotation Dynamic SPECT (dSPECT). In *IEEE Nuclear Science and Medical Imaging Conference*, pages 15/31–15/25, 2000.

[28] T. H. Farncombe, A. Celler, C. Bever, D. Noll, J. Maegt, and R. Harrop. The Incorporation of Organ Uptake Into Dynamic SPECT (dSPECT) Image Reconstruction. *IEEE Transactions on Nuclear Science*, 48:3–9, 2001.

[29] L. Fu and J. Qi. Evaluation of 2D ROI Image Reconstruction Using ML-EM Method from Truncated Projections. In *IEEE Nuclear Science Symposium Conference Record*, pages 2236–2241, 2006.

[30] K. Fukunaga and L. D. Hostetler. The Estimation of the Gradient of a Density Function, with Applications in Pattern - Recognition. *IEEE Transactions on Information Theory*, IT-21(1):32–40, 1975.

[31] K. Fukushima, M. Mitsuru, K. Chisato, K. Kusakabe, and H. Kasanuki. Myocardial kinetics of ^{201}Thallium, ^{99m}Tc-tetrofosmin and ^{99m}Tc-sestamibi in an Acute Ischemia–Reperfusion Model Using Isolated Rat Heart. *Annals of Nuclear Medicine*, 21(5):267–273, 2007.

[32] A. G. García. The Paley-Wiener-Levinson Theorem Revisited. *International Journal of Mathematics and Mathematical Sciences*, 20(2):229–234, 1997.

[33] P. J. Green. Bayesian Reconstructions From Emmission Tomography Data Using a Modified EM Algorithm. *IEEE Transactions on Medical Imaging*, 9(1):84–93, 1990.

[34] P. J. Green. On Use of the EM Algorithm for Penalized Likelihood Estimation. *Journal of the Royal Statistical Society. Series B (Methodological)*, 52(3):443–452, 1990.

[35] G. Gullberg, B. Reutter, A. Sitek, J. Maltz, and T. Budinger. Dynamic single photon emission computed tomography, basic principles and cardiac applications. *Physics in Medicine and Biology*, 55(20):111–191, 2010.

[36] R. Gunn, S. Gunn, T. Turkheimer, J. Aston, and V. Cunningham. Positron Emission Tomography Compartmental Models: A Basis Pursuit Strategy for Kinetic Modeling. *Journal of Cerebral Blood Flow Metabolism*, 22(12):1425–1439, 2002.

[37] H. M. Hudson and R. S. Larkin. Accelerated Image Reconstruction Using Ordered Subsets of Projection Data. *IEEE Transactions on Medical Imaging*, 13:973–982, 1994.

[38] R. H. Huesman, B. W. Reutter, G. L. Zeng, and G. T. Gullberg. Kinetic Parameter Estimation from SPECT Cone-beam Projection Measurements. *Physics in Medicine and Biology*, 43:973–982, 1998.

[39] D. Hunter and K. Lange. A tutorial on MM algorithms. *The American Statistician*, 58(1):30–37, 2004.

[40] A. Ihsani and T. H. Farncombe. A Mathematical Formulation of the Single-Pinhole Transform and Asymptotic Properties in Fourier Space. In *IEEE Nuclear Science Symposium and Medical Imaging Conference*, pages 2493–2496, 2012.

[41] Howard Jacobowitz and Scott D. Metzler. Geometric Sensitivity of a Pinhole Collimator. *International Journal of Mathematics and Mathematical Sciences*, 2010(3), 2010.

[42] R. A. Jarvis. On the Identification of the Convex Hull of a Finite Set of Points in the Plane. *Information Processing Letters*, 2(1):18–21, 1973.

[43] E. L. Johnson, H. Wang, J. W. McCormick, K. L. Greer, R. E. Coleman, and Jaszczak. Pixel Driven Implementation and Filtered Backprojection for Reconstruction of a Fan Beam SPECT Data Using a Position Dependent Effective Projection Bin Length. *Physics in Medicine and Biology*, 41:1439–1452, 1996.

[44] Peter M. Joseph. An Improved Algorithm of Reprojecting Rays Through Pixel Images. *IEEE Transactions on Medical Imaging*, 1(3):192–196, 1982.

[45] D. Kadrmas and G. Gullberg. 4D Maximum a posteriori Reconstruction in Dynamic SPECT Using a Compartmental Model-based Prior. *Physics in Medicine and Biology*, 46:1553–1574, 2001.

[46] P. Krijnen, C. Nijmenijer, C. Visser, C. Hack, and H. Niessen. Apoptosis in Myocardial Ischaemia and Infarction. *Journal of Clinical Pathology*, 55(11):801–811, 2002.

[47] T. Le, T. Chartrand, and T. J. Asaki. A Variational Approach to Reconstructing Images Corrupted by Poisson Noise. *Journal of Mathematical Imaging and Vision*, 27(3):257–263, 2007.

[48] N. Levinson. *Gap and Density Theorems*. American Mathematical Society, 1940.

[49] E. Levitan and G. T. Herman. A Maximum A Posteriori Probability Expectation Maximization Algorithm for Image Reconstruction in Emission Tomography. *IEEE Transactions on Medical Imaging*, MI-6(3):185–192, 1987.

[50] Y. Mao and G. L. Zeng. A Tailored ML-EM Algorithm for Reconstruction of Truncated Projection Data Using Few View Angles. *Physics in Medicine and Biology*, 58(12), 2013.

[51] S. D. Metzler and R. Accorsi. Resolution- Versus Sensitivity-effective Diameter in Pinhole Collimation: Experimental Verification. *Physics in Medicine and Biology*, 50(21):5005–5017, 2005.

[52] S. D. Metzler, J. E. Bowsher, M. F. Smith, and R. J. Jaszczak. Analytic Determination of Pinhole Collimator Sensitivity with Penetration. *IEEE Transactions on Medical Imaging*, 20(8):730–741, 2001.

[53] F. Natterer. *The Mathematics of Computerized Tomography*. John Wiley & Sons, 1986.

[54] F. Natterer. Sampling in Fan Beam Tomography. *SIAM Journal on Applied Mathematics*, 53(2):358–380, 1993.

[55] F. Natterer and F. Wübbeling. *Mathematical Methods in Image Reconstruction*. SIAM, 2001.

[56] O. Pahlm and G. Wagner. *Multimodal Cardiovascular Imaging Principles and Clinical Applications*. McGraw-Hill Medical, 2011.

[57] D. Paix. Pinhole imaging of gamma rays. *Physics in Medicine and Biology*, 12:489–500, 1967.

[58] V. Palamodov. Localization of Harmonic Decomposition of the Radon Transform. *Inverse Problems*, 11:1025–1030, 1995.

[59] R. Paley and N. Wiener. Fourier Transform in the Complex Domain. *Amer. Math. Soc. Colloq. Publ.*, 19, 1934.

[60] N. Parikh and S. Boyd. Proximal Algorithms. *Foundations and Trends® in Optimization*, 1(3):123–231, 2013.

[61] Emmanuel Parzen. On Estimation of a Probability Density Function and Mode. *The Annals of Mathematical Statistics*, 33(3):1065–1076, 1962.

[62] T. Peters. Algorithms for Fast Back- and Re-projection in Computed Tomography. *IEEE Transactions on Nuclear Science*, 28:3641–3647, 1981.

[63] D. P. Petersen and D. Middleton. Sampling and Reconstruction of Wave-Number-Limited Functions in N-Dimensional Euclidean Spaces. *Information and Control*, 5(4):279–323, 1962.

[64] B Reutter, G. Gullberg, and R. Huesman. Direct Least-Squares Estimation of Spatiotemporal Distributions from Dynamic SPECT Projections Using a Spatial Segmentation and Temporal B-Splines. *IEEE Transactions of Medical Imaging*, 19(5), 2000.

[65] B. W. Reutter, G. T. Gullberg, and R. H. Huesman. Effects of Temporal Modelling on the Statistical Uncertainty of Spatiotemporal Distributions Estimated Directly from Dynamic SPECT Projections. *Physics in Medicine and Biology*, 47(15):2673, 2002.

[66] S. Rit, M. Vila Oliva, S. Brousmiche, R. Labarbe, D. Sarrut, and G. C. Sharp. The Reconstruction Toolkit (RTK), an Open-source Cone-beam CT Reconstruction Toolkit Based on the Insight Toolkit (ITK). *Journal of Physics: Conference Series*, 489, 2014.

[67] M. Rosenblatt. Remarks on Some Nonparametric Estimates of a Density Function. *The Annals of Mathematical Statistics*, 27(3):569–878, 1956.

[68] P. Shirley and K. Chiu. A Low Distortion Map Between Disk and Square. *Journal of Graphics Tools*, 2(3):45–52, 1997.

[69] A. Smith, T. Gullberg, and .P Christian. Experimental Verification of Technetium 99m-labelled Teboroxime Kinetic Parameters in the Myocardium with Dynamic Single-Photon Emission Computed Tomography: Reproducibility, Correlation to Flow, and Susceptibility to Extravascular Contamination. *Journal of Nuclear Medicine*, 3(2):130–142, 1996.

[70] I. Sutherland and G. W. Hodgman. Reentrant Polygon Clipping. *Communications of the ACM*, 17:3242, 1974.

[71] Ping Wang, Dongryeol Lee, Alexander G. Gray, and James M. Rehg. Fast mean shift with accurate and stable convergence. In Marina Meila and Xiaotong Shen, editors, *AISTATS*, volume 2 of *JMLR Proceedings*, pages 604–611, 2007.

[72] K. Weiler and P. Atherton. Hidden Surface Removal Using Polygon Area Sorting. *Computer Graphics*, 11(2):214–222, 1977.

[73] N. Weissman and G. Adelmann. *Cardiac Imaging Secrets*. Hanley & Belfus, 2004.

[74] M. Wernick and J. Aarsvold. *Emission Tomography: The Fundamentals of PET and SPECT*. Elsevier Academic Press, 2004.

[75] K. Wong, S. Meikle, D. Feng, and M. Fulham. Numerical Deconvolution by a Monte Carlo Approach with Application to Dynamic Cardiac Perfusion Tc-99m SPECT. In D Feng, J. Jin, P. Eades, and H. Yan, editors, *Visualisation 2001, Selected Papers from the Pan-Sydney Area Workshop on Visual Information Processing, VIP2001*, volume 11 of *CRPIT*, pages 123–127. Australian Computer Society, 2001.

[76] Chunxia Xiao and Meng Liu. Efficient mean-shift clustering using gaussian kd-tree. *Computer Graphics Forum*, 29(7):2065–2073, 2010.

[77] Fang Xu and Klaus Mueller. A Comparative Study of Popular Interpolation and Integration Methods for Use in Computed Tomography. In *Biomedical Imaging: Nano to Macro, 2006. 3rd IEEE International Symposium on*, pages 1252–1255, 2006.

[78] R. M. Young. *An Introduction to Nonharmonic Fourier Series*. Academic Press, 1980.

[79] G. Zeng and G. Gullberg. A Ray-Driven Backprojector for Backprojection Filtering and Filtered Backprojection Algorithms. In *IEEE Nuclear Science Symposium. Medical Imaging Conference. (San Francisco)*, pages 1199–1201, 1993.

[80] G. L. Zeng, G. T. Gullberg, and D. J. Kadrmas. Closed-Form Kinetic Parameter Estimation Solution to the Truncated Data Problem. *Physics in Medicine and Biology*, 55(24):7453–7468, 2010.

[81] B. Zhang and G. L. Zeng. Two-dimensional Iterative Region-of-interest (ROI) Reconstruction from Truncaed Projection Data. *Medical Physics*, 34(3):935–944, 2007.

[82] W. Zhuang, S. Gopal, and T. Herbert. Numerical Evaluation of Methods for Computing Tomographic Projections. *IEEE Transactions on Nuclear Science*, 41:1660–1665, 1994.